Astronomy Reports, Vol. 46, No. 9, 2002, pp. 697–703. Translated from Astronomicheskiĭ Zhurnal, Vol. 79, No. 9, 2002, pp. 771–777.

Classification of Optical Identifications of Radio Sources from Complete Samples

V. Chavushyan[1], R. Mujica[1], J. R. Valdes[1], A. G. Gorshkov[2], V. K. Konnikova[2], and M. G. Mingaliev[3]

[1]*Instituto Nacional de Astrofísica, Óptica y Electrónica, Luís Enrique Erro No. 1, Apdo Postal 51 y 216, Tonantzintla, Puebla, 72840 México*

[2]*Sternberg Astronomical Institute, Universitetskiĭ pr. 13, Moscow, 119899 Russia*

[3]*Special Astrophysical Observatory, Russian Academy of Sciences, Nizhniĭ Arkhyz, Karachaevo-Cherkesskaya Republic, 357169 Russia*

Received November 22, 2001; in final form, February 1, 2002

Abstract—Classifications of the optical counterparts and radio spectra of nine radio sources are presented. The observations were carried out using the 2.1-m optical telescope in Cananea (Mexico) at 4200–9000 Å and the RATAN-600 radio telescope at 0.97–21.7 GHz. Five objects have been classified as quasars (three have redshifts $z > 2$), two as BL Lac objects, one as an elliptical galaxy, and one as an absorption-line galaxy. © *2002 MAIK "Nauka/Interperiodica".*

1. INTRODUCTION

This paper continues our work on classifying optical objects identified with radio sources from complete samples corresponding to a specified flux density. We have obtained spectra for eight objects representing optical counterparts of radio sources from a complete sample derived from the MGB survey at 4.85 GHz. The sample contains all sources with flux densities $S_{4.85} > 200$ mJy with declinations $10°–12°30'$ (J2000), right ascensions $0–24^h$, and $|b| > 10°$. One distinctive feature of the sample is the large fraction of optical identifications obtained for the radio sources (88% of the flat-spectrum objects have identifications down to 21^m). This makes the sample promising for cosmological studies. One object is the optical counterpart of a radio source from the Zelenchuk survey ($S_{3.9} > 200$ mJy, declinations $4°–6°$ (B1950)), which has been studied by us since 1984 [1–3]. The results of previous work on classifications of optical objects identified with sources in this sample have been published in [4, 5].

2. RADIO AND OPTICAL OBSERVATIONS

Radio observations of the sources were carried out on the Northern quadrant of the RATAN-600 telescope at 0.97, 2.3, 3.9, 7.7, 11.1, and 21.7 GHz. The parameters of the receivers and telescope beams are given in [2, 6]. The error in the flux-density measurements dS was determined in the standard way from the scatter of the fluxes recorded every day in a given observing session. This estimate includes all types of errors: noise, calibration errors, errors in linking to the calibration signal, antenna pointing errors, etc. For long series of observations of variable sources, the rms flux error during a session is also included in the error in the average flux density. The data processing technique is described in [7].

Optical spectra of the objects were obtained in June–October, 1999 using the 2.1-meter telescope of the Guillermo Haro Observatory (Cananea, Mexico), Instituto Nacional de Astrofísica, Óptica y Electrónica (INAOE). We used the LFOSC spectrophotometer equipped with a 600×400 CCD matrix [8]. The detector read-out noise was 8 electrons. The spectrophotometer wavelength range was 4200–9000 Å with a dispersion of 8.2 Å/mm. The effective instrumental spectral resolution was about 16 Å.

The optical data were processed with the IRAF package, including removal of cosmic rays, flat-fielding, wavelength linearization, and flux calibration.

3. RADIO AND OPTICAL COORDINATES

Table 1 lists the positions of the objects from the catalogs of the JVAS2[1] and CLASS[2] surveys at 8.4 GHz [9, 10] and the NVSS survey at 1.4 GHz [11], differences between the radio and

[1]JVAS, Jodrell Bank–VLA Astrometric Survey.

[2]CLASS, Cosmic Lens All-Sky Survey.

1063-7729/02/4609-0697$22.00

Table 1. Positions and magnitudes of the objects

Object name	Radio position J2000.0		Radio−optical		R	B	Survey
	RA	DEC	ΔRA	ΔDEC			
0121+1127	$01^h21^m29^s.00$	$+11°27'00''.53$	0.02^s	$0.73''$	17.1	17.4	JVAS
0211+1051	02 11 13.18	+10 51 34.79	−0.01	−0.01	14.8	15.1	JVAS
0323+0446	03 23 14.72	+04 46 12.59	−0.02	−0.01	18.9	19.1	JVAS
0345+1218	03 45 01.32	+12 18 48.77	−0.01	−0.13	18.5	19.5	CLASS
2203+1217	22 03 45.54	+12 17 15.63	−0.10	−2.07	17.5	18.5	NVSS
2229+1127	22 29 57.45	+11 27 37.73	0.09	−0.57	18.5	21.2	NVSS
2233+1008	22 33 58.45	+10 08 52.10	0.04	0	18.0	17.6	JVAS
2300+1037	23 00 18.32	+10 37 54.08	0	0.08	18.4	18.6	CLASS
2330+1228	23 30 09.95	+12 28 28.60	0.02	−0.40	14.5	17.5	JVAS

optical positions in right ascension and declination, and the R and B magnitudes of the objects. The optical coordinates and magnitudes were taken from the USNO catalog of astrometric standards [12] and the APM database of the Palomar Sky Survey [13]. The source names are composed from the hours and minutes of the object's right ascension and the degrees and minutes of its declination for epoch 2000.0. The rms error of the positions in the JVAS and CLASS catalogs is $0.012''$ and in the NVSS survey catalog is, on average, about $0.035''$ and $0.56''$ for right ascension and declination, respectively.

4. RESULTS

The optical and radio spectra of all the sources are presented in Figs. 1 and 2.

4.1. 0121+1121

The May 2001 spectrum at 0.97–21.7 GHz peaks at 6.5 GHz and can be approximated by the logarithmic parabola $\log S = 1.717 + 1.208\log\nu - 0.741\log^2\nu$. (Frequencies here and below are given in Gigahertz and flux densities in milliJanskys.) Most of the flux density comes from a compact component, and the extended emission is weak. The source is absent from low-frequency surveys.

This source is identified with a blue starlike object. The optical spectrum of the object was obtained on September 13, 1999 with a 40-min exposure. We have identified the Lyα 1216 Å emission line of hydrogen, the nearby lines SiIV/OIV] 1400 Å, CIV 1549 Å and the semiforbidden line CIII] 1909 Å in the spectrum. The redshift determined from all the lines is $z = 2.485$, and the object is classified as a quasar.

4.2. 0211+1051

The radio spectrum for October 2000 has a maximum at 12 GHz. At 0.97–21.7 GHz, the spectrum can be approximated by the logarithmic parabola $\log S = 2.324 + 0.385\log\nu - 0.181\log^2\nu$. Using the 611-MHz data, we can extract a power-law component with spectral index $\alpha = -0.8 \pm 0.1$ from the spectrum. The technique used to distinguish components in complex spectra is described in [3]. After subtracting the power-law component, the resulting spectrum of the compact component can be approximated by a logarithmic parabola with its maximum at 18 GHz. The radio source was observed in 2000 and 2001; its mean flux density remained unchanged at all frequencies over the year between these observations.

We have identified the radio source with a bright, blue object ($m(B) = 15.1$). The optical spectrum was obtained on September 13, 1999 with a 45-min exposure. The spectrum shows a featureless continuum, so that the object can be classified as a BL Lac object.

4.3. 0323+0446

At 0.97–21.7-GHz, the flux density decreases toward higher frequencies, and the spectrum for December 1998 can be approximated by the logarithmic parabola $\log S = 2.377 - 0.565\log\nu + 0.199\log^2\nu$. The observations at 3.9 and 7.7 GHz show that its flux density is slowly decreasing at these frequencies: at 3.9 GHz, from 200 mJy in the Zelenchuk survey of 1980 to 130 mJy in 1998. The 1990 spectrum at 3.9–11.1-GHz was also falling toward higher frequencies, with a mean spectral index of $\alpha = -0.23$ ($S \propto \nu^\alpha$). Apparently, most of the emission at these frequencies comes from an extended component, and

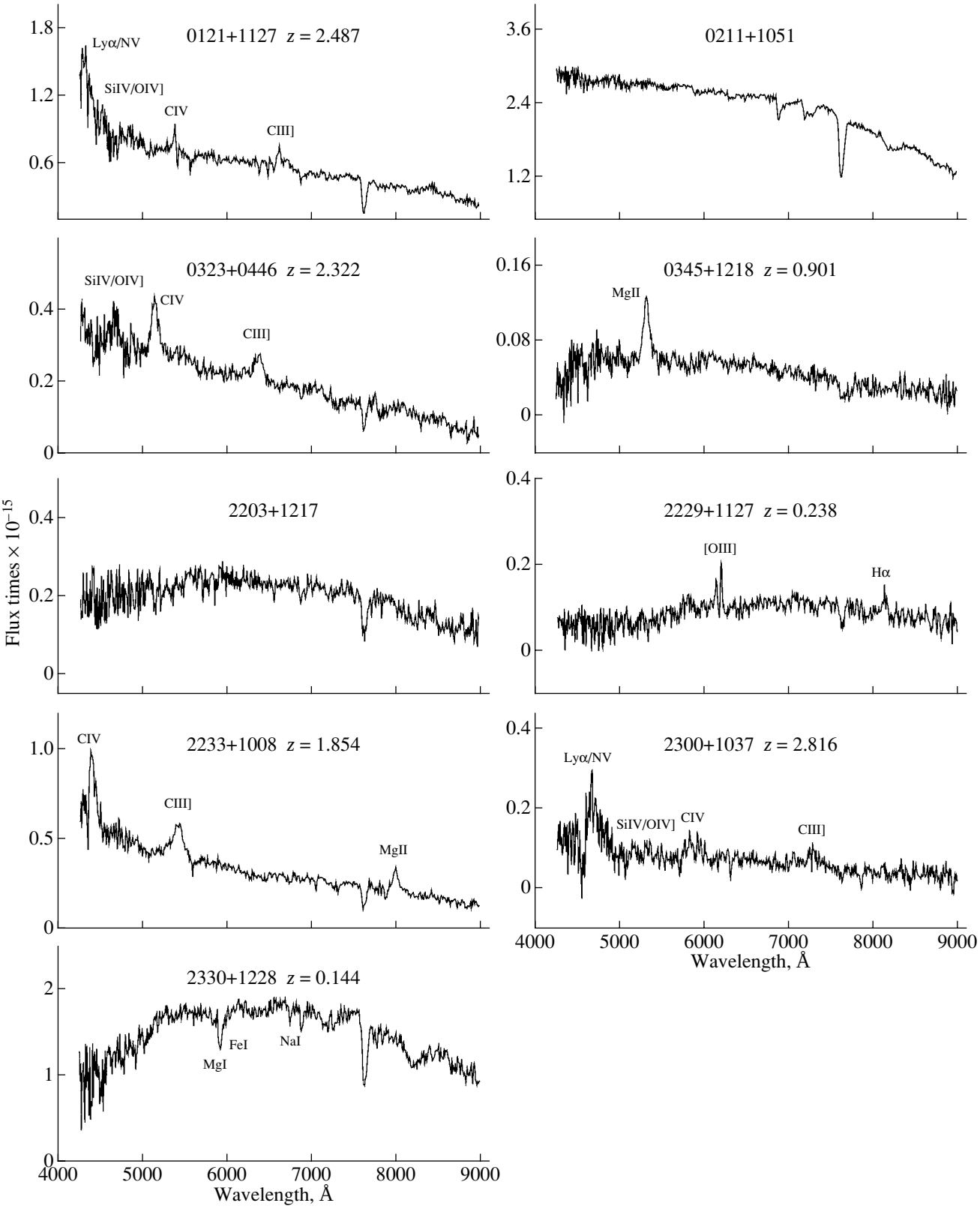

Fig. 1. Optical spectra of the objects.

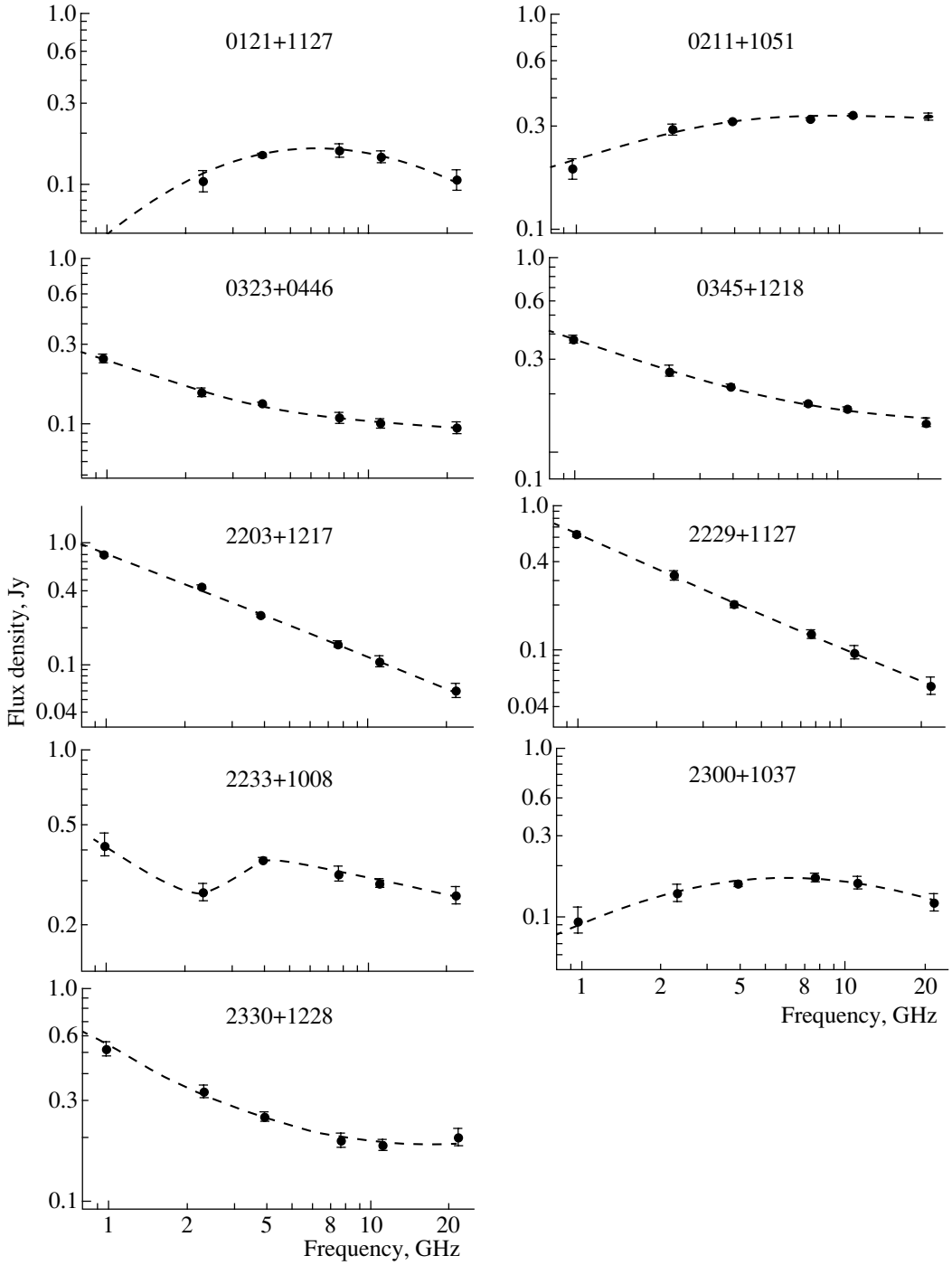

Fig. 2. Radio spectra of the objects.

the flattening of the spectrum is due to a compact component whose emission is concentrated at higher frequencies. In this case, the source spectrum can be divided into two components: a power law with spectral index $\alpha = -0.8 \pm 0.2$, whose emission dominates in the frequency range considered, and a compact component whose spectrum peaks at $\nu > 30$ GHz.

The optical spectrum was obtained on October 9, 1999 with a 60-min exposure. The strongest feature in the spectrum, which is more than 60 Å wide, has been identified with the CIV 1549 Å line of carbon. The 1394–1403 Å SiIV doublet and the OIV] 1406 Å and CIII] 1909 Å lines are also present. The redshift derived from all the lines is $z = 2.322$, and we classified the object as a quasar.

Table 2. Data concerning the optical and radio observations

Object name	Lines in the spectrum	Wavelength, lab./obs., Å	z	Object type	B	$S_{3.9\,\mathrm{GHz}}$, mJy $S_{7.7\,\mathrm{GHz}}$, mJy	α
0121+1127	Lyα	1216/4238	2.487	QSO	17.3	150 ± 5	0.08
	SiIV/OIV]	1400/4879				158 ± 15	
	CIV	1549/5398					
	CIII	1909/6653					
0211+1051	None			Lac	15.1	310 ± 5	0.08
						327 ± 7	
0323+0446	SiIV/OIV]	1400/5651	2.322	QSO	19.3	132 ± 4	−0.29
	CIV	1549/4650				108 ± 6	
	CIII	1909/6342					
0345+1218	MgII	2798/5319	0.901	QSO	19.5	215 ± 3	−0.28
						178 ± 3	
2203+1217	None			Lac	18.5	249 ± 9	−0.85
						102 ± 10	
2229+1127	[OIII]	4959/6139	0.238	ELG	19.1	208 ± 9	−0.74
	[OIII]	5007/6198				196 ± 8	
	H α	6563/8125					
2233+1008	CIV	1549/4421	1.854	QSO	17.6	360 ± 6	−0.17
	CIII	1909/5448				320 ± 20	
	MgII	2798/7985					
2300+1037	Lyα/NV	1216/4640	2.816	QSO	19.3	160 ± 5	0.12
	SiIV/OIV]	1400/5342				173 ± 10	
	CIV	1549/5911					
	CII	1909/7285					
2330+1228	MgI	5175/5920	0.144	AbsG	17.5	250 ± 10	−0.36
	FeI	5270/6029				195 ± 15	
	NaI	5896/6745					

4.4. 0345+1218

At 0.97–21.7 GHz, the source has a decreasing spectrum that flattens at high frequencies. The spectrum can be divided into a strong power-law component (comprising almost 100% of the flux density at 0.97 GHz) with spectral index $\alpha = -0.6 \pm 0.1$ and a compact component that is well approximated by a logarithmic parabola with its maximum at about 20 GHz. The total spectrum for October 2000 can be approximated by the parabola $\log S = 2.575 - 0.494 \log \nu + 0.144 \log^2 \nu$. The mean flux of the source did not change during the year between the observations in 2000 and 2001.

The optical spectrum was obtained on October 7, 1999 with a 60-min exposure. We have interpreted a strong emission feature with a width of about 80 Å as the MgII 2798 Å line at a redshift of $z = 0.901$. The object is classified as a quasar.

4.5. 2203+1218

The radio spectrum is a power-law at 0.365–21.7 GHz: $S = 779\nu^{-0.843}$.

The optical spectrum was obtained on October 9, 1999 with a 40-min exposure. There are no lines in the spectrum, and we have accordingly classified the source as a BL Lac object.

4.6. 2229+1127

The radio spectrum is a power-law at 0.408–21.7 GHz: $S = 622\nu^{-0.783}$.

The optical spectrum was obtained on October 10, 1999 with a 60-min exposure. We have identified two nearby lines separated by approximately 50 Å with the forbidden [OIII] 4959 Å and 5007 Å lines of oxygen. A weak line identified with the Hα 6563 Å line was also detected at the long-wavelength end of the spectrum. All the lines are in emission, and we have classified the object as an emission-line radio galaxy at a redshift of $z = 0.238$.

4.7. 2233+1008

The radio spectrum is complex, and the spectral index between 0.365 GHz (the Texas survey) and 0.97 GHz is $\alpha = -0.5$. If we assume that the source contains an extended component with this spectral index and subtract its contribution from the total spectrum, we obtain a spectrum that rises to 2.3 GHz and then reaches a plateau. This shape is close to the spectrum of a homogeneous, spherically symmetric source of synchrotron radio emission.

The optical spectrum, which was obtained on October 10, 1999 with a 60-min exposure, contains strong lines of carbon CIV 1549 Å and CIII] 1909 Å and a weaker magnesium MgII 2798 Å line at a redshift of $z = 1.854$. The object is a quasar.

4.8. 2300+1031

The spectrum at 0.97–21.7 GHz is well approximated by the logarithmic parabola $\log S = 0.082 + 0.868\log\nu - 0.582\log^2\nu$, which has its maximum at 7 GHz. The source is absent from low-frequency surveys. The extended component in the source is weak, and the bulk of the emission comes from a compact component.

The optical spectrum was obtained on October 10, 1999 with a 60-min exposure. We identified the Lyα/NV 1216 Å 1240 Å SiIV/OIV] 1400 Å CIV 1549 Å and CIII] 1909 Å lines at a redshift of $z = 2.816$. The object is a quasar.

4.9. 2330+1218

The radio spectrum flattens toward higher frequencies. The July 2001 spectrum can be approximated by the parabola $\log S = 2.911 - 1.255\log\nu + 0.614\log^2\nu$. At low frequencies, the spectrum can be divided into an extended component with a power-law spectrum with spectral index $\alpha = -0.54 \pm 0.1$ and a compact component with a rising spectrum in the range considered. The spectral index of the compact component in the initial segment is $\alpha \approx 1.8$, and the maximum occurs at 25–30 GHz.

The optical spectrum was obtained on October 6, 1999 with a 30-min exposure. We have identified three absorption lines MgI 5175 Å FeI 5270 Å and NaI 5896 Å at a redshift of $z = 0.144$. The object is an absorption-line elliptical galaxy.

5. CONCLUSION

Of the nine objects studied, five have been classified as quasars, three have redshifts $z > 2$, two are BL Lac objects, one is an absorption-line galaxy, and one is an emission-line galaxy. Table 2 summarizes some data concerning the optical and radio observations. The flux densities S at 3.9 and 7.7 GHz are given in mJy.

The columns of Table 2 present the (1) name of the object, (2) lines present in the spectrum, (3) line wavelengths in the laboratory system and as observed, (4) redshift of the object, (5) object type, (6) B magnitude of the object, (7) its flux densities at 3.9 and 7.7 GHz, and (8) the spectral index α between these frequencies.

ACKNOWLEDGMENTS

The authors thank the administration of the Guillermo Haro Observatory for support and attention to this work. This work was supported by the Russian Foundation for Basic Research (project no. 01-02-16331), the Universities of Russia Program (grant 015.02.02.19), and in part by two CONACYT grants (28499-E and J32178-E).

REFERENCES

1. A. G. Gorshkov and V. K. Konnikova, Astron. Zh. **72**, 291 (1995) [Astron. Rep. **39**, 257 (1995)].
2. A. M. Botashev, A. G. Gorshkov, V. K. Konnikova, and M. G. Mingaliev, Astron. Zh. **76**, 723 (1999) [Astron. Rep. **43**, 631 (1999)].
3. A. G. Gorshkov, V. K. Konnikova, and M. G. Mingaliev, Astron. Zh. **77**, 407 (2000) [Astron. Rep. **44**, 353 (2000)].
4. V. Chavushyan, R. Mujica, A. G. Gorshkov, *et al.*, Pis'ma Astron. Zh. **26**, 403 (2000) [Astron. Lett. **26**, 339 (2000)].

5. V. Chavushyan, R. Mujica, A. G. Gorshkov, *et al.*, Astron. Zh. **78**, 99 (2001) [Astron. Rep. **45**, 79 (2001)].
6. A. B. Berlin, A. A. Maksyasheva, N. A. Nizhel'skiĭ, *et al.*, in *Proceedings of the XXVII Radio-astronomy Conference, St. Petersburg, 1997,* Vol. 3, p. 115.
7. A. G. Gorshkov and O. I. Khromov, Astrofiz. Issled. (Izv. SAO) **14**, 15 (1981).
8. F. J. Zickgraf, I. Thiering, J. Krautter *et al.*, Astron. Astrophys., Suppl. Ser. **123**, 103 (1997).
9. I. W. A. Browne, P. N. Wilkinson, A. R. Patnaik, and J. M. Wrobel, Mon. Not. R. Astron. Soc. **293**, 257 (1998).
10. C. D. Fassnacht, S. T. Myers, T. J. Pearson, *et al.*, Astrophys. J., Suppl. Ser. **185**, 2301 (1994).
11. J. J. Condon, W. D. Cotton, E. W. Greisen, *et al.*, Astron. J. **115**, 1693 (1998).
12. D. Monet, A. Bird, B. Canzian, *et al.*, USNO-SA1.0 (Naval Observatory, Washington, DC, 1996).
13. R. L. Pennington, R. M. Humphreys, S. C. Odewahn, *et al.*, Publ. Astron. Soc. Pac. **105**, 103 (1993).

Translated by G. Rudnitskiĭ

Astronomy Reports, Vol. 46, No. 9, 2002, pp. 704–711. Translated from Astronomicheskiĭ Zhurnal, Vol. 79, No. 9, 2002, pp. 778–786.

BVRI Surface Photometry of the Galaxy NGC 3726

A. S. Gusev[1,2], A. V. Zasov[1], S. S. Kaĭsin[3], and D. V. Bizyaev[1]

[1]*Sternberg Astronomical Institute, Universitetskiĭ pr. 13, Moscow, 119899, Russia*

[2]*Institute of Solid State Physics, P.O. Chernogolovka, Moscow region, 142432, Russia*

[3]*Special Astrophysical Observatory, Russian Academy of Sciences, Nizhniĭ Arkhyz, Karachaevo-Cherkesskaya Republic, 357147 Russia*

Received November 19, 2001; in final form, February 1, 2002

Abstract—We present $BVRI$ surface photometry of the late-type spiral galaxy NGC 3627. The distributions of the color indices and extinction-independent Q indices show that the observed photometric asymmetry in the inner part of the galaxy, including the bar, is due to an asymmetric distribution of absorbing material. The bluest regions of star formation are located in a ring surrounding the bar. The background-subtracted color indices of individual blue knots are used to estimate the ages of young stellar aggregates. In combination with previously published photometric data, our measurements indicate that the R-band profile of the disk is rather flat in its inner part ($r < 50''$) and becomes steeper further from its center. We estimate the mass of the disk and dark halo by decomposing the rotation curve. The mass-to-light ratio M/L_B for the stellar disk is ≈ 1.4. The galaxy possesses a massive dark halo; however, the mass of the disk exceeds that of the halo in the inner part of the galaxy, which displays a regular spiral structure.

1. INTRODUCTION

Here, we will analyze detailed $BVRI$ photometry and the mass distribution of the fairly close spiral galaxy NGC 3726.

The SABc galaxy NGC 3726 is located at a distance of about 12 Mpc ($H_0 = 75$ km s^{-1} Mpc^{-1});[1)], and its luminosity is comparable to that of M31. A short bar is visible in the central region of the galaxy (Fig. 1). The two inner spiral arms of the galaxy form a ring around the bar, with several branching spirals beyond it. Table 1 presents the basic parameters of NGC 3726 adopted in our study (according to the RC3 [2] and LEDA catalogs).

The galaxy has been studied over a broad range of wavelengths by numerous observers. $U'JF$ [3], RJ [4], and JHK aperture photometry [5] are available. Parameters describing the brightness distribution over the disk (assuming an exponential brightness decrease with the radius r) and bulge of the galaxy in the J and TO bands are presented in [6]. An infrared image of the central region (from the 2MASS survey) can be found in the NASA Extragalactic Database (NED), available via the internet.

A diffuse core with an emission spectrum is seen at the galactic center, and is classified as a LINER (low-ionization emission region) [7]. According to Grosbol [8], the luminosity of the bulge in the red does not exceed 1% of the integrated luminosity of NGC 3716, and the brightness of the disk from 8″ to 164″ from the center falls of exponentially with a radial scale of 63″. However, in fact, the photometric profile is not well described by this exponential relation (see below). The azimuthal brightness distribution in NGC 3726 is fairly asymmetric at both optical wavelengths [4] and in the 21 cm line [3]. The morphology of the bar was studied in [9, 10], with very different bar parameters being obtained (for example, the derived axial ratio was $b/a = 0.5$ in [9] and $b/a = 0.22$ in [10]). The

Table 1. Basic parameters of NGC 3726

Type	SABc
B_T, mag	10.90
$M_B^{0,i}$, mag	−20.37
V_{LG}, km/s	908
D, Mpc	12.1
($H_0 = 75$ km s^{-1}Mpc^{-1})	
D_{25}, arcmin	6.05
i, deg	49.2
(PA), deg	10

[1)]In [1], the distance to the UMa cluster, to which the galaxy apparently belongs, is taken to be 15.5 Mpc.

1063-7729/02/4609-0704$22.00 © 2002 MAIK "Nauka/Interperiodica"

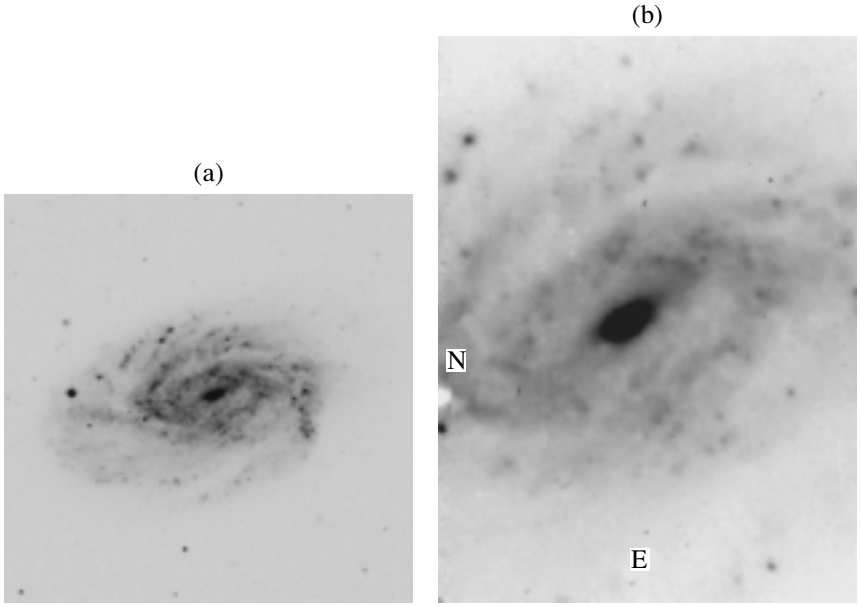

Fig. 1. (a) Digital Sky Survey image of NGC 3726 and (b) a CCD image of NGC 3226 in the V filter. The size of the region shown is (a) $6.8' \times 7.4'$ and (b) $2.4' \times 3.5'$ respectively. North is on the left and east is at the bottom.

age of the bar's population was estimated by Martinet and Friedli [11] to be 3×10^8 years (suggesting the bar is young).

The HI observations yield a mass of neutral hydrogen within a radius of $7.3'$ $M(\mathrm{HI}) = 3.8 \times 10^9 M_\odot$, which makes up several percent of the total mass of the galaxy within the same radius [3]. The maximum surface density of HI is $8.5 M_\odot/\mathrm{pc}^2$ and is observed $120''$ from the center of NGC 3726. Further from the center, the density of HI decreases dramatically: at a distance of $240''$, it is lower than $2.0 M_\odot/\mathrm{pc}^2$.

The galaxy also displays several fairly small HII condensations, related to regions of active star formation [13]. However, the luminosity of NGC 3726 in the far infrared is low compared to that in the blue: $L_{FIR}/L_B = 0.06$ [9], indicating a moderate star-formation rate in the galaxy overall.

Here, we analyze the brightness and color-index distributions in various regions of the galaxy and model its mass distribution using the rotation curve of [1].

2. OBSERVATIONS AND REDUCTION

NGC 3726 was observed on January 22–23, 1998 with the 1-m Zeiss-1000 telescope of the Special Astrophysical Observatory in the Johnson–Cousins B, V, R, and I bands. The image size was $2.4' \times 3.5'$, with $0.28'' \times 0.37''$ per pixel. Four 600-s exposures were made in each filter, with a small shift of the frame center to decrease the effect of inhomogeneous field sensitivity of the CCD matrix. The average seeing during the night was $3.0''$. Four standard stars from the list of Landolt [13] were observed on the same night as calibrators. The preliminary calibration was done using the ESO MIDAS package.

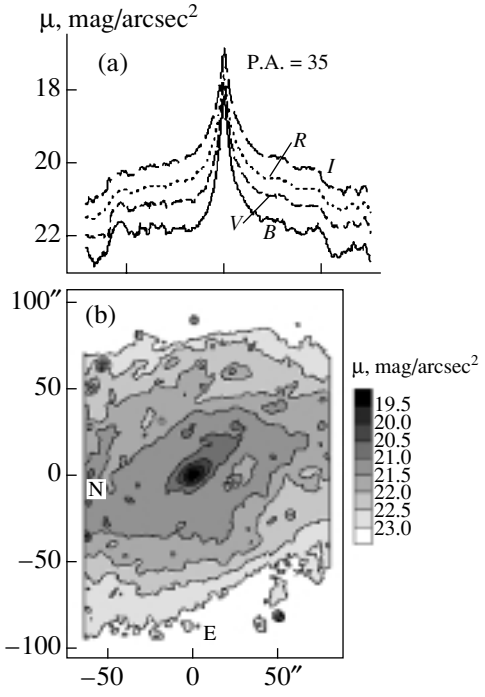

Fig. 2. (a) Photometric profiles along the major axis of NGC 3726 in B, V, R, and I along the position angle of the major axis 35°, and (b) the V isophotes of the galaxy.

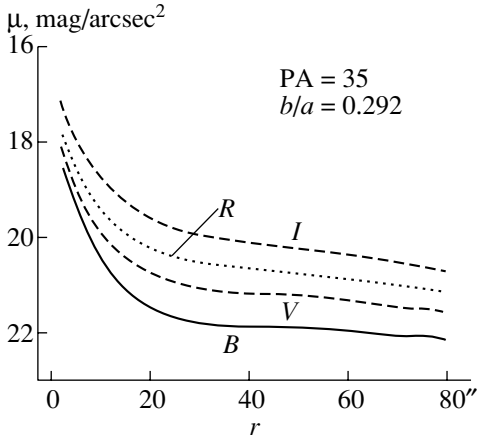

Fig. 3. Mean photometric profiles of NGC 3726 in B, V, R, and I.

The accuracy of the photometric calibration was 0.06^m in V and R, 0.12^m in B, and 0.04^m in I. We corrected both the brightness and color indices for Galactic extinction. We also introduced average corrections for the color excesses due to the inclination of the galactic disk to the line of sight (taken from the RC3 catalog [2]) for two-color diagrams and the colors of star-formation sites.

3. RESULTS

Due to the limited size of the field, we were able to study in detail only the inner region of the galaxy (Fig. 1b)—approximately $0.4D_{25}$, where D_{25} is the optical diameter. The outer regions of the disk to the north and south of the center of NGC 3726 remained beyond our field of view. Therefore, the results presented here correspond to a region with a radius of about 80″ (≈5 kpc). Apart from the disk, this region also contains the bright compact bulge (with a maximum V brightness of 17.8 mag/arcsec^2), which dominates within the central 20″ (about 1 kpc).

The brightness decrease in the core region along the major axis is asymmetric: it falls off very steeply toward the northeast, while the gradient toward the southwest is substantially smaller, especially in B (Fig. 2a). This was probably why van den Bergh [14] classified the core of NGC 3726 as a diffuse (non-star-like) object. The asymmetry is most pronounced in B and appreciably smaller in red filters, suggesting that it is related to some asymmetry in the distribution of either an absorbing medium or blue stars. We will show below that the first possibility is more likely.

The brightness of the bar of the galaxy, with a radius of about 3 kpc (50″), is also asymmetric. The surface brightness of the southwestern part of the bar falls off with distance exponentiallly, from $\mu_V = 20.8 \pm 0.03$ mag/arcsec^2 in the central region to $\mu_V = 21.3 \pm 0.05$ mag/arcsec^2 at the periphery. The V brightness of the northeastern part of the bar is 0.3 mag/arcsec^2 lower (Figs. 2a, 2b). At the edges of the bar ($r = 50''$), the local brightness increases in the blue by 0.3–0.4 mag/arcsec^2 in B. The ellipticity of the bar isophotes is 0.31 ± 0.01 in B, V, and R. The position angle of the bar ($PA = 25° \pm 3°$) is close to that of the major axis of the disk of the galaxy as a whole.

The spiral arms emerging from the ends of the bar form a ring with inner radius 2.9 kpc (50″). Its azimuth-averaged surface brightness is $\mu_V = 21.2 \pm 0.2$ mag/arcsec^2.

Figure 3 presents mean photometric profiles for the adopted disk position angle and axial ratio (the brightness is not corrected for the disk inclination). Decomposition of the profiles into the disk and bulge with its exponential profile (Table 2) indicates that, at distances $r = 26''-50''$ from the center, the main contribution to R is made by the disk, with a very slow exponential decrease of the brightness (with scale $r_{\rm disk} = 5.4 \pm 0.1$ kpc ($92'' \pm 2''$)) and a central surface brightness of $\mu_R(0) = 20.18 \pm 0.02$ mag/arcsec^2.

The disk brightness falls off more slowly at shorter wavelengths (see Table 2). The disk of NGC 3726 extends appreciably beyond our images. We used the FITS archive of Frei *et al.* [15], which contains R photometric data obtained with the 1.1-m telescope of the Lowell Observatory, to study the R photometric profile at large r. These data are in good agreement with our within 80″ of the center (with an accuracy of 0.06 mag/arcsec^2). The azimuthal profiles at distances from 50″ to 150″ of the galactic center indicate that, at large r, the disk of NGC 3726 displays an radial scale of $r_{\rm disk} = 3.26 \pm 0.05$ kpc ($55.6'' \pm 0.9''$) and $\mu_R(0) = 20.74 \pm 0.04$ mag/arcsec^2; the outer region of the disk makes a transition to the inner region 40″–50″ from the center. The obtained estimate for $r_{\rm disk}$ is consistent with the value 58″ found for the K band in [6].

Thus, NGC 3726 displays a brightness (density) "deficiency" in the inner part of its disk (a type II photometric profile according to Freeman [16]). In the region $r = 4''-18''$ from the center occupied by the bulge, an exponential brightness decrease with the scale $r_{\rm bulge} = 300 \pm 5$ pc ($5.11'' \pm 0.09''$) is observed; the surface brightness extrapolated to the center is $\mu_R(0) = 17.95 \pm 0.04$ mag/arcsec^2.

NGC 3726 is rather blue. Its integrated color index corrected for the Galactic extinction is $(B-V)_0 = 0.52^m$ [17]. According to our data, the color remains blue even in the bulge region. The color indices of the bulge ($B - V = 0.5^m \pm 0.1^m$, $V - R = 0.33^m \pm$

Table 2. Photometric parameters of the components of NGC 3726

Components	Filters	Distance interval, arcsec	Characteristic scale		Central surface brightness, mag/arcsec^2
			arcsec	kpc	
Bulge	B	4–18	4.5 ± 0.1	0.26 ± 0.01	18.57 ± 0.06
	V		4.8 ± 0.1	0.28 ± 0.01	18.25 ± 0.05
	R		5.1 ± 0.1	0.30 ± 0.005	17.95 ± 0.04
	I		5.0 ± 0.1	0.30 ± 0.004	17.24 ± 0.03
Inner disk	B	26–50	151.0 ± 7.2	8.86 ± 0.42	21.54 ± 0.03
	V		111.1 ± 2.7	6.51 ± 0.16	20.76 ± 0.02
	R		91.9 ± 1.7	5.39 ± 0.10	20.18 ± 0.02
	I		72.1 ± 1.3	4.23 ± 0.08	19.50 ± 0.02
Outer disk	R	50–150	55.6 ± 0.9	3.26 ± 0.05	20.74 ± 0.04

Table 3. Parameters of sites of star formation

No.	Coordinates, arcsec	$(B-V)_0^i$	$(V-R)_0^i$	$(V-I)_0^i$	d, pc	t, 10^6 years
1	59.3N, 0.8W	0.39	0.27	–	130	>8
2	53.8N, 24.6W	–0.03	0.00	0.32	220	5.8 ± 0.5
3	59.3N, 52.5W	–0.02	0.11	0.75	245	5.8 ± 0.6
4	53.1N, 63.5W	0.02	0.18	0.03	190	6.2 ± 0.9
5	4.4S, 63.1W	0.07	0.01	0.03	210	6.1 ± 0.9
6	22.8S, 60.2W	0.11	0.06	0.34	215	6.4 ± 0.8
7	25.7S, 29.0W	0.06	0.16	0.49	360	6.9 ± 0.2
8	46.6S, 10.0W	–0.04	0.09	0.58	170	6.6 ± 0.9
9	12.1S, 29.6E	0.02	0.01	0.19	550	5.9 ± 0.8
10	34.1S, 39.1E	0.03	–0.08	0.23	190	5 ± 2
11	39.9N, 46.8E	–0.04	–0.05	0.59	180	5.6 ± 1.9
12	6.2N, 24.6W	–0.35	–	0.10	60	<3

0.13^m, $R - I = 0.65^m \pm 0.03^m$) are comparable to those of the galactic disk (Figs. 5a–5d), suggestive of star formation in the circumnuclear region.

The color distribution in the galaxy is appreciably asymmetric. Within 2.9 kpc (50″) from the center, the northern and eastern parts of the inner disk are, on average, redder than regions to the south and west of the core by 0.1^m in $B - V$ and 0.05^m in $V - R$ (Figs. 4a–4d). However, the "red" $R - I$ color-index distribution in the galaxy remains azimuthally symmetric (Figs. 4a, 4d). The reddest regions are the core and the inner regions of the northeastern part of the bar, where the color indices reach $B - V = 0.8^m \pm 0.1^m$, $V - R = 0.60^m \pm 0.05^m$, and $R - I = 0.70^m \pm 0.05^m$ (Fig. 4a).

On average, the galaxy becomes bluer with distance from the center. However, the radial variations of $B - V$ and $V - R$ to the north and south of the core (along the major axis) differ substantially (Fig. 4a): $B - V$ decreases towards the northeast from $0.8^m \pm 0.1^m$ to $0.5^m \pm 0.1^m$ at the periphery, remaining essentially constant ($B - V = 0.65^m \pm 0.15^m$) toward the southwest of the center. $V - R$ behaves in a similar way (decreasing with distance from $0.60^m \pm 0.05^m$ to $0.40^m \pm 0.05^m$ toward the northeast and remaining constant ($0.47^m \pm 0.04^m$) toward the southwest). However, $R - I$, which is the least

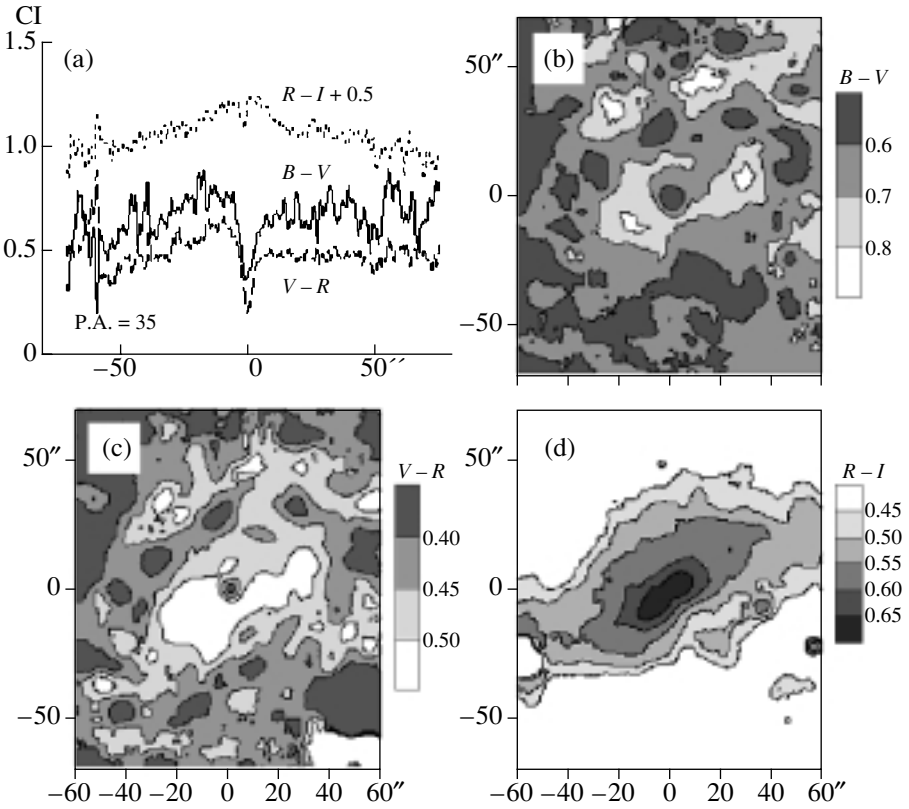

Fig. 4. (a) The color indices $B-V$, $V-R$, and $R-I$ along the major axis of NGC 3726, together with color-index maps for the galaxy in (b) $B-V$, (c) $V-R$, and (d) $R-I$.

sensitive to the presence of an absorbing medium and/or blue stars, varies almost symmetrically along the major axis of the galaxy, decreasing from $0.70^m \pm 0.05^m$ to $0.45^m \pm 0.05^m$ at the periphery (Fig. 4a). The ring of NGC 3726 is the bluest region in the galaxy. Its azimuth-averaged color indices are $B-V = 0.54^m \pm 0.06^m$, $V-R = 0.40^m \pm 0.07^m$, and $R-I = 0.46^m \pm 0.11^m$; bright local formations in the ring and the spiral arms of the outer disk are even bluer (for more detail about the sites of star formation, see Section 5).

4. PHOTOMETRIC INDICES Q

The color inhomogeneity of the galaxy, including the large-scale color asymmetry, may be due to peculiarities of the distributions of both an absorbing medium and regions of star formation. In both cases, the inhomogeneity should be most pronounced for the "blue" $B-V$ color index, as is observed. To investigate the structure of the galaxy and distinguish between these two cases, Zasov and Moiseev [18] and Bizyaev *et al.* [19] introduced a convenient photometric index Q, which combines pairs of color indices (for example, Q_{BVI}, Q_{VRI}, and so on) and is independent (ideally, at least) of selective absorption. It is assumed that the ratios of dust-related color-excesses in different photometric bands are close to those accepted for our Galaxy.

The values of the Q parameters are primarily determined by the relative luminosities of young stars, old stars, and gas in the Hα line; the chemical composition of the stellar population; and, in the presence of a burst of star formation, the characteristic age of the burst and the relative mass of the stars formed. As was shown in [19], Q_{BVI} is the most sensitive Q parameter to the presence of blue stars, while Q_{VRI} can be used to localize regions with intense Hα emission in the R band. Figures 5a and 5b present maps of the Q_{BVI} and Q_{VRI} distributions in the central region of NGC 3726.

The circumnuclear region can be distinguished in these maps, together with a number of young stars, manifest as darker regions with decreased color index. The spiral arms show less contrast in the Q map (and can be distinguished even more poorly in ordinary color maps). The fraction of radiation associated with young stars is highest in the arms, and, judging from the Q_{VRI} maps, they contain the bulk of the HII regions, leading to an increase in this index. On the whole, the disk looks more symmetric in the Q_{BVI} map than in the color maps, suggesting that the color

asymmetry of the galaxy is related to the distribution of dust rather than the distribution of young stars in the disk.

5. STAR-FORMATION SITES IN THE GALAXY

We have identified 12 bright, blue star-formation regions in the ring and spiral arms of NGC 3726. Figures 6a and 6b indicate their locations in the $(B-V)^i_0-(V-R)^i_0$ and $(B-V)^i_0-(V-I)^i_0$ two-color diagrams. We estimated the color indices by subtracting the disk background from the images of these bright regions in each filter, estimating the background in the nearest vicinity of these regions. The effective ages of the sites of star formation were derived from their locations in the two-color diagrams by using evolutionary tracks of aging stellar systems with solar chemical composition which were obtained with the PEGASE code available via the internet (dotted line). The solid line indicates the mean position of the dependence along which galaxies of various morphological types are located, according to the data of Buta and Williams [20].

The columns in Table 3 present the derived parameters of these objects: their coordinates from the center of the galaxy in arcseconds (2); $(B-V)^i_0$, $(V-R)^i_0$, and $(V-I)^i_0$ color indices (3–5), the diameter of the region in parsecs (6), and its estimated age (7). The sizes of most of the star-formation sites in NGC 3726 are 150–250 pc. In the hierarchical star-formation scale suggested by Efremov [21], such sizes are typical of stellar aggregates. All the star-formation sites (except for *1*, *12*) lie close to each other in the two-color diagrams, in the region corresponding to stellar systems with ages of 5–7 million years (Figs. 6a, 6b). The color indices of the faint regions *1* and *12* have large uncertainties, and their ages cannot be estimated reliably from our data.

6. KINEMATICS OF THE GALAXY AND MASSES OF THE COMPONENTS

The rotation curve of the galaxy $V(r)$ derived from observations of the HI line is presented in [1]. The curve $V(r)$ displays a rather unusual shape, having a maximum at $r\approx 6$ kpc (which is obviously beyond the bright bulge, for the adopted distance to the galaxy) and then increasing again somewhat more slowly at the periphery.

The inner increasing part of the rotation curve must be due to the disk, since the bulge of the galaxy is very small and the influence of the halo becomes important only in the outer regions of the galaxy. This fact, along with the presence of a local minimum in the rotation curve, presents a rare opportunity to

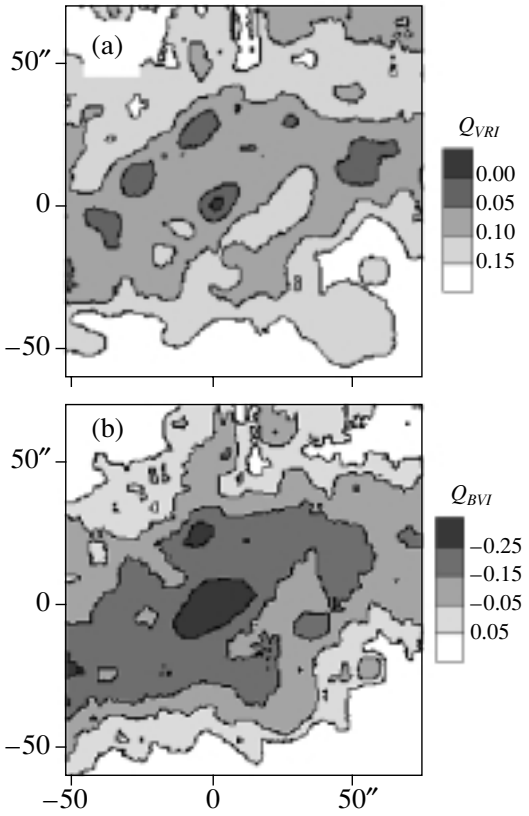

Fig. 5. Distributions of the combined parameters (a) Q_{VRI} and (b) Q_{BVI} over the disk of the galaxy.

appreciably decrease the uncertainties in the masses of the disk and halo derived by decomposing the $V(r)$ curve into corresponding components.

We will assume that the surface density of the thin disk of the galaxy matches the observed brightness distribution in the R and I bands (Table 2), varying exponentially with indices $-r/5.4$ kpc ($\approx 90''$) to $r=$ 2.9 kpc ($50''$) (the inner disk) and 3.3 kpc ($57''$) for $r>2.9$ kpc (the outer disk). Note that the photometric profile of the disk at the periphery of the galaxy ($r>180''$) displays a rapid brightness decrease with a characteristic scale slightly larger than 1 kpc [3]; however, the disk density at this distance is so small that this steepening of the profile does not affect the rotation curve, whose shape at large distances from the center is determined by the halo.

Table 4. Masses of the components of NGC 3726

r, kpc	$M_{\rm disk}$, $10^9 M_\odot$	$M_{\rm halo}$, $10^9 M_\odot$
5	16.5	3.0
10	30.5	18.5
15	35.8	54.1

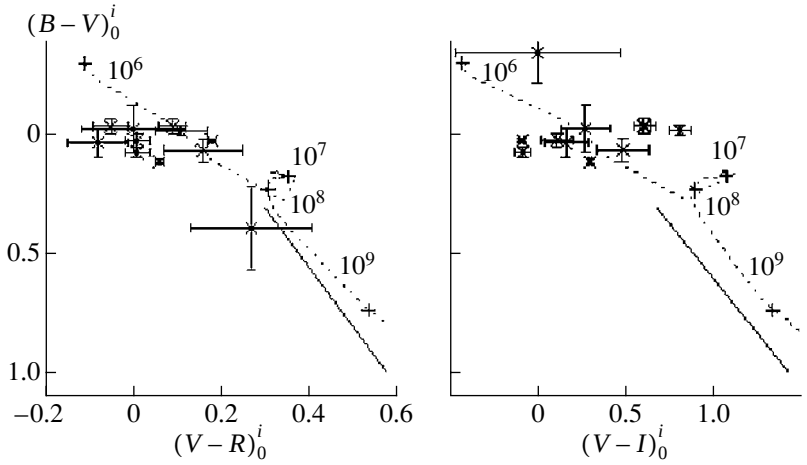

Fig. 6. $(B-V)_0^i - (V-R)_0^i$ and $(B-V)_0^i - (V-I)_0^i$ two-color diagrams for sites of star formation in the galaxy (x's). The solid line marks the mean color sequence for galaxies according to [20]. The dotted lines indicate the evolutionary tracks of a stellar system without star formation (the crosses mark positions corresponding to the ages of the system in years indicated in the diagram). The bars show the estimated errors.

In addition to the thin disk, the model includes a gaseous disk, whose surface density is assumed to be twice the HI density (to take into account the abundance of heavier elements and molecular gas); the bulge, whose density distribution is described by a King law; and a quasi-isothermal halo. We used the GR4 code written by A.N. Burlak for the modeling. Figure 7 presents the resulting decomposition of the rotation curve into components related to different parts of the galaxy.

There is no doubt that the galaxy possesses a massive dark halo (the model asymptotic velocity is about 200 km/s) responsible for the high rotational velocity at large r; however, its contribution to the total mass in the region of the rotation curve maximum is insignificant. The disk and the halo masses become equal only at $r = 12$–14 kpc, so that, despite its modest total mass, the disk of NGC 3726 can be considered to be self-gravitating in the region of the bright spirals (2–10 kpc). The mass of the bulge is too small to be estimated reliably from the shape of the rotation curve.

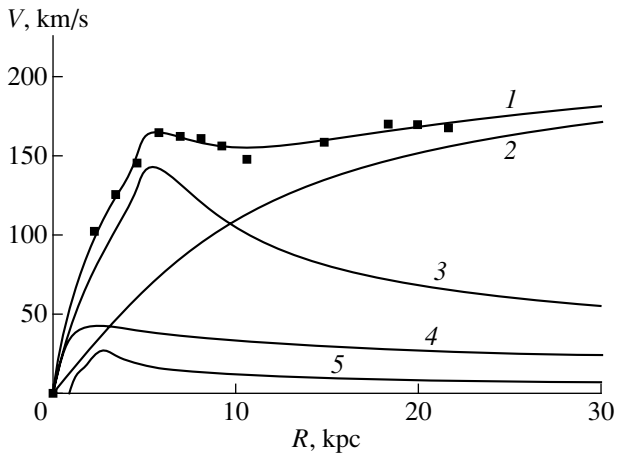

Fig. 7. Rotation curve of NGC 3726. The squares indicate the observational data and curve *1* the model curve. The components of the rotation curve related to the halo (*2*), disk *(3)*, bulge (*4*), and gas (*5*) are indicated.

The model explains the local minimum in the rotation curve, although the observed depth of the minimum is somewhat larger than in the model. Some large-scale, non-circular gas motions with low amplitudes may occur in this region (6–10 kpc from the center). Note that the region of the minimum corresponds to the distances from the center where the regular spiral pattern disappears and the extended asymmetric outer disk with floccular structure begins.

Table 4 presents the relative masses of the disk and halo inside spheres with radii 5, 10, and 15 kpc. The total mass of the stellar components of the galaxy is around $3.5 \times 10^{10} M_\odot$, which corresponds to a rather low $M/L_B ratio \approx 1.4$ for the stellar population. By varying the model parameters, we estimated the uncertainty of this value to be $\pm 20\%$.

7. CONCLUSIONS

We conclude that the asymmetry of the bar and inner disk of NGC 3726 is primarily due to an asymmetric distribution of an absorbing medium. Active star formation is underway in the ring around the bar and in the core region; the colors of the brightest blue condensations corresponds to ages of 5–7 million years. The inner and outer stellar disks can be distinguished in the galaxy; the mass of the disk

dominates that of the halo out to distances $r = 10$–13 kpc, within which the arms are regular. Thus, a regular spiral structure is formed within the stellar disk of NGC 3726, which is self-gravitating; this structure loses its regularity where the contribution of the disk to the total mass no longer dominates.

ACKNOWLEDGMENTS

This work was supported by the Russian Foundation for Basic Research, project no. 01-02-17597.

REFERENCES

1. R. Sanders and M. Verheijen, Astrophys. J. **503**, 97 (1998).
2. G. de Vaucouleurs, A. de Vaucouleurs, H. G. Corwin, *et al.*, *Third Reference Catalogue of Bright Galaxies* (Springer-Verlag, New York, 1991).
3. B. M. H. R. Wevers, P. C. van der Kruit, and R. J. Allen, Astron. Astrophys., Suppl. Ser. **66**, 505 (1986).
4. C. J. Conselice, Publ. Astron. Soc. Pac. **109**, 1251 (1997).
5. M. Shaw, D. Axon, R. Probst, and I. Gatley, Mon. Not. R. Astron. Soc. **274**, 367 (1995).
6. C. Mollenhoff and J. Heidt, Astron. Astrophys. **368**, 16 (2001).
7. R. W. Pogge, Astrophys. J., Suppl. Ser. **71**, 433 (1989).
8. P. J. Grosbol, Astron. Astrophys., Suppl. Ser. **60**, 261 (1985).
9. P. Martin, Astron. J. **109**, 2428 (1995).
10. S. Chapelon, T. Contini, and E. Davoust, Astron. Astrophys. **345**, 81 (1999).
11. L. Martinet and D. Friedli, Astron. Astrophys. **323**, 363 (1997).
12. P. W. Hodge, Astron. J. **87**, 1341 (1982).
13. A. Landolt, Astron. J. **88**, 853 (1983).
14. S. van den Bergh, Astron. J. **110**, 613 (1995).
15. Z. Frei, P. Guhathakurta, J. E. Gunn, and J. A. Tyson, Astron. J. **111**, 174 (1996).
16. K. C. Freeman, Astrophys. J. **160**, 811 (1970).
17. P. Prugniel and P. Heraudeau, Astron. Astrophys., Suppl. Ser. **128**, 299 (1998).
18. A. V. Zasov and A. V. Moiseev, Pis'ma Astron. Zh. **24**, 677 (1998) [Astron. Lett. **24**, 584 (1998)].
19. D. V. Bizyaev, A. V. Zasov, and S. S. Kaĭsin, Pis'ma Astron. Zh. **27**, 254 (2001) [Astron. Lett. **27**, 217 (2001)].
20. R. Buta and K. L. Williams, Astron. J. **109**, 543 (1995).
21. Yu. N. Efremov, *Sites of Star Formation in Galaxies* [in Russian] (FM, Moscow, 1989).

Translated by K. Maslennikov

Astronomy Reports, Vol. 46, No. 9, 2002, pp. 712–720. Translated from Astronomicheskiĭ Zhurnal, Vol. 79, No. 9, 2002, pp. 787–797.

*BVRI*Hα CCD Photometry of the Spiral Galaxy NGC 3184

A. S. Gusev[1, 2, 3, 4] and S. S. Kaĭsin[5]

[1] *Sternberg Astronomical Institute, Universitetskiĭ pr. 13, Moscow, 119899 Russia*

[2] *Kyungpook National University, Taegu 702-701, Korea*

[3] *Institute of Solid State Physics, P.O. Chernogolovka, Moscow region, 142432 Russia*

[4] *Astronomy Data Center, University of Cambridge, Cambridge, Great Britain*

[5] *Special Astrophysical Observatory, Russian Academy of Sciences, Nizhniĭ Arkhyz, Karachaevo-Cherkesskaya Republic, 357147 Russia*

Received November 19, 2001; in final form, February 1, 2002

Abstract—We have carried out *BVRI*Hα CCD surface photometry of the spiral galaxy with active star formation NGC 3184 using the 1-m telescope of the Special Astrophysical Observatory. *B* and Hα data from the ING Archive (La Palma Observatory) were also used. We consider the structure and radial brightness distribution of the galaxy. Stellar populations in different regions of the galaxy are analyzed using two-color diagrams. We have identified and studied star-forming regions in NGC 3184 and estimated their ages based on evolutionary modeling. © *2002 MAIK "Nauka/Interperiodica"*.

1. GENERAL INFORMATION

NGC 3184 is a relatively nearby, late-type barred spiral galaxy viewed face-on (Fig. 1). Table 1 presents the basic parameters of the galaxy taken from the RC3 Catalog [1].

NGC 3184 has been studied relatively thoroughly, but its morphology and the photometric properties of its components in the *VRI* bands had not been analyzed in detail. NGC 3184 displays a diffuse core [2, 3] with signs of activity, e.g., Hα emission [2]. The brightness of the galactic disk falls off exponentially; the characteristic scale for the disk given by *V* photometry is 74″ [45], while *R* photometry yields 115″ [5]. The galaxy possesses a massive bulge whose brightness decreases in accordance with a de Vaucouleurs law with effective radius 38″ [4]. The bulge luminosity is 6% of the integrated luminosity of the galaxy [5]. Two bright symmetrical spiral arms branch in the outer disk of NGC 3184, forming several long extended arms [6]. A short (semi-major axis 0.4′), broad ($b/a = 0.95$) bar is visible [7–10], whose brightness also falls off exponentially [9, 10]. According to the calculations of [11], the bar is relatively young (10^8 years).

More than 100 HII regions—sites of star formation—have been identified in the galaxy (see the catalog of Hodge [12]). 32 HII regions in NGC 3184 have been studied in detail spectrophotometrically [13–15]. *UBVRI*Hα photometry has been carried out for 13 young clusters in the galaxy [16, 17].

According to [18], the mass of gas in the galaxy is $M(\mathrm{HI}) = 1.8 \times 10^9 M_\odot$ and $M(\mathrm{H_2}) = 8.0 \times 10^8 M_\odot$. The IR luminosity of NGC 3184 is rather high: $L(\mathrm{FIR}) = 2.1 \times 10^9 L_\odot$ and $L(\mathrm{FIR})/L(B) = 0.24$. The mass of dust in the galaxy is $1.2 \times 10^6 M_\odot$ [18].

ROSAT 0.1–2.0 keV observations indicated an excess of radiation by hot gas beyond the optical boundary of the galaxy, as is especially characteristic of gas with temperatures $T \approx 10^6$ K [19]. The supernova rate in NGC 3184 estimated in [19] ($1/30\ \mathrm{yr}^{-1}$) is consistent with the observations: four supernova

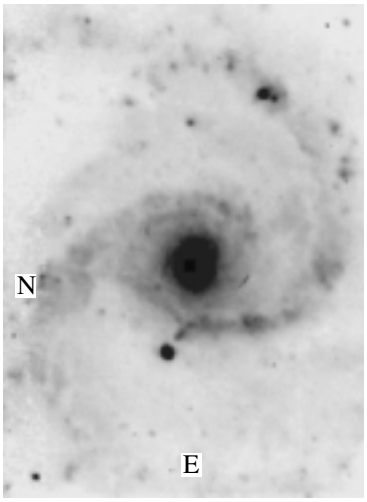

Fig. 1. *V* CCD image of NGC 3184. The size of the area is 2.4′ × 3.5′.

1063-7729/02/4609-0712$22.00

outbursts (1921B, 1921C, 1937F, and 1999gi) have been detected over the last century [20, 21].

2. OBSERVATIONS AND REDUCTION

NGC 3184 was observed on January 21–22, 1998, with the 1-m Zeiss-1000 telescope of the Special Astrophysical Observatory (focal length 13.3 m) using a permanently mounted CCD photometer [22]. The photometric system of the K585 CCD camera with V, R, and I broadband filters is close to the standard VRI Johnson–Cousins system. The size of the CCD is 530 × 580 pixels, which provides a 143″ × 212″ field of view for an image scale of 0.28″/pixel × 0.37″/pixel.

Five exposures were made in each filter. Between exposures, the telescope was shifted by several arcseconds to decrease the impact of flaws in the CCD. The duration of one exposure in each filter was 600 s. The seeing was 2.5″–3.0″.

The photometric calibration was carried out using standard stars from the list of [23] (PG0220, PG1407, RU149, S101429), which were observed on the same night. We also used the galactic aperture photometry data of the catalog [24]. The data of [15] were used to calibrate the Hα image.

The preliminary reduction of the images was performed at the Special Astrophysical Observatory. To take into account the electronic bias and the influence of hot pixels, a dark frame was subtracted from the frames obtained for the target and standard stars. This dark frame was averaged from several closed-shutter exposures made with the same integration time as for the target. For the flat field, we used twilight sky integrated in each filter with signal-to-noise ratio no lower than 60–80. All the images were divided by a flat field to take into account the inhomogeneous sensitivity of the detecting elements.

We used B and Hα images of NGC 3184 taken from the archive of the Isaac Newton Group (Astronomy Data Center, University of Cambridge, Great Britain), obtained using the telescopes of La Palma Observatory. The B image was obtained on March 5–6, 1999, at the Cassegrain 1 : 25 focus of the 1-m Jacob Kapteyn Telescope, with the JAC 1124 × 1124 CCD. The field of the CCD was 338″ × 338″, with an image scale of 0.″33/pixel. The duration of the exposure was 900 s. The Hα image of NGC 3184 ($\lambda_0 =$ 6577 Å) was acquired on January 15–16, 1998 with the 4.2-m William Hershel Telescope (Cassegrain focus), using a TEK-5 CCD array. The size of the CCD was 1124 × 1124 pixel, with an image scale of 0.″30/pixel. The duration of the exposure was 900 s.

Further, all images were processed at the Sternberg Astronomical Institute using the standard ESO MIDAS procedures. The basic stages of the image processing were as follows.

(a) Reducing the images to a single scale (0.37″/pixel) and bringing the images of the galaxy into coincidence with an accuracy of up to 0.1 pixel. Shifting the images between consecutive frames made it possible to effectively eliminate the influence of cosmic ray tracks, individual "hot" pixels, and "bad" columns of the K585 array.

(b) Summing the images of the galaxy made in a single filter.

(c) Correcting for the air mass.

(d) Determining the sky background and subtracting it.

(e) Translating the readings onto a logarithmic scale (magnitudes per square arcsecond) in accordance with the photometric calibration (for the Hα image of the galaxy, relative calibration with a conventional zero point was carried out).

(f) Correcting for differences between the instrumental photometric systems and the standard Johnson–Cousins system (taking into account the color equations obtained).

(g) Subtracting the images obtained in different filters, i.e., color-index mapping of the galaxy.

The sky background for the V, R, and I images of the galaxy was determined from the images of other galaxies obtained on the same night, with corrections

Table 1. Basic parameters of NGC 3184

Parameter	Value
Type	SBc
m_B, mag	10.42
$M_B^{0,i}$, mag	−19.81
V_{LG}, km/s	605
R, Mpc ($H_0 = 75$ km s^{-1}Mpc^{-1})	8.07
D_{25}, arcmin	7.85
i, deg	24.2
PA, deg	135

Table 2. Reddening due to Galactic absorption and absorption due to the inclination of NGC 3184

Color index	E	E_i
$B-V$	0.06	0.009
$V-R$	0.03	0.004
$R-I$	0.04	0.006

for the time of observation and the air mass. The accuracy of the photometric calibration was 0.07^m in B, 0.05^m in V and R, and 0.02^m in I. The relative accuracy for the Hα flux determination was 20%.

All the data (brightness, color indices, Hα luminosity) were corrected for Galactic absorption, and the data for the two-color diagrams and the analysis of the color characteristics of site of star formation in the galaxy were also corrected for absorption due to the inclination of NGC 3184. The correction was introduced according to the standard procedure adopted in the RC3 Catalog [1]. Table 2 presents the absorption in various filters.

Given the accepted distance to the galaxy, the image scale is 14.5 pc/pixel.

3. RESULTS

The size of NGC 3184 exceeds the field of our CCD array. As a result, we are not able to study the ends of the spiral arms and the outer regions of the disk of the galaxy here.

3.1. Photometric Profiles and Morphology of the Galaxy

NGC 3184 possesses a large, bright core (Figs. 2a, 2b). We estimate its diameter to be 0.5 kpc (13″); however, it is not possible to draw a distinct line of demarcation between the core and bulge of the galaxy. The Hα luminosity of the core region within 6.5″ of the center is $3.6 \times 10^5 L_\odot$.

The bulge can be seen out to 0.51 kpc (15″) from the center. The short, faint bar of NGC 3184 is almost perpendicular to its major axis (Fig. 2c). The semimajor axis of the bar is 0.9 kpc (23″), and its position angle is PA $= 90° \pm 2°$ (Fig. 3b). The brightness falls off exponentially along the bar major axis (Fig. 2b); however, it is difficult to distinguish the short bar against the bright bulge. The mean V surface brightness of the bar is 20.8 ± 0.1^m/arcsec^2. At the eastern edge of the bar, the brightness locally increases to $\mu_V = 20.70 \pm 0.05^m$/arcsec^2 (Figs. 2b–2d).

Two bright, weakly-curved spiral arms emerge from the edges of the bar (Figs. 1, 2c, 2d). The arm emerging from the eastern end of the bar (the southern arm) is, on average, 0.2^m/arcsec^2 brighter in V than the northern arm; the surface brightnesses of the arms μ_V are 21.2 ± 0.6 and 21.4 ± 0.6^m/arcsec^2, respectively. Both spiral arms display numerous bright regions with V surface brightnesses up to 19.1^m/arcsec^2 and diameters from 100 to 300 pc (from 3″ to 7″)—sites of active star formation. Some dust lanes are visible along the spiral arms (Fig. 1). Apart from the two main spiral arms, the galaxy also possesses several fainter arms (Figs. 1, 2c, 2d). The V surface brightness of the disk of NGC 3184 does not exceed 22.0^m/arcsec^2.

A very bright star-like object located 1.7 kpc (44″) to the east of the core of NGC 3184 (Figs. 1, 2c, 2d) is of considerable interest. Its maximum V brightness reaches 17.0^m/arcsec^2, and its diameter is 260 pc (6.5″). Figures 1 and 2c, 2d clearly show a bright bridge about 250 pc (6.3″) in length extending from the spiral arm towards the galaxy.

The Hα emission is primarily observed in the core, the circumnuclear region, and the spiral arms of the galaxy (Fig. 2d). The intensity of the emission from these regions exceeds 1.5×10^{-17} erg s^{-1}cm^{-2}, reaching $(3–4) \times 10^{-16}$ erg s^{-1}cm^{-2} in the core and in the bright region in the spiral arm to the southwest of the center of NGC 3184.

We were able to study the dependence of the isophote ellipticity and position angle on distance from the center of the galaxy with good accuracy only within 2.3 kpc (60″) of the center. In the central regions ($r < 30″$), the isophotes are essentially circular ($e = 0.10 \pm 0.05$), and the position angle is PA $= 87° \pm 15°$ (Figs. 3a, 3b). For more distant regions, the $e(r)$ and PA(r) dependences are appreciably affected by the bright spiral arms. It is likely that the difference between the ellipticity of the B isophotes and of isophotes at longer wavelengths (Fig. 3a) is related precisely to this. In long-wavelength bands, the isophote ellipticity increases to 0.51 ± 0.02 by $r = 45″$, then decreases slightly (Fig. 3a). The position angle of the galaxy increases smoothly to $22° \pm 6°$ (Fig. 3b). We obtained the overall value $e = 0.23 \pm 0.07$, which corresponds to an inclination for NGC 3184 of $i = 40° \pm 6°$.

Figure 4 presents azimuthally averaged photometric profiles of NGC 3184 derived using the obtained b/a and PA values. The local brightness increase at $r = 44″$ is related to the bright star-like object described above. The profiles indicate some differences between the characteristics of the inner and outer regions of the disk. The decrease in the disk brightness at $r = 20″–38″$ is consistent with an exponential law with scale 1.14 ± 0.02 kpc ($29.2 \pm 0.4″$) and $\mu_V(0) = 20.12 \pm 0.15^m$/arcsec^2. At $r = 50″–78″$, the characteristic scale of the exponential decrease in the disk brightness is 2.02 ± 0.17 kpc ($51.7″ \pm 4.5″$), and the central surface brightness is $\mu_V(0) = 20.77 \pm 0.13^m$/arcsec^2. When the profiles of the central regions are decomposed into the disk and bulge, it is apparent that the main contribution to the luminosity at $r = 4″–12″$ is made by the bulge. The decrease in the bulge brightness follows a de Vaucouleurs law with effective radius

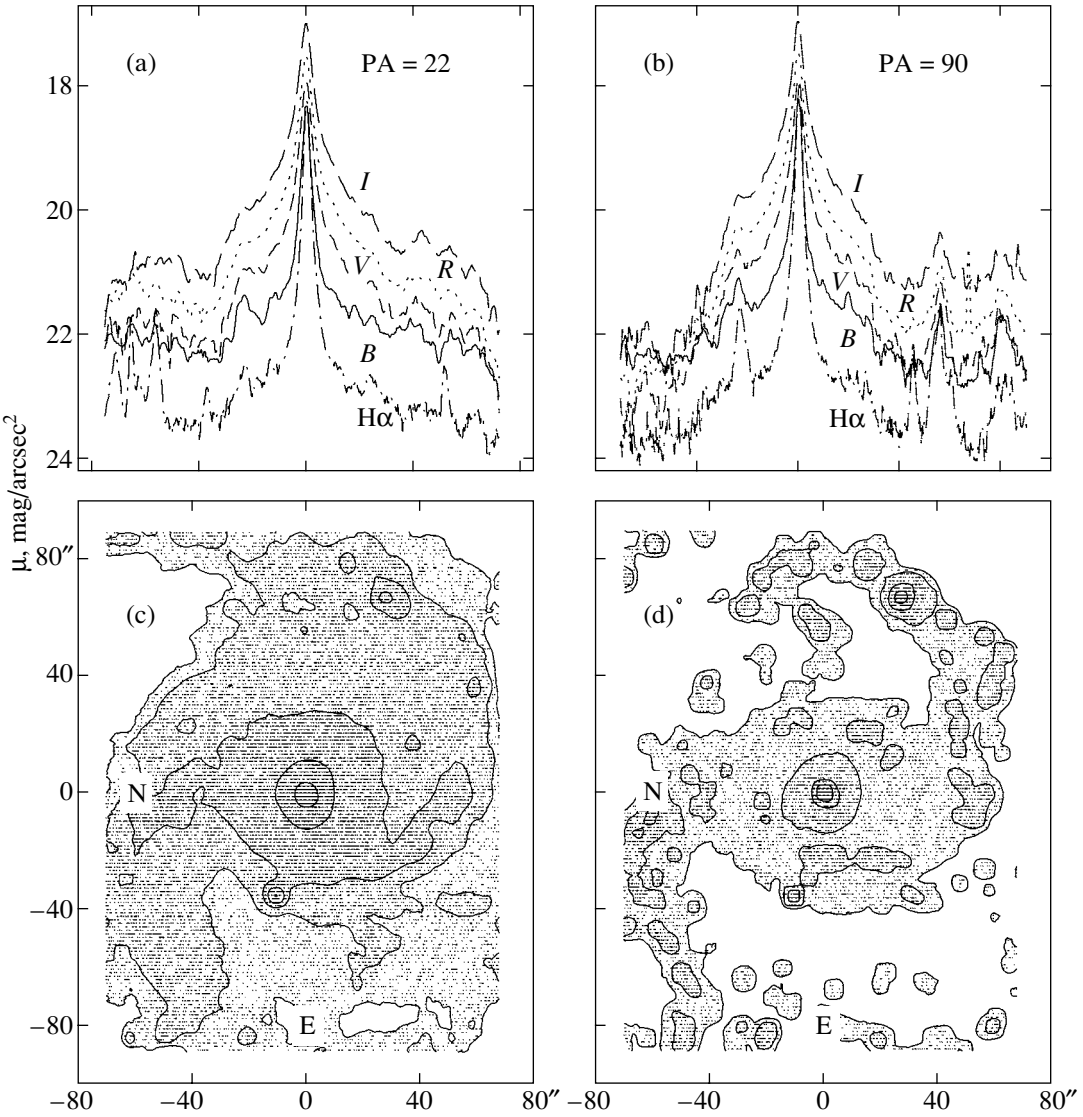

Fig. 2. Photometric profiles (a) along the major axis of the galaxy and (b) along the major axis of its bar in B (solid line), V (short-dashed line), R (dotted line), I (long-dashed line), and Hα (dash-dot line), and images of the galaxy in (c) V and (d) Hα. We have adopted $m_{\mathrm{H}\alpha}(0) = 18^m/\mathrm{arcsec}^2$ for the Hα photometric profiles. The 19.5, 20.5, 21.5, 22.5, and 23.5 isophotes (c) and contours of equal flux at 1.5, 3, 10, and 30×10^{-17} erg s^{-1}cm^{-2} (d) are shown.

0.91 ± 0.14 kpc ($23.2'' \pm 3.7''$) and $\mu_V(r_e) = 25.36 \pm 0.77^m/\mathrm{arcsec}^2$. A King model does not satisfy the observational data for the bulge of NGC 3184. The brightness of the outer disk falls off slightly faster in the I band than in the V and R bands, while the B-band brightness remains virtually constant with distance (Fig. 4). This is due to the presence of a number of bright, blue star-forming regions in the outer disk. As will be shown in Section 3.2, generally speaking, NGC 3184 displays an anomalously large gradient of $B - V$ along the galactic radius.

3.2. Color Distribution

The galaxy as a whole is blue: according to [1, 25], the integrated color indices are $B - V = 0.52 \pm 0.10^m$, $V - R = 0.40 \pm 0.02^m$, and $R - I = 0.50 \pm 0.03^m$. The core of NGC 3184 is moderately red ($B - V = 0.85 \pm 0.10^m$, $V - R = 0.51 \pm 0.07^m$, and $R - I = 0.59 \pm 0.07^m$). The bulge and inner parts of the bar are the reddest regions in NGC 3184 (Figs. 5a–5e). The color indices of the bulge are $B - V = 0.9 \pm 0.1^m$, $V - R = 0.58 \pm 0.03^m$, and $R - I = 0.62 \pm 0.05^m$ (Fig. 5a). The average color indices of the bar are $B - V = 0.65 \pm 0.15^m$, $V - R = 0.54 \pm 0.04^m$, and $R - I = 0.60 \pm 0.03^m$ (Fig. 5b); on average, the bar becomes bluer with distance from

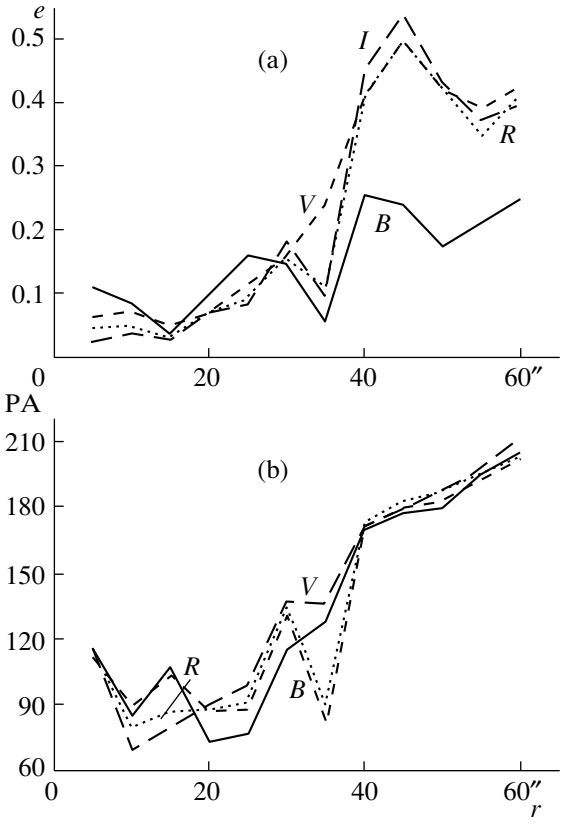

Fig. 3. (a) Isophote ellipticity $e = 1 - b/a$ and (b) position angle of the galaxy PA as a function of the distance r to the center of NGC 3184 in B, V, R, and I.

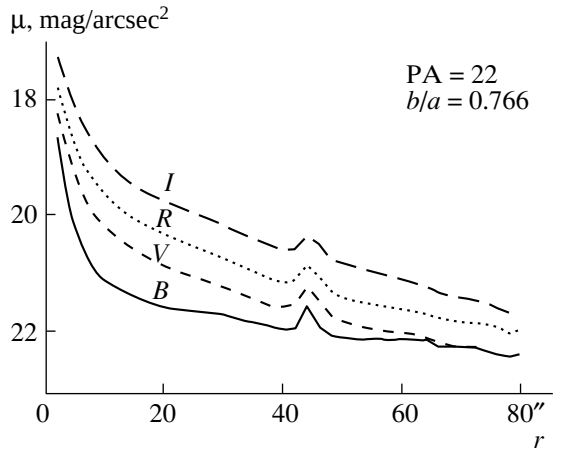

Fig. 4. Mean photometric profiles of NGC 3184 in B, V, R, and I.

the center. The color indices of the disk vary within fairly broad limits. On average, for the disk, $B - V = 0.3 \pm 0.2^m$, $V - R = 0.4 \pm 0.1^m$, and $R - I = 0.55 \pm 0.15^m$ (Figs. 5c–5e). The spiral arms of the galaxy are blue: $B - V = 0.35 \pm 0.10^m$, $V - R = 0.35 \pm 0.05^m$, and $R - I = 0.50 \pm 0.05^m$; the northern and southern spiral arms display the same colors within the errors. The bluest areas in NGC 3184 are bright regions in spiral arms that correspond to sites of star formation. Their photometric characteristics will be considered in detail in Section 3.4.

The large radial gradient of $B - V$ in NGC 3184 is noteworthy (Figs. 5a, 5b). This color index decreases from 0.9 ± 0.1^m in the bulge region (0.3 kpc from the center) to 0.3 ± 0.1^m in the disk region (1.2 kpc from the center).

In general, the distribution of brightness and color in the galaxy is symmetric.

3.3. Two-Color Diagrams

Figure 6a, 6c presents the positions of various regions of NGC 3184 in $(B-V)_0^i - (V-R)_0^i$ and $(B-V)_0^i - (V-I)_0^i$ two-color diagrams. The numbers on the graph denote: 1—the core within 250 pc (6.5″) from the galactic center; 2—the bulge at $r =$ 270–590 pc (7″–15″); 3—the entire galaxy (the integrated color indices are taken from [1, 25]); 4—the spiral arms; 5—the disk; 6–8— bar regions at $r =$ 660, 740, and 820 pc (17″, 19″, and 21″), respectively.

The data in the two-color diagrams have been corrected for absorption due to the inclination of NGC 3184; this is why the color indices for various regions do not coincide with the data presented in Subsection 3.2. Table 2 presents the differences between these values, i.e., the reddening due to the inclination of NGC 3184.

In the $(B-V)_0^i - (V-R)_0^i$ and $(B-V)_0^i - (V-I)_0^i$ diagrams, the dots corresponding to the color indices of various components of the galaxy are located primarily along the normal integrated color sequence (NCS) for galaxies. This testifies to a standard star-formation history in NGC 3184: exponential damping of the star-formation rate at some distance from the center of the galaxy. There is virtually no star formation in the bulge of NGC 3184: its color indices correspond to an aging, metal-deficient stellar system with a characteristic age of several million years. Weak star formation continues in the core of NGC 3184. Active star formation is observed in the spiral arms, the disk, and the outer regions of the bar. The deviation of the color indices of the spiral arms and disk of NGC 3184 to the right of the NCS (points 4 and 5 in Fig. 6a, c) may be due to recent bursts of star formation in these regions—an excess young stellar population compared to the standard population of spiral galaxies is observed. The bar becomes noticeably bluer with distance from the center along the NCS (points 6–8), indicating an increase in the fractional young stellar population toward the periphery of the bar.

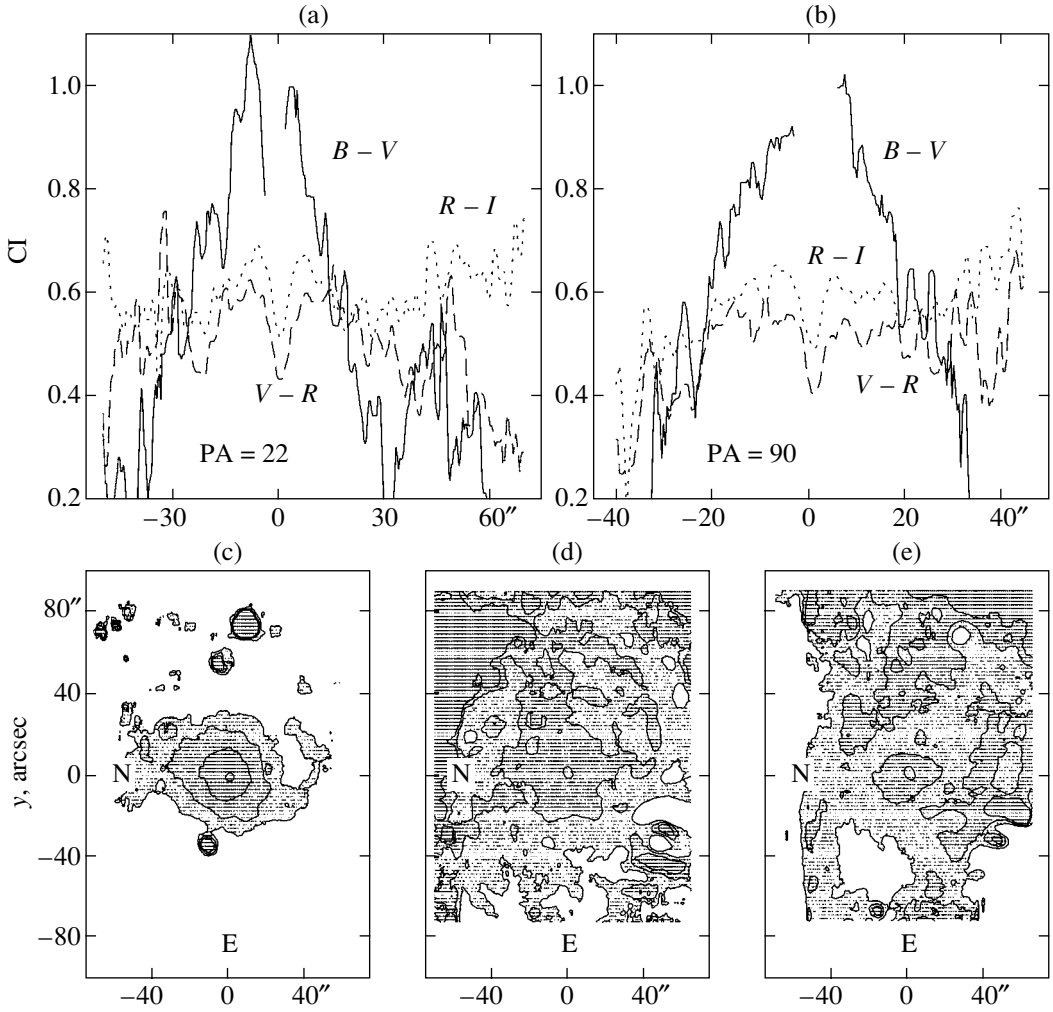

Fig. 5. The $B-V$ (solid line), $V-R$ (short-dashed line), and $R-I$ (dotted line) color indices (a) along the major axis of the galaxy and (b) along the major axis of the bar, together with maps of the (c) $B-V$, (d) $V-R$, and (e) $R-I$ color indices. Contours of equal color indices of 0.4, 0.6, and 0.8 (c); 0.3, 0.5, and 0.7 (d); and 0.4, 0.6, and 0.8 (e) are indicated; the dark intervals correspond to larger color indices.

The star-formation rate (SFR) in NGC 3184 is fairly high: SFR $= 1.4 \pm 0.1 M_\odot$/year according to IR observations and $0.5 \pm 0.05 M_\odot$/year according to Hα observations [11, 18]. The star-formation efficiency (SFE) in the galaxy is SFE $= (5.6 \pm 0.2) \times 10^{-10}$ year^{-1} from IR observations and SFE $= (1.4 \pm 0.1) \times 10^{-10}$ year^{-1} from Hα observations [11, 18].

3.4. Sites of Star Formation in the Galaxy

We have identified 13 modest star-like and diffuse blue formations in the outer regions of the disk and in the spiral arms of NGC 3184. Their position in the $(B-V)_0^i - (V-R)_0^i$ and $(B-V)_0^i - (V-I)_0^i$ two-color diagrams is shown in Figs. 6b, 6d. The columns of Table 3 present the derived parameters for these objects: (2) their coordinates relative to the galactic center in arcseconds, (3)–(5) $(B-V)_0^i$, $(V-R)_0^i$, and $(V-I)_0^i$ color indices, (6) Hα luminosity $10^3 L_\odot$, (7) the diameter of the region in parsecs, and (8) their age in units of 10^6 yrs. When deriving the color indices of the regions, we determined their brightnesses in each filter by subtracting the background radiation of the surrounding disk from the radiation coming from the region of the site of star formation. The ages of the star-forming regions were estimated from their positions in the two-color diagrams, using evolutionary tracks for aging stellar systems with $Z = Z_\odot$ obtained with the PEGASE2 code [2].

The average size of the star-forming regions in NGC 3184 is 120–170 pc. Some star-forming regions in the galaxy display complex hierarchical structures: two to three brighter regions with diameters of 120–180 pc are visible within regions

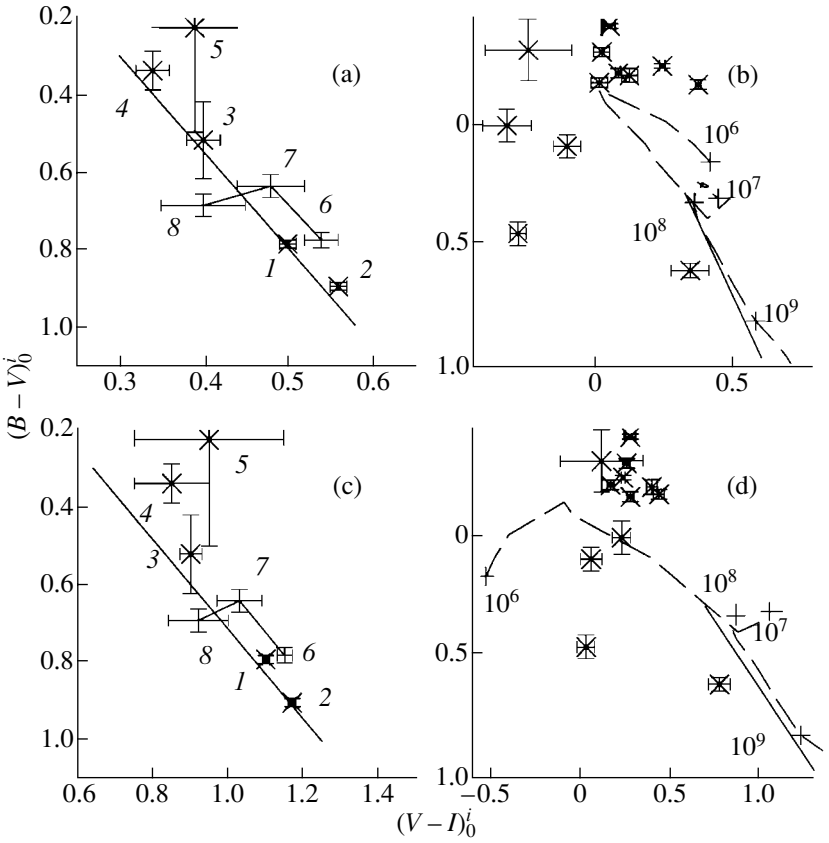

Fig. 6. (a, b) $(B-V)^i_0-(V-R)^i_0$ and (c, d) $(B-V)^i_0-(V-I)^i_0$ two-color diagrams for (a, c) some regions of NGC 3184 and (b, d) sites of star formation in the galaxy. The straight solid lines represent the normal color sequences (NCS) for galaxies, according to [25]. The broken solid lines in the left graphs indicate variations of the color indices along the major axis of the bar. The dashed curves in the right graphs are evolutionary tracks for a stellar system without star formation and with $Z = 0.02$ (the age in years is indicated). The errors are indicated. The shift due to selective dust absorption is parallel to the NCS. The numbers denoting different regions of NGC 3184 are explained in the text.

230 ± 60 pc in size; this is true, for example, of star-forming regions 8 and 10 (see Table 3). The sizes of most sites of star formation in NGC 3184 are typical of stellar associations; the sizes of two regions (3, 5) indicate that they are stellar aggregates (according to the hierarchical star-formation scale of Efremov [27]).

In the $(B-V)^i_0-(V-R)^i_0$ and $(B-V)^i_0-(V-I)^i_0$ two-color diagrams, a substantial fraction of the star-forming regions are located along the evolutionary track of a young stellar system with an age of about $(3–7)\times 10^6$ yrs. Some clusters are located appreciably above this track (Figs. 6b, 6d). This may indicate a significant contribution from non-stellar radiation associated with these star-forming regions, such as radiation by hot gas. Clusters 5 and 13 in the diagrams are situated to the left of the evolutionary track, possibly due the fact that we have not taken dust into account in these regions. The luminosity of most of the objects is $L(\mathrm{H}\alpha) = (1–4)\times 10^4 L_\odot$.

Region 3 is the bright star-like object that is connected to the central regions of the galaxy by a bridge (see Section 3.1). Judging from its photometric parameters and intense Hα radiation (Table 3), this object is a stellar aggregate with a diameter of 260 pc. The position of region 3 in the two-color diagrams indicates that it may be a young object with very strong selective absorption, $(E(B-V) = 1.5^m)$. This is also supported by the fact that the infrared color indices of the region obtained from JHK photometry from the 2MASS survey are $J-H = 0.33^m \pm 0.10^m$ and $H-K = 0.07^m \pm 0.10^m$, which corresponds to an age of $(6.8 \pm 1.3)\times 10^6$ yrs.

Object 8 (probably the youngest of those studied) is distinguished by its very intense Hα luminosity, $1.68\times 10^5 L_\odot$ (46% of the core luminosity of NGC 3184).

We have not been able to determine the age of region 2 with confidence, due to the absence of data on selective absorption in this region. In the absence of appreciable absorption, the age of the stellar population of this region is $(6.5–30)\times 10^8$ yrs (depending on the chemical composition). It is possible that we

Table 3. Parameters of sites of star formation in the galaxy

No.	Coordinates, arcsec	$(B-V)_0^i$	$(V-R)_0^i$	$(V-I)_0^i$	$L(\mathrm{H}\alpha)$, $10^3 L_\odot$	d, pc	t, 10^6 yrs
1	59.6N, 4.9E	−0.31	−0.27	0.07	17	80	4.8 ± 1.0
2	70/2N, 43.7E	0.63	0.32	0.72	16	155	7.5–3000
3	10.5N, 31.2E	1.26	0.12	0.32	41	260	6.8 ± 1.3?
4	37.2S, 18.9E	0.01	−0.35	0.18	9	140	5.5 ± 0.3
5	50.7S, 1.9E	0.10	−0.13	0.01	27	235	5.0 ± 1.0
6	58.4S, 35.5W	−0.30	0.00	0.21	11	120	4.8 ± 1.0
7	55.1S, 53.8W	−0.17	−0.01	0.39	14	120	5.3 ± 1.4
8	27/6S, 67.7W	−0.24	0.22	0.19	168	170	4.3 ± 1.3
9	14.1S, 78.4W	−0.20	0.10	0.35	29	120	4.8 ± 1.5
10	1/3N, 56.0W	−0.21	0.06	0.12	25	140	4.7 ± 1.0
11	7.9N, 78.4W	−0.16	0.35	0.23	32	160	5.0 ± 2.1
12	25.5N, 64.1W	−0.41	0.03	0.23	14	120	4.8 ± 1.1
13	49/3N, 17.5W	0.47	−0.31	−0.02	11	140	<5

are dealing here with a moderately old stellar cluster or a dwarf galaxy.

Larsen [17] studied 13 other young stellar clusters in NGC 3184 in the U, B, V, and I bands. We derived the ages of these objects from his $U-B$, $B-V$, and $V-I$ color indices using model evolutionary tracks calculated with the PEGASE2 code [26]. Table 4 presents the resulting ages. For at least ten of the objects studied by Larsen [17], the ages are similar to those of the sites of star formation considered here.

As was already noted in Section 1, about 100 HII regions are known in NGC 3184. Here, we were not able to use the spectrophotometric observations of HII regions from [13–14], since those regions are situated near the periphery of the galaxy and lie outside the field of view of our CCD camera. However, there are also many HII regions in the inner region of the galaxy (Fig. 2d). Their sizes are 2″–8″ (80–310 pc), which correspond to stellar associations and aggregates (according to the classification of Efremov [27]). It is possible that the galaxy contains HII regions smaller than 2″, but we cannot test this due to the insufficient quality of our Hα images. Several groups of close HII regions are seen, which form chains and rings. The characteristic scale for these formations is 12″–20″ (480–800 pc), which corresponds to the sizes of stellar complexes [27], and is also the characteristic width of the spiral arms of NGC 3184 (Fig. 2d).

4. DISCUSSION

On the whole, NGC 3184 is a typical late-type galaxy with ongoing star formation in the disk and possibly in the core. The star formation in the galaxy is of a quiescent (non-burst) type. An appreciable fraction of young stars are located in compact star-forming regions. At least three spatial star-formation scales can be recognized in NGC 3184: (1) chains and rings with characteristic sizes 500–800 pc, (2) diffuse and star-like regions with diameters of 200–300 pc, and (3) star-like regions with diameters of 80–200 pc. These results are consistent with the hierarchical scale of star-formation suggested by

Table 4. Ages of young stellar clusters in NGC 3184

No.	Name (from [17])	t, 10^6 yrs
1	n3184–105	6.6 ± 0.4
2	353	6.3 ± 0.9
3	383	6.8 ± 0.3
4	475	6.3 ± 1.0?
5	568	5.9 ± 0.4
6	788	7.4 ± 0.2
7	870	7.3 ± 0.9
8	878	250 ± 60
9	909	6.8 ± 0.9
10	1053	6.5 ± 0.5
11	1070	5.9 ± 0.4
12	1137	8.2 ± 0.8
13	1316	6.2 ± 0.2

Efremov [27] (complexes–aggregates–associations); however, no distinct boundary between stellar aggregates and associations can be seen in NGC 3184. Both star-like aggregates and aggregates containing several stellar associations are seen in the galaxy; both types of aggregates display the same color indices.

The ages of the young star-forming regions in the galaxy are $(4–7) \times 10^6$ yrs, possibly due to a selection effect, if this is the age at which clusters of a given equal mass display the maximum B luminosity.

Spectrophotometric observations are needed to clarify the nature of the bright star-like object located in the eastern part of the galaxy. Our data do not provide an unambiguous answer to the question of whether the object is a field star or belongs to NGC 3184. The origin of the bridge toward the object also remains unclear. Clarification of these issues requires analyses of the kinematics of the galaxy, and, most of all, mapping of the velocity field of NGC 3184. Thus, in spite of the large volume of data already available for NGC 3184, supplementary studies are needed.

5. CONCLUSIONS

(1) The disk brightness of NGC 3184 decreases exponentially with a characteristic scale of $51.7'' \pm 4.5''$ (2.02 ± 0.17 kpc); the brightness of the bulge decreases according to a de Vaucouleurs law with effective radius $23.2'' \pm 3.7''$ (0.91 ± 0.14 kpc).

(2) The galaxy displays active, though quiescent (non-burst), star formation, i.e., star formation occuring at a constant rate. The only region where star formation is not currently observed is the bulge.

(3) Three scales of star-formation can be distinguished: complexes (characteristic size 500–800 pc), aggregates (200–300 pc), and associations (80–200 pc). The ages of the brightest star-formation regions in the galaxy are $(4–7) \times 10^6$ yrs.

ACKNOWLEDGMENTS

The authors are grateful to A.V. Zasov (Sternberg Astronomical Institute) for useful discussions and comments, and to D.V. Bizyaev (Sternberg Astronomical Institute) for the preliminary reduction of the observations. This work was partially supported by the Russian Foundation for Basic Research, project nos. 98-02-17102, 01-02-16800, and 01-02-17597. This study was based partially on data from the Isaac Newton Group Archive (Cambridge).

REFERENCES

1. G. de Vaucouleurs, A. de Vaucouleurs, H. G. Corwin, *et al.*, *Third Reference Catalogue of Bright Galaxies* (Springer-Verlag, New York, 1991).
2. R. W. Pogge, Astrophys. J., Suppl. Ser. **71**, 433 (1989).
3. S. van den Bergh, Astron. J. **110**, 613 (1995).
4. W. E. Baggett, S. M. Baggett, and K. S. J. Anderson, Astron. J. **116**, 1626 (1998).
5. P. J. Grosbol, Astron. Astrophys., Suppl. Ser. **60**, 261 (1985).
6. D. M. Elmegreen and B. G. Elmegreen, Astrophys. J. **314**, 3 (1987).
7. P. Martin and J.-R. Roy, Astrophys. J. **424**, 599 (1994).
8. P. Martin, Astron. J. **109**, 2428 (1995).
9. D. M. Elmegreen, B. G. Elmegreen, F. R. Chromey, *et al.*, Astron. J. **111**, 1880 (1996).
10. D. M. Elmegreen, B. G. Elmegreen, F. R. Chromey, *et al.*, Astron. J. **111**, 2233 (1996).
11. L. Martinet and D. Friedli, Astron. Astrophys. **323**, 363 (1997).
12. P. W. Hodge, Astron. J. **87**, 1341 (1982).
13. M. L. McCall, P. M. Rybski, and G. A. Shields, Astrophys. J., Suppl. Ser. **57**, 1 (1985).
14. D. Zaritsky, R. C. Kennicutt, Jr., and J. Huchra, Astrophys. J. **420**, 87 (1994).
15. L. van Zee, J. J. Salzer, M. P. Haynes, *et al.*, Astron. J. **116**, 2805 (1998).
16. S. S. Larsen and T. Richtler, Astron. Astrophys. **345**, 59 (1999).
17. S. S. Larsen, Astron. Astrophys., Suppl. Ser. **139**, 393 (1999).
18. J. S. Young, L. Allen, J. D. P. Kenny, *et al.*, Astron. J. **112**, 1903 (1996).
19. W. Cui, W. T. Sanders, D. McCammon, *et al.*, Astrophys. J. **468**, 102 (1996).
20. R. Barbon, E. Cappellaro, and M. Turatto, Astron. Astrophys., Suppl. Ser. **81**, 421 (1989).
21. D. W. E. Green, IAU Circ. **7334**, 1 (1999).
22. I. I. Zin'kovskiĭ, S. S. Kaĭsin, A. I. Kopylov, *et al.*, *Technical Report of Special Astronomical Observatory, Russian Academy of Sciences,* 1994, No. 231.
23. S. R. Majewski, R. G. Kron, D. C. Koo, and M. A. Bershady, Publ. Astron. Soc. Pac. **106**, 1258 (1994).
24. P. Prugniel and P. Heraudeau, Astron. Astrophys., Suppl. Ser. **128**, 299 (1998).
25. R. Buta and K. L. Williams, Astron. J. **109**, 543 (1995).
26. M. Fioc and B. Rocca-Volmerange, Astron. Astrophys. (in press) (2001).
27. Yu. N. Efremov, *Sites of Star Formation in Galaxies* [in Russian] (Nauka, Moscow, 1989).

Translated by K. Maslennikov

Astronomy Reports, Vol. 46, No. 9, 2002, pp. 721–730. Translated from Astronomicheskiĭ Zhurnal, Vol. 79, No. 9, 2002, pp. 798–809.

Disk Boundaries in Spiral Galaxies

D. V. Bizyaev and A. V. Zasov

Sternberg Astronomical Institute, Universitetskiĭ pr. 13, Moscow, 119992 Russia

Received September 12, 2001; in final form, February 1, 2002

Abstract—We explore the hypothesis that the outer boundaries ("cutoffs") of the stellar disks observed in many galaxies are determined by the condition of local gravitational (Jeans) stability for the gaseous protodisks at large galactocentric distances. The ratio of the surface density of the disk $\Sigma_{\rm disk}$ to the critical value for Jeans instability $\Sigma_{\rm crit}$ is computed for a number of galaxies, assuming that the gas velocity dispersion in the forming disk corresponded to its current thickness and that the disk itself is in a quasi-equilibrium state. The mean estimated stellar velocity dispersion in the vicinity of the cutoff (12 km/s) is close to the typical velocity dispersions of gaseous clouds in disk galaxies. At greater distances, such velocity dispersions should ensure gravitational stability of the disk both at the present epoch and in the past. The cutoff radius of the disk $R_{\rm cut}$ is correlated with other disk parameters, and the ratio $\Sigma_{\rm disk}/\Sigma_{\rm crit}$ at $R_{\rm cut}$ is close to unity in most cases. We conclude that the available observational data agree well with the hypothesis that stellar disk cutoffs are due to a rapid decrease in the star-formation rate beyond $R_{\rm cut}$, where the gaseous disk has always been stable. © *2002 MAIK "Nauka/Interperiodica".*

1. INTRODUCTION

The azimuthally averaged brightnesses of the stellar disks in spiral galaxies decrease with galactocentric distance R, obeying in most cases an exponential law, $I(R) = I_0 \exp(-R/R_{\rm e})$, where $R_{\rm e}$ is the radial disk scale length. Analyses of the brightness profiles out to extremely faint isophotes suggest in many cases that the profile steepens abruptly at a some large distance, beyond which the radial scale length shortens significantly. We will call this distance the disk cutoff radius, $R_{\rm cut}$. The cutoff cannot be completely sharp, if only because of the radial velocity dispersion of the stars in the disk (10–20 km/s for regions near the disk periphery), which "smears out" the edges, so the notion of a cutoff is somewhat arbitrary, and the uncertainty in $R_{\rm cut}$ estimates can exceed 1–2 kpc.

The number of galaxies with observed cutoffs in their stellar disks is small due to technical difficulties in carrying out photometry at low intensity levels. Galaxies showing cutoffs are usually edge-on galaxies in which the brightness is enhanced by projection effects [1–7], although cutoffs are also observed in several galaxies seen almost face on [8]. The distance $R_{\rm cut}$ in units of the disk scale length $R_{\rm e}$ varies over a wide range, and lies in the interval 3–5 in most cases. The ratio $R_{\rm cut}/R_{\rm e}$ tends to increase toward larger galaxies [9].

The cutoff of the disk brightness profile by itself does not imply a total absence of gas and stars at large galactocentric distances. In a number of cases, rotating HI disks extend far beyond the optical boundary [10]. Isolated star-forming regions can sometimes be seen very far from the galactic centers (see, e.g., [11]).

The old stellar disk of our Galaxy also has a cutoff. According to the DIBRE infrared survey, $R_{\rm cut} = 12.4 \pm 0.1$ kpc [12]. However, observations reveal a small number of young stars and HII regions at even greater distances.

The origin of the cutoffs of stellar disks remains under debate. Current hypotheses can be divided into two groups. The first group attributes the existence of disk cutoffs to the conditions under which the disk formed in the pre-stellar stage, while the second group suggests they are due to conditions hindering star formation in the outer regions of already formed disks. One hypothesis in the first group is that sharp outer disk edges have resulted from the distribution of the initial angular momentum of the matter making up the disk: matter with a large specific angular momentum is simply absent [13]. Another possibility is that the process of disk formation has not completed, so that the outer parts of the disk have had time to form only out to some radius [1, 14–17]. The second group of hypotheses includes the suggestion that outer disk edges are due to a low gas pressure that prevents the development of thermal instabilities that are responsible for the formation of a two-phased interstellar medium [18], and the idea that the cutoffs are due to the stabilizing role of the rotation of the gaseous disk, which slows star formation in

1063-7729/02/4609-0721$22.00

the very tenuous outer regions by suppressing large-scale gravitational instability [3, 9].

The aim of the work presented here is to verify this last possibility.

The important role that can be played by gravitational instability of the initial gaseous disk during star formation in the disk is reflected by the close relationship between the degree of fulfillment of the stability condition by modern gaseous galactic disks and their star-formation rates [20–22]. In virtually all gas-rich galaxies, the star-formation rate (density of young stars) falls abruptly beginning with some radius R, where the density $\Sigma_{\rm gas}$ of the gaseous disk falls below some value that is close to the critical density for gravitational instability.

The main problem with testing this hypothesis is the absence of an exact analytical formula for marginal stability (stability criteria have been obtained only for simplified two-dimensional models). In addition, the solution of this problem requires data that are impossible to derive directly from observations, such as the surface density and velocity dispersion in the disk at $R_{\rm cut}$. Below, we make use of the fact that the vertical scale height (half-thickness) of the disk, which is a measurable quantity for edge-on galaxies, depends on the same parameters. We show below that, if combined with galactic rotation-curve data, photometric estimates of the vertical profile and radial disk scale length can be used to attack the problem in which we are interested.

2. SIMPLIFYING ASSUMPTIONS

Let us assume that the disk was entirely gaseous at time $T = 0$. The process of disk formation must be fairly prolonged, so that this initial epoch can be different for the outer and inner disk regions. We take this epoch to correspond to a region whose radius is close to $R_{\rm cut}$ for the disk.

Let us make several simplifying assumptions.

(1) The stellar disk formed from a gaseous protodisk that had already reached a quasi-equilibrium state. Otherwise, the very notion of the gravitational stability of the forming disk loses meaning, and the stellar population of the disk should form in accordance with a different scenario.

(2) The surface density of the disk at time $T = 0$ is the sum of the current surface densities of stars and gas. Note, however, that our subsequent conclusions remain unchanged if the process of the disk formation is accompanied by accretion and the disk remained in a quasi-stationary state.

(3) The velocity dispersion of stars perpendicular to the plane of the disk has not increased significantly since their formation. The stellar velocity dispersion in the Galaxy is known to increase with age; however, the mechanisms usually proposed to explain this increase (spiral-arm effects, gravitational interaction between stars and massive gas clouds) have low efficiencies at large R, especially beyond the region in which the spiral pattern is well defined. This assumption, however, is not fulfilled in interacting galaxies, which have systematically thicker disks [23].

We can adopt the following, more universal and softer, condition: the current stellar velocity dispersion perpendicular to the disk (along the Z axis) is an upper limit for the velocity dispersion of the parent gas of the old stellar disk population.

(4) The gaseous disk of the Galaxy is isothermal at time $T = 0$ (the velocity dispersion of gaseous clouds is isotropic), which is natural for collisional systems.

These assumptions will enable us to compare the estimated radial density distribution in the disk near $R_{\rm cut}$ with the critical density of the initial gaseous disk in the same region.

The surface density of the disk at a given radius can be determined in two ways. First, photometric disk profiles can be used as the input data by converting them into mass profiles via the mass-to-luminosity ratio M/L and adding the gas density at the same radius to the resulting stellar density. This approach has the drawback that the M/L ratio depends on a number of factors and is not known *a priori*. This ratio can, in principle, be estimated using evolutionary models of the stellar population and the observed color indices (under certain assumptions). However, the colors of the stellar populations of edge-on galaxies (which we consider below) are difficult to estimate due to the strong internal absorption. Moreover, the M/L ratios can display a large scatter even for stellar systems with the same color indices.

The second approach starts with the galactic rotation curve, and extracts the disk component from it. In this case, photometric data (first and foremost, the radial disk scale) can be used to reduce the ambiguity in the rotation-curve modeling. As a by product, we obtain simultaneously the desired surface density of stars and gas. We also determine the parameters of the spheroidal component of the galaxy required for estimating the equilibrium disk thickness.

The main sources of error in this method of surface-density estimation are as follows.

(a) The decomposition of the rotation curve does not allow unambiguous estimation of the relative mass of the disk even if the radial disk scale length is known.

(b) Observations of edge-on galaxies can yield significantly distorted rotation curves due to strong internal absorption when dust hides regions that are located along the major axis of the galaxy and

have maximum Doppler circular-velocity components (this applies primarily to optical rotation curves).

To allow for the ambiguity of parameter estimates for the disk and spherical components derived from rotation-curve decomposition, we analyzed three different models for each galaxy: a maximum disk model (the model with the maximum possible contribution of a disk with a specified radial scale length to the observed rotation curve), a "best fit" model (optimum agreement between the model and observed rotation curves, when the rms differences between the curves is minimum), and a minimum disk model. In the last case, the ratio $M_{\rm disk}/L$ takes on the minimum value that still allows the observed rotation curve to be explained in terms of a model with the adopted laws for the component density distributions but is no smaller than $0.5\,M_{\rm odot}/L_{\rm odot}$.

We compared the estimates of the disk density with the critical value (for gravitational stability) by estimating the latter from the kinematic parameters of the disk.

We will use the local stability criterion suggested by Polyachenko (see [24]), in which the dimensionless Toomre parameter for a marginally stable gaseous disk $Q_c = c_{\rm crit}/c_T$ is determined by the formula (here, $c_{\rm crit}$ is the critical velocity dispersion and $c_T = \pi G\,\Sigma_{\rm disk}(R)/\kappa(R)$ is the critical value for axisymmetric perturbations)

$$Q_c^2 = \frac{3}{2}\frac{\alpha^2 - 1}{\alpha^2 - 3/2}.$$

Here,

$$\alpha^2 = \frac{2\Omega}{R|\frac{d\Omega}{dr}|},$$

$\Sigma_{\rm disk}$ is the surface density of the gaseous disk, $\Omega(R)$ is the angular rotational velocity of the disk, and $\kappa(R)$ is the epicyclic frequency.

Like any other analytical criterion, this formula is an approximate relation. However, a similar criterion for a collisionless (stellar) disk derived by Polyachenko *et al.* [25] under the same assumptions is in good agreement with the results of numerical simulations of outer regions of the disk [26].

These relations enable us to write the formula for the critical surface density of the gaseous disk in the form

$$\Sigma_{\rm crit}(R) \approx 0.6\frac{c_g}{10\ {\rm km/s}} \times \frac{V(R)}{R}\sqrt{1+3x}\ \ \frac{M_\odot}{{\rm pc}^2}, \quad (1)$$

where V is the linear gas rotational velocity in km/s, R is the linear galactocentric distance in kpc, and $x = d\,\ln V/d\,\ln R$, c_g is the velocity dispersion of gaseous clouds in km/s [21].

In the case of a flat rotation curve with $x = 0$, the Toomre parameter is $Q = \sqrt{3}$, and $\Sigma_{\rm crit}$ is a factor of $\sqrt{3}$ lower than implied by the Toomre criterion $Q_c = 1$ (this is a result of allowing for non-axisymmetric perturbations, which are less stable in the disk than radial perturbations).

To determine the critical density, we must know the velocity dispersion of gaseous clouds at the time of formation of the stellar disk, which requires estimating the current velocity dispersion of old stars of the disk. No direct estimates are available at large galactocentric distances. However, for edge-on galaxies, the velocity dispersion can be estimated from the observed thickness of the stellar disks (under the above assumptions).

3. CRITICAL GAS DENSITY AT THE CUTOFF RADIUS

3.1. Estimate of the Relative Critical Density

A rough estimate of the critical density $\Sigma_{\rm crit}$ at a given radius is easy to derive if it is expressed in units of the central density Σ_0 of the exponential disk, without estimating the absolute mass or density of the disk.

We will assume that we know the linear radial scale length and vertical scale height of the density distribution in the disk (z_0 and $R_{\rm e}$, respectively) and that the rotation curve has a plateau at a velocity of $V_{\rm max}$.

Let $V_{\rm disk} = k \times V_{\rm max}$, where $V_{\rm disk}$ is the maximum rotational velocity for the rotation-curve component associated with the exponential disk [27]:

$$V_{\rm disk} = 0.623 \times \sqrt{2\pi G\,\Sigma_0\,R_{\rm e}}.$$

For spiral galaxies, the coefficient k is usually equal to 0.5–0.8, depending on the fractional mass of the halo [28, 29].

The vertical velocity dispersion of the disk stars is related to the vertical scale height z_0 and surface density $\Sigma(R)$ at a given radius via the formula

$$c_z^2 = z_0\pi G\Sigma$$

(here, we neglect the effect of the halo on the disk thickness). For a flat rotation curve, $\kappa = \sqrt{2}V_{\rm max}/R$, so that

$$\Sigma_{\rm crit}(R) = \frac{\sqrt{2}c_r V_{\rm max}/R}{Q_T\pi G},$$

where $Q_T \approx \sqrt{3}$, in accordance with the adopted criterion (1). Combining the last three equations, we obtain for the desired ratio with $k \approx 0.7$:

$$\frac{\Sigma_{\rm crit}}{\Sigma_0} \approx \frac{0.9\sqrt{\exp(-R_{\rm cut}/R_{\rm e}) \times (z_0/R_{\rm cut})}}{(R_{\rm cut}/R_{\rm e})}. \quad (2)$$

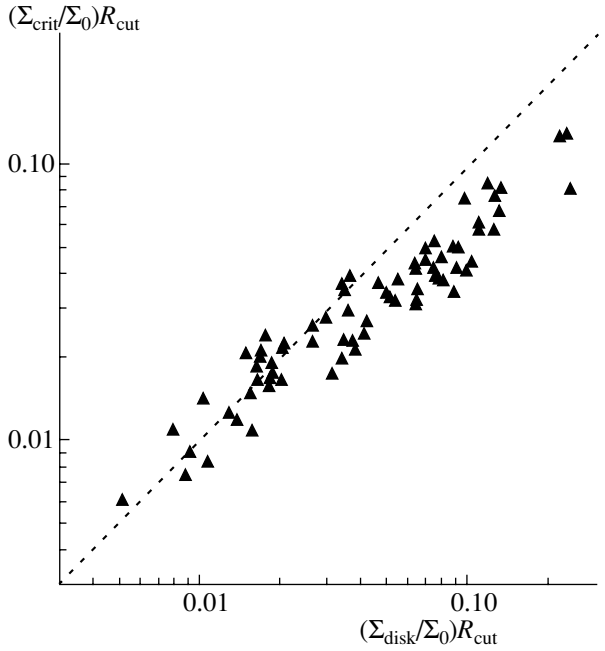

Fig. 1. Comparison of Σ_{disk}/Σ_0 and Σ_{crit}/Σ_0 at the disk cutoff radius estimated from Eqs. (2) and (3) for a sample of 75 objects.

On the other hand, the relative surface density of the disk at the cutoff radius R_{cut} can be written in the form

$$\frac{\Sigma_{disk}}{\Sigma_0} = \exp(-R_{cut}/R_e). \qquad (3)$$

The Σ_{crit}/Σ_0 and Σ_{disk}/Σ_0 ratios can be estimated using Eqs. (2) and (3) and the photometrically determined value of R_e, assuming that the radial distribution of the surface density is proportional to the surface brightness. Figure 1 compares the Σ_{disk}/Σ_0 and Σ_{crit}/Σ_0 ratios estimated from (2) and (3) for a sample of 75 galaxies from [1–3, 7, 30] for which we adopted the photometrically determined R_{cut}, z_0, and R_e values. We determined the vertical scale heights z_0 for an isothermal law for the decrease of the volume luminosity of the disk with distance from the galactic plane: $\rho_L(z) \sim \mathrm{sech}^2(z/z_0)$. The dashed line in Fig. 1 corresponds to $\Sigma_{disk}/\Sigma_0 = \Sigma_{crit}/\Sigma_0$ at $R = R_{cut}$.

It follows from Fig. 1 that the normalized Σ_{crit} and Σ_{disk} estimates at R_{cut} are closely correlated and follow a linear relationship with a slope that is close to unity. Note that the very existence of such a tight relation in Fig. 1 agrees well with the possibility that R_{cut} is related to the disk stability threshold but by no means proves this hypothesis, since the quantities plotted are interdependent due to the way they were estimated (both quantities contain the factor $\exp(-R_{cut}/R_e)$, though in different powers).

If we substitute in (2) the observed z_0/R_{cut} ratios for random quantities uniformly distributed over the same interval, there remains some overall dependence, but the dispersion of the data points on the diagram increases by a factor of two to three. The correlation coefficient remains high (0.7), even if we eliminate the interrelation between the quantities being compared by dividing (2) and (3) by $\exp(-R_{cut}/2R_e)$.

It is clear from Fig. 1 that the data points deviate systematically from the linear relation at large values of $\Sigma_{disk}/\Sigma_0 > 0.05$ (or at $R_{cut}/R_e < 3$). The integrated parameters of galaxies with large $\Sigma_{disk}/\Sigma_0(R_{cut})$ (cutoff radius, vertical disk scale height, central disk surface brightness, width of the HI line, absolute magnitude) do not differ from the corresponding mean parameters for the main sample. The only exception is the radial scale length R_e, whose mean value is substantially higher for galaxies located in the upper part of the diagram, which deviate from the linear relation. For example, for 64 objects with $\Sigma_{disk}/\Sigma_0 < 0.1$, the mean R_e and its dispersion are 5.7 ± 2.8 kpc, these values for 11 objects with $0.1 < \Sigma_{disk}/\Sigma_0$ are 10.1 ± 5.1 kpc (seven of 11 objects have radial scale lengths greater than 8 kpc), and the mean R_e for the three galaxies with the largest $\Sigma_{disk}/\Sigma_0 > 0.2$ is 15.4 kpc. As a result, the R_{cut}/R_e and z_0/R_e ratios for these objects are, on average, smaller than for galaxies with low Σ_{disk}/Σ_0.

This appears to be why galaxies with large R_{cut}/R_e values deviate from the linear relation. Indeed, the contribution of a fixed-mass disk to the total galactic potential is smaller for objects with large radial disk scale lengths (the maximum circular velocity for an exponential disk of given mass is proportional to $R_e^{-0.5}$), whereas we assumed that the disk's contribution to the rotation curve is the same for all galaxies. The Σ_{crit} and Σ_{disk} values for galaxies with the largest R_e can be reconciled if the maximum rotation velocity of the disk component of the rotation curve, V_{disk}, is equal to 0.4–0.5 instead of our adopted value of 0.7; i.e., if we suppose that the galaxies in question have most of their mass in the spherical component (halo) even at the radius ($\approx 2R_e$) where the disk's contribution to the rotation curve is maximum.

Therefore, V_{max} and, consequently, Σ_{crit}/Σ_0 should be larger for galaxies with more extended scale lengths R_e, if their other parameters are equal. We obtain a refined quantitative estimate of the difference in R_e in the next section, where we estimate Σ_{crit} using a more rigorous approach.

3.2. Estimates of the Absolute Value of the Critical Disk Density

We now estimate the critical density of galactic disks using the parameters of components that can be

derived by decomposing the rotation curve in terms of a three-component model (a disk of fixed thickness, spherical bulge, and spherical halo).

We used two samples of edge-on galaxies. The first sample, adopted from van der Kruit and Searle [1–3], includes seven relatively nearby and large edge-on galaxies with conspicuous disk cutoffs in their photometric profiles. The second sample consists of nine galaxies studied by Pohlen *et al.* [7] using photometric CCD data for which R-band photometry and published rotation curves are available. As for the photometric data, we use the radial scale lengths and vertical scale heights reported in these papers. The table gives the adopted distance, radial photometric disk scale length (for $R < R_{\rm cut}$), vertical disk scale height z_0, and cutoff radius $R_{\rm cut}$ for each galaxy, together with the references for the adopted rotation curves.

We decomposed the rotation curves into disk, bulge, and halo components assuming fixed radial scale lengths and vertical scale heights for the galaxy disks. We fitted the halo using a very simple model with a quasi-isothermal distribution of the volume density in the form

$$\rho_{\rm halo}(R) = \frac{\rho_{\rm halo}(0)}{1 + (R/a_h)^2}.$$

We fitted the bulge density distribution using a King law.

To go from the observed disk scale heights z_0 to the vertical velocity dispersion c_z, we must know, not only the disk densities, but also the masses of the spherical components at the radius considered. The vertical profile of the volume density of an equilibrium disk immersed in a spherically symmetric external potential is given by the equation [39]:

$$y\frac{d^2y}{dx^2} - \left(\frac{dy}{dx}\right)^2 = -2y^3 - 2y^2\frac{\rho^{\rm eff}_{\rm halo}(0)}{\rho(0)}, \quad (4)$$

where $y = \rho(z)$ is the disk density as a function of the distance z from the galactic plane, $\rho(0)$ is the disk density in the $z = 0$ plane, $x = z/z_0$, and $\rho^{\rm eff}_{\rm halo}(0)$ is the effective halo density in the plane of the disk (see below). In the general case, the vertical disk scale height is given by

$$z_0 = \frac{< c_z^2 >}{\pi G \Sigma_{\rm disk}},$$

however, in the presence of a halo, the $\rho(z)$ distribution has a more complex form than the usual $\mathrm{sech}^2(z/z_0)$ law. The volume density is related to the surface density via the equation $\Sigma_{\rm disk}(R) = \int \rho(R,z)dz$. The effective halo density that enters (4) can be expressed in terms of the halo density, and the form of the rotation curve can be expressed using the formula

$$\rho^{\rm eff}_{\rm halo}(R) = \rho_{\rm halo}(R) - (4\pi GR)^{-1}\frac{dV^2(R)}{dR}.$$

Using the photometric scale lengths $R_{\rm e}$ and estimating the disk density Σ_0 and the parameters of the bulge and dark halo by decomposing the rotation curve, we find it is possible to determine the parameter $\rho(z)$ as a function of c_z by solving (4). In our case, we solve the inverse problem: we use (4) to determine the vertical disk profile for various c_z, and select the value that yields a vertical scale height coincident with the observed value. The parameter c_z thus obtained can be used to estimate the critical density $\Sigma_{\rm crit}$ via formula (1).

The effect of the halo on the vertical disk scale height is relatively small (we solved (4) precisely to take this effect into account): for a given c_z, the halo reduces z_0 by 10–20% compared to a "pure" disk

Table

Galaxy	D, Mpc	$R_{\rm e}$, kpc	z_0, kpc	$R_{\rm cut}$, kpc	Reference for $V(R)$
First sample, based on [1, 2, 3]					
NGC 4244	5.0	2.6	0.58	13.7	[31]
NGC 5907	11.0	5.7	0.83	19.3	[32]
NGC 4565	10.0	5.5	0.79	24.9	[32]
NGC 891	9.5	4.9	0.99	21.0	[33]
NGC 5023	8.0	2.0	0.46	7.8	[34]
NGC 4217	14.5	3.5	1.70	14.3	[35]
NGC 4013	11.8	3.4	1.08	14.0	[36]
Second sample, based on [7]					
ESO 187-008	56.3	4.12	1.20	13.7	[37]
ESO 269-015	42.5	8.33	1.63	18.6	[37]
NGC 2424	43.1	6.62	2.49	23.4	[38]
ESO 319-026	45.3	3.23	0.70	13.8	[37]
ESO 321-010	39.5	4.14	0.96	12.4	[37]
ESO 446-018	62.2	7.14	1.18	22.8	[37]
ESO 446-044	35.2	5.08	0.99	12.9	[37]
ESO 528-017	80.7	7.79	1.06	21.6	[37]
ESO 581-006	40.9	3.61	1.11	11.1	[37]

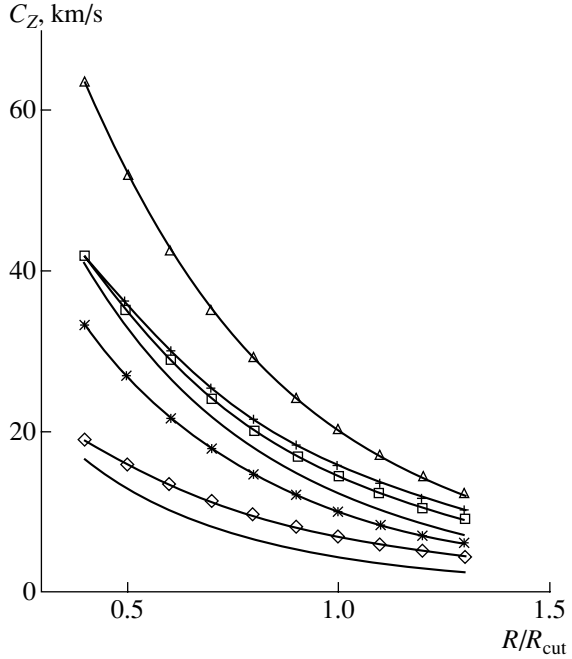

Fig. 2. Radial dependence of the vertical component of the stellar velocity dispersion c_z for the seven galaxies of the first sample computed using the best-fit model. The distance is normalized to the disk cutoff radius R_{cut}. The solid lines without symbols correspond to NGC 4244 (below) and NGC 891 (above), the crosses to NGC 5907, the asterisks to NGC 4565, the diamonds to NGC 5023, the triangles to NGC 4217, and the squares to NGC 4013.

estimate ($\rho^{eff}_{halo} = 0$). The presence of a massive halo can indeed affect the thickness of the disk if the disk is close to marginal stability; however, this is achieved via a different mechanism [40]: since the mass of the disk is fixed, its angular velocity increases with the mass of the surrounding halo. Therefore, the condition of gravitational stability in the presence of a massive halo requires a lower velocity dispersion and, consequently, allows a thinner disk.

Morozov [41] was the first to point out that the disk velocity dispersion (relative to its rotational velocity) is correlated with the halo mass fraction. This relation is confirmed by both numerical models of equilibrium disks and measurements of vertical scale heights of edge-on disks (see [26, 29] and references therein).

The uncertainty in Σ_{crit} is due mainly to the uncertainty in the estimate of Σ_{disk} near R_{cut} derived from the rotation curve. To determine the interval of possible values of Σ_{crit}, we estimated the parameters of the galaxy components separately for the best-fit, maximum-disk, and minimum-disk models (see Section 2).

Figure 2 shows the radial dependences of c_z computed for the seven galaxies of the first sample using the best-fit model. If, in accordance with the above assumptions, we consider the current c_z for the stellar disk to be an upper limit for the one-dimensional velocity dispersion (speed of sound) during the disk's formation at the onset of star formation in the region of $R \le R_{cut}$, the corresponding Σ_{crit} should be an upper limit for the critical surface density of gas and $\Sigma_{disk}/\Sigma_{crit}$ should represent a lower limit for the gas-to-critical density ratio at time $T = 0$. It is evident from Fig. 2 that the mean c_z for regions near R_{cut} is about 12 km/s. This value is close to the current vertical velocity dispersion of gas in disks with ongoing star formation (see, e.g., the c_z estimates for face-on galaxies reported by Lewis [42] and Kamphuis and Sancisi [43]), leaving no reason to believe that c_z was significantly lower in the past.

Figure 3 shows the radial distributions of the $\Sigma_{disk}/\Sigma_{crit}(R)$ values corresponding to the $c_z(R)$ dependences in Fig. 2. First, they show that $\Sigma_{disk}/\Sigma_{crit}$ decreases with increasing radius in all galaxies. Second, at $R \approx R_{cut}$, the mean $\Sigma_{disk}/\Sigma_{crit}$ is close to unity (0.8–1.7, with a mean value of 1.22). A comparison of the different models (maximum disk, best fit, and minimum disk) shows that the possible values for this ratio for a particular galaxy are confined to an interval whose width is about 30% of the mean ratio. Note also that $\Sigma_{disk}/\Sigma_{crit}$ depends linearly on the adopted distance to the galaxy, and is thus also affected by the uncertainty of this distance.

However, it is evident from Fig. 3 that the $\Sigma_{disk}/\Sigma_{crit}(R_{cut})$ values exhibit a small scatter, which is comparable to the scatter of the current gas-to-critical density ratios for the gaseous disks of spiral galaxies at the radius R_{HII} beyond which the star-formation rate decreases sharply [20, 22].

The bold line in Fig. 3 shows the radial variation of $\Sigma_{disk}/\Sigma_{crit}$ for our Galaxy based on the directly estimated value $c_z = 20$ km/s in the solar neighborhood [44, 45]. We took the radial disk scale and cutoff radius to be 3 and 14 kpc, respectively (in accordance with [12]). We assumed that the rotation curve is flat in the region considered and that the disk thickness is constant. As is evident from Fig. 3, this relation has the same form for the Milky Way as for other galaxies.

Figure 4a shows the dependence between Σ_{disk} and Σ_{crit} at $R = R_{cut}$ for the galaxies of the first sample and for our own Galaxy (indicated by a cross). This relation is characterized by a formally large correlation coefficient (0.85) and a slope that is close to unity. The approximate equality of Σ_{disk} and Σ_{crit} virtually disappears if we adopt the same stellar velocity dispersion at $R = R_{cut}$ for all the galaxies (see Fig. 4b, where the velocity dispersion is taken to be equal to 10 km/s).

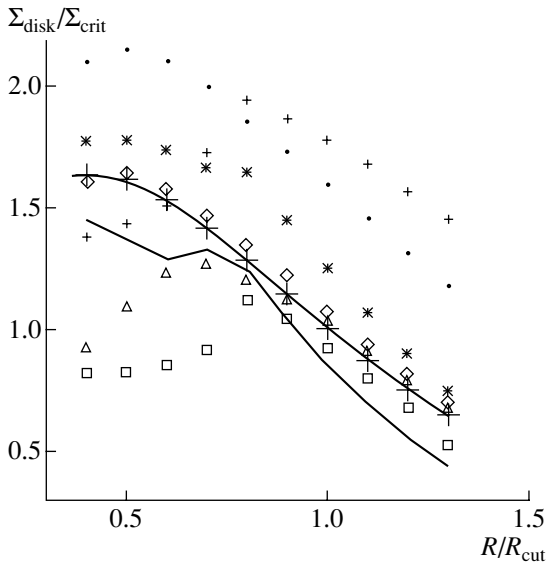

Fig. 3. Radial dependences of $\Sigma_{disk}/\Sigma_{crit}$ constructed for the "best-fit" model for the seven galaxies of the first sample. The distance is normalized to the disk cutoff radius R_{cut}. The solid line without symbols corresponds to NGC 4244, the dots to NGC 891, the small crosses to NGC 5907, the asterisks to NGC 4565, the diamonds to NGC 5023, the triangles to NGC 4217, and the squares to NGC 4013. The bold line with large crosses corresponds to our own Galaxy.

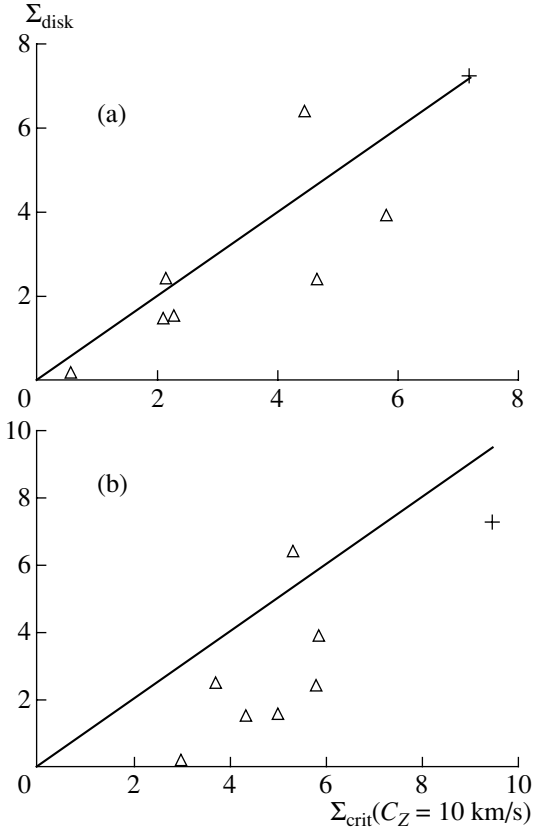

Fig. 4. (a) Σ_{disk} vs. Σ_{crit} relation at $R = R_{cut}$ for galaxies of the first sample and for our own Galaxy (cross). (b) The same plot constructed assuming that all galaxies have the same velocity dispersion at $R = R_{cut}$, equal to 10 km/s.

In contrast to the Σ_{disk} / Σ_{crit} ratio, individual values of Σ_{disk} are not concentrated near any certain value, as is also true of the disk surface brightness at R_{cut} reduced to the face-on position. This result supports the hypothesis that the densities Σ_{disk} and Σ_{crit} are indeed physically correlated at the cutoff radius.

Dependencies analogous to that in Fig. 3 but constructed for the maximum-disk and minimum-disk models have qualitatively the same form. Naturally, assuming a more massive disk implies even higher $\Sigma_{disk}/\Sigma_{crit}$ ratios.

To expand our sample, we also constructed the radial dependences of $\Sigma_{disk}/\Sigma_{crit}$ for nine galaxies from [7] (our second sample), for which we were able to find rotation curves in the literature suitable for decomposition into components (Table). The galaxies of this group are located at greater distances (from 35 to 81 Mpc for $H_0 = 75$ km s^{-1}Mpc^{-1}) than those of the first sample.

The radial dependences of $\Sigma_{disk}/\Sigma_{crit}$ for these galaxies are shown in Fig. 5 in the same way as were those of the first sample. The larger scatter of these curves compared to those in Fig. 3 is partly due to the larger uncertainties in the photometric parameters used, due to the poorer angular resolution for the corresponding data.

Figure 6 summarizes the results of comparing Σ_{disk} and Σ_{crit} at the cutoff radius for all the galaxies considered. Due to the uncertainty in the cutoff radius associated with the choice of model used for the rotation-curve decomposition, we give an interval of $\Sigma_{disk}/\Sigma_{crit}$ for the three rotation-curve models used for each galaxy of the two samples (Fig. 6). The left and right boundaries of the interval correspond to the minimum- and maximum-disk models, respectively. The filled triangles indicate the best-fit model values. The vertical line corresponds to $\Sigma_{disk}/\Sigma_{crit} = 1$. As is evident from the figure, given the errors, the hypothesis that $\Sigma_{disk}/\Sigma_{crit}$ is equal to unity at R_{cut} is generally in good agreement with the available data, with only a few exceptions. For NGC 891, NGC 4565, and ESO 528-017, the $\Sigma_{disk}/\Sigma_{crit}$ value at R_{cut} remains greater than unity even when it is computed using the minimum-disk model; the mass-to-luminosity ratios are $M_{disk}/L_J = 4.3$ and 4.6 for the first two galaxies (the J photometric system used in [1–3] is close to the B band) and $M_{disk}/L_R = 0.97$ for the third galaxy. For ESO 581-006, on the contrary, even the maximum-disk model yields $\Sigma_{disk}/\Sigma_{crit} \approx 0.7$ at

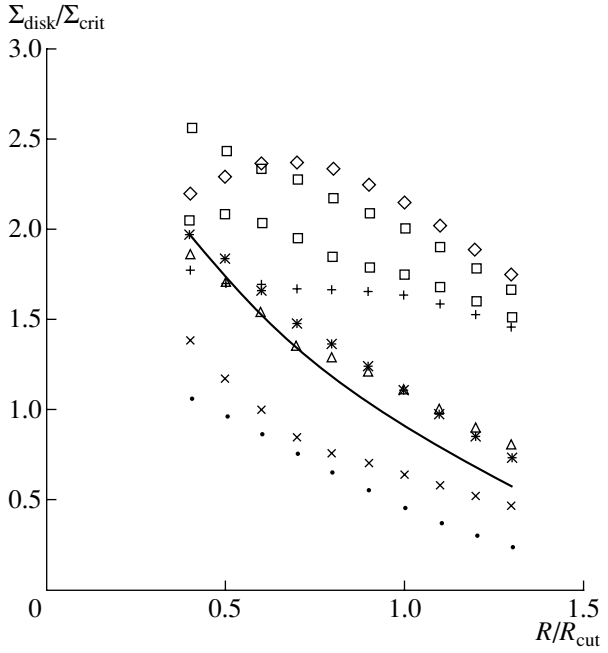

Fig. 5. Same as Fig. 3 for the nine galaxies of the second sample (see text). The solid line corresponds to ESO 187-008, the pluses to ESO 269-015, the asterisks to NGC 2424, the dots to ESO 319-026, the diamonds to ESO 321-010, the triangles to ESO 446-018, the squares to ESO 446-044 (lower curve) and ESO 528-017 (upper curve), and the crosses to ESO 581-006.

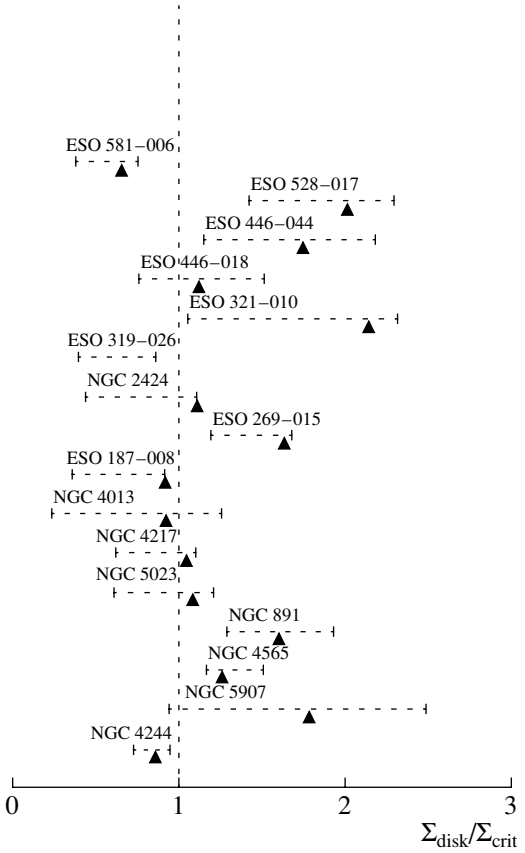

Fig. 6. Interval of $\Sigma_{disk}/\Sigma_{crit}$ obtained using the three adopted rotation-curve models for both galaxy samples. For each galaxy, the left and right ends of the interval correspond to the minimum- and maximum-disk models, respectively. The filled triangles correspond to the best-fit model. The vertical line indicates $\Sigma_{disk}/\Sigma_{crit} = 1$.

$R = R_{cut}$. These galaxies may have undergone a more complex formation scenario in their outer regions.

The mean $\Sigma_{disk}/\Sigma_{crit}$ values at R_{cut} for the first sample are 1.22 ± 0.13, 1.49 ± 0.21, and 0.80 ± 0.14 for the best-fit, maximum-disk, and minimum-disk models, respectively. The corresponding values for the galaxies of the second sample are 1.31 ± 0.20, 1.44 ± 0.23, and 0.8 ± 0.14.

4. DISCUSSION AND CONCLUSIONS

The key assumptions underlying this paper are that the current stellar z-velocity dispersion at the disk periphery is equal to or greater than the velocity dispersion (speed of sound) in the gaseous disk when the bulk of stars formed, and that this velocity dispersion can be determined from the condition of local gravitational stability for the disk. In this, it is also assumed that the transformation of the gaseous disk into a stellar disk involved no substantial increase of c_z. Let us consider this assumption in more detail.

The stellar disk that formed from the equilibrium gaseous disk must reach a stable state within a short time. However, gaseous and stellar disks are governed by different gravitational stability conditions. In the case of axisymmetric perturbations, these differences are minimal (the coefficient π in the equation for the critical velocity dispersion is replaced by 3.36 [46]). In the presence of non-axisymmetric perturbations, a stellar disk requires a higher radial velocity dispersion to maintain its stability (according to [25], the difference is a factor of $\sqrt{3}$ for a flat rotation curve). However, the vertical velocity dispersion c_z changes little in this case, since higher c_r values are accompanied by the development of anisotropy in the velocity distribution in the stellar disk: $c_z/c_r < 1$. Indeed, both observations [47, 48] and the results of dynamical modeling (see the discussion of this issue in [26]) show that c_z/c_r values in stellar disks are 0.5–0.7, whereas $c_z \approx c_r$ for collisional gaseous disks. Therefore, it is mainly the radial and not the vertical velocity dispersion that increases in the transition to a collisionless disk. Therefore, the assumption that the observed thickness of a stellar disk reflects the initial velocity dispersion in the gaseous disk seems to be quite justified. However, we should bear in mind that

estimates of the critical velocity dispersions remain fairly crude, and the development of a disk-formation model should include a separate analysis of the dynamical evolution of galactic disks in the transition from a gaseous to a stellar state.

The results presented here confirm that gravitational instability is a crucial factor determining the efficiency of star formation (the star-formation rate per unit gas mass), at least in the outer regions of galactic disks—and not only at the present epoch, but also during the formation of galaxies. However, observations of relatively nearby galaxies show that stars are still born in places where the observed gas density is below the critical threshold, albeit at lower rates (e.g., in M33 [22]; see also a discussion of this issue in [21]), since the development of gravitational instability in gaseous disks is an efficient but by no means the only mechanism capable of supporting star formation. Therefore, faint extensions of stellar disks may exist even at $R > R_{\rm cut}$.

Apart from gravitational instability, other factors that can significantly enhance the star-formation efficiency during the formation of disk stars include the tidal influence of neighboring galaxies; self-sustained star formation, when the influence of massive stars on the ambient medium triggers the formation of stars in neighboring regions; and gas compression waves associated with spiral arms. This last mechanism is at present inefficient at the radii considered, but billions of years ago, when the outer regions of the galaxy consisted mostly of gas, powerful spiral waves (due to the gravitation of gas rather than of stars) could have been much more extensive. However, whatever additional star-formation triggering mechanisms there might be, they should not only disrupt the relation between $R_{\rm cut}$ and $\Sigma_{\rm disk}/\Sigma_{\rm crit}$, but also decrease the total gas content preserved to the prsent epoch. This may explain why disk cutoffs are more difficult to detect in early-type disk galaxies [49] characterized by low gas mass fractions. However, the results presented here show that gravitational instability of rotating disks was nevertheless the determining factor during the formation of these stellar systems.

Note that, if the radial dependence of the critical density in the galaxy disk does not change with time, the location of $R_{\rm cut}$ relative to the center of the galaxy should be independent of the disk-formation scenario: whether the disk formed instantaneously or as a result of a prolonged infall of gas (provided that the gaseous disk remained in a quasi-equilibrium state).

The mean stellar velocity dispersion at $R_{\rm cut}$ estimated from the current thicknesses of stellar disks is 12 km/s for the galaxies considered here. This value is close to the estimated velocity dispersions of gaseous clouds in galaxies with ongoing star formation, suggesting that the formation of the disk was not followed by any substantial heating in the vertical direction at $R = R_{\rm cut}$. The closeness of c_z to the critical value indicates that, in most of the galaxies, the outer regions of their stellar disks do not have any substantial margin of gravitational stability.

Our results show that the ratio $\Sigma_{\rm disk}/\Sigma_{\rm crit}$ for a disk whose thickness does not change with radius decreases from the center to the periphery in all the galaxies considered. $\Sigma_{\rm disk}/\Sigma_{\rm crit}$ is close to unity in the cutoff region (the scatter is within the uncertainty due to the choice of the disk mass fraction in the decomposition of the observed rotation curve). This supports the hypothesis that, in most of the galaxies studied, both the stellar velocity dispersion and the total mass of matter (stars + gas) in the outer disk have remained largely unchanged since the time of formation of the disk.

Thus, the observational data agree well with the hypothesis that the observed outer boundaries of stellar disks, beyond which there is a rapid brightness decrease (at least for the late-type galaxies studied here), are the result of the gravitational stability of the gaseous protodisks at $R > R_{\rm cut}$, which has kept the efficiency of star formation low at large distances from the galactic center.

ACKNOWLEDGMENTS

This work was supported by the Russian Foundation for Basic Research (project no. 01-02-17597) and the "Astronomy" State Research and Technology Program.

REFERENCES

1. P. C. van der Kuit and L. Searle, Astron. Astrophys. **95**, 105 (1981).
2. P. C. van der Kuit and L. Searle, Astron. Astrophys. **95**, 116 (1981).
3. P. C. van der Kuit and L. Searle, Astron. Astrophys. **110**, 61 (1981).
4. P. C. van der Kuit and L. Searle, Astron. Astrophys. **110**, 79 (1981).
5. R. de Grijs, Ph.D. Thesis (University of Groningen, 1997).
6. A. Barteldrees and R.-J. Dettmar, Astron. Astrophys., Suppl. Ser. **103**, 475 (1994).
7. M. Pohlen, R.-J. Dettmar, R. Lutticke, and U. Schwarzkopf, Astron. Astrophys., Suppl. Ser. **144**, 405 (2000).
8. P. C. van der Kruit, Astron. Astrophys. **192**, 117 (1998).
9. M. Pohlen, R.-J. Dettmar, and R. Lutticke, Astron. Astrophys. **357**, L1 (2000).
10. P. C. van der Kruit, in *Galaxy Disks and Disk Galaxies,* Ed. by J. Funes and E. Corsini, Astron. Soc. Pac. Conf. Ser. **230**, 119 (2001).

11. A. M. Ferguson, R. F. G. Wyse, J. S. Gallagher, and D. Hunter, Astrophys. J. **506**, L19 (1998).
12. H. T. Freudenreich, Astrophys. J. **492**, 495 (1998).
13. P. C. van der Kruit, Astron. Astrophys. **173**, 59 (1987).
14. P. Seiden, L. Schulman, and B. Elmegreen, Astrophys. J. **282**, 95 (1984).
15. D. Lin and J. Pringle, Mon. Not. R. Astron. Soc. **225**, 607 (1987).
16. B. Zhang and R. Wyse, Mon. Not. R. Astron. Soc. **313**, 310 (2000).
17. A. Ferguson and C. Clarke, Mon. Not. R. Astron. Soc. **325**, 781 (2001).
18. B. G. Elmegreen and A. Paravano, Astrophys. J. **435**, L121 (1994).
19. S. M. Fall and G. Efstathiou, Mon. Not. R. Astron. Soc. **193**, 189 (1980).
20. R. Kennicutt, Astrophys. J. **344**, 685 (1989).
21. A. Zasov and D. Bizyaev, Pis'ma Astron. Zh. **22**, 83 (1996) [Astron. Lett. **22**, 71 (1996)].
22. C. Martin and R. Kennicutt, Astrophys. J. **555**, 301 (2001).
23. V. Reshetnikov and F. Combes, Astron. Astrophys. **324**, 80 (1997).
24. V. Polyachenko, E. Polyachenko, and A. Strel'nikov, Pis'ma Astron. Zh. **23**, 551 (1997) [Astron. Lett. **23**, 483 (1997)].
25. V. Polyachenko, E. Polyachenko, and A. Strel'nikov, Pis'ma Astron. Zh. **23**, 598 (1997) [Astron. Lett. **23**, 525 (1997)].
26. A. Khoperskov, A. Zasov, N. Tyurina, and E. Chulanova, Astron. Zh. (in press) [Astron. Rep. (in press)].
27. K. Freeman, Astrophys. J. **160**, 811 (1970).
28. R. Bottema, Astron. Astrophys. **328**, 517 (1997).
29. A. Khoperskov, A. Zasov, and N. Tyurina, Astron. Zh. **78**, 213 (2001) [Astron. Rep. **45**, 180 (2001)].
30. U. Schwarzkopf and R.-J. Dettmar, Astron. Astrophys. **361**, 451 (2000).
31. M. Honma and Y. Sofue, Publ. Astron. Soc. Jpn. **49**, 539 (1997).
32. Y. Sofue, Astrophys. J. **458**, 120 (1996).
33. Y. Sofue and N. Nakai, Publ. Astron. Soc. Jpn. **45**, 139 (1993).
34. R. Bottema, G. Shostak, and P. van der Kruit, Astron. Astrophys. **167**, 34 (1986).
35. R. Sanders and M. Verheijen, Astrophys. J. **503**, 97 (1998).
36. R. Bottema, Astron. Astrophys. **306**, 345 (1996).
37. M. Persic and P. Salucci, Astrophys. J., Suppl. Ser. **99**, 501 (1995).
38. I. Karachentsev, Pis'ma Astron. Zh. **17**, 485 (1991) [Sov. Astron. Lett. **17**, 206 (1991)].
39. J. Bahcall, Astrophys. J. **276**, 156 (1984).
40. A. Zasov, D. Makarov, and E. Mikhaĭlova, Pis'ma Astron. Zh. **17**, 884 (1991) [Sov. Astron. Lett. **17**, 374 (1991)].
41. A. G. Morozov, Pis'ma Astron. Zh. **9**, 716 (1983) [Sov. Astron. Lett. **9**, 370 (1983)].
42. B. Lewis, Astrophys. J. **285**, 453 (1984).
43. J. Kamphuis and R. Sancisi, Astron. Astrophys. **273**, L31 (1993).
44. P. D. Sackett, Astrophys. J. **483**, 103 (1997).
45. V. P. Reshetnikov, Astrofizika **43**, 197 (2000)
46. A. Toomre, Astrophys. J. **139**, 121 (1964).
47. R. Bottema, Astron. Astrophys. **275**, 16 (1993).
48. J. Gerssen, K. Kuijken, and M. Merrifield, Mon. Not. R. Astron. Soc. **288**, 618 (1997).
49. P. C. van der Kruit, Astron. Astrophys. **192**, 117 (1988).

Translated by A. Dambis

Astronomy Reports, Vol. 46, No. 9, 2002, pp. 731–739. Translated from Astronomicheskiĭ Zhurnal, Vol. 79, No. 9, 2002, pp. 810–819.

The Outer Turbulence Scale in the Interstellar Plasma

V. I. Shishov and T. V. Smirnova

Pushchino Radio Astronomy Observatory, Pushchino, Russia

Received March 29, 2001; in final form, February 1, 2002

Abstract—The structure function for phase fluctuations on spatial scales from 10^6 to 10^{17} m is constructed using data on diffractive and refractive scintillation of pulsars, scattering angles, variations in pulse arrival times, and differences in dispersion measures observed for close pairs of pulsars in globular clusters. For distances $R > 1$ kpc (a sample of pulsars with DM ≥ 30 pc/cm^3), the fluctuations in the interstellar electron density on scales from 10^6 to 10^{14} m are well described by a Kolmogorov spectrum with index 11/3. Analysis of variations in the dispersion measures for close pairs of pulsars in globular clusters indicates an outer turbulence scale of $L_0 = 10^{15}$ m. The relative level of turbulent fluctuations is determined for the interstellar plasma, and the important role of turbulence in the energy balance is demonstrated.

1. INTRODUCTION

In spite of many-year studies of interstellar scintillations of radio sources and other radio-wave modulations by the turbulent interstellar plasma, there is no generally accepted model for the turbulence giving rise to these effects. The construction of such a model requires some additional observational data. In particular, we must detect the outer turbulence scale L_0 and estimate the level of the turbulence, i.e., the square of the ratio of the variance of the electron-density fluctuations to the average density: $\delta = (\Delta N_e/N_e)^2$. These parameters are extremely important for the identification of sources of the turbulent energy. A composite three-dimensional spectrum of the electron-density fluctuations on scales from a thousand kilometers to several parsecs was constructed in [1] based on measurements of various radio-wave modulation effects introduced by the interstellar plasma, derived from observations of pulsars located nearby the Sun ($R < 1$ kpc). These data indicate a power-law spectrum for this range of scales, with the power-law index of the three-dimensional spectra being close to that of a Kolmogorov spectrum. However, the accuracy of the spectrum presented in [1] is rather low, especially for the larger scales. Differences in the plasma parameters in different regions of the Galaxy must be taken into account when constructing composite spectra. The existence of differences between the parameters of the turbulent plasma in clouds in the spiral arms of the Galaxy and in the inter-arm space was pointed out in [2, 3]. It was shown in [4] that there are clouds of turbulent plasma with two types of spectra in the spiral arms: a pure power-law Kolmogorov spectrum and a spectrum with an inner scale. In addition, the medium is considerably inhomogeneous at distances $R > 1$ kpc. Consequently, when constructing composite spectra, the observational data must be reduced to a single set of physical conditions.

Here, we construct a composite phase-fluctuation structure function derived from temporal variations in the dispersion measures obtained from pulsar timing measurements, measurements of diffractive and refractive scintillation of pulsars, and variations in the dispersion measures of pairs of pulsars in globular clusters; this enables us to estimate the structure function for the largest scales. We have paid special attention to applying reliable corrections to reduce the observational data to the same physical conditions. Further, we determine the turbulence spectrum based on the behavior of the structure function. We prefer to work with the phase-fluctuation structure function, since, in contrast to the electron-density fluctuation spectrum, it is directly measurable for all the observations used (except for those of refractive scintillations).

2. BASIC RELATIONS

The main quantity characterizing the interstellar medium is the dispersion measure

$$\mathrm{DM}[\mathrm{pc/cm^3}] = \int_0^R dr N_e, \qquad (1)$$

where R is the distance in parsecs from the source to the observer and N_e is the electron number density in cm^{-3}; DM can be well measured from pulsar observations. The time delay of the arrival of a pulsar pulse

introduced by the interstellar medium depends on the dispersion measure, and obeys the relation

$$\begin{aligned}\delta t &= (1/\alpha_d)(f_0/f)^2\mathrm{DM},\\ f_0 &= 1000\ \mathrm{MHz},\\ \alpha_d &= 241.03\ \mathrm{pc\ cm^{-3}\ s^{-1}}.\end{aligned} \tag{2}$$

We have introduced the frequency f_0 since the most reliable data on refractive scintillations are available near 1000 MHz, and it is convenient to reduce other data to this frequency. An additional phase fluctuation introduced by the interstellar medium (calculated in a linear geometrical-optics approximation) also depends on the dispersion measure:

$$S = (\lambda r_e)\int_0^R drN_e = \alpha_s(f_0/f)\mathrm{DM}, \tag{3}$$
$$\alpha_s = 2.526\times 10^7\ \mathrm{pc^{-1}\ cm^3},$$

where λ is the radio wavelength and r_e is the classical electron radius. The dispersion measure contains information about both the average electron density and fluctuations of this density. The inhomogeneities of the electron density along the line of sight can be characterized by the structure function

$$D_{\mathrm{DM}}(\rho) = \langle[\mathrm{DM}(\rho_1+\rho) - \mathrm{DM}(\rho_1)]^2\rangle, \tag{4}$$

where ρ is the two-dimensional vector of the relative displacement of two observation points in the plane of the sky. Note that the length R of the paths in $\mathrm{DM}(\rho_1+\rho)$ and $\mathrm{DM}(\rho_1)$ must be the same, so that $D_{\mathrm{DM}}(\rho)$ is determined only by a displacement of the path perpendicular to the line of sight. The structure function for fluctuations of the dispersion measure is related to the spatial spectrum of the electron-density fluctuations $\Phi_{N_e}(\mathbf{q}_\perp, q_l)$ by the formula

$$D_{\mathrm{DM}}(\rho) = (1/3\times 10^{18})^2 \tag{5}$$
$$\times\int dl\int d^2\mathbf{q}_\perp[1-\cos(\mathbf{q}_\perp\rho)]\Phi_{N_e}(\mathbf{q}_\perp, q_\parallel = 0),$$

where $\mathbf{q}_\perp$ and $q_\parallel$ are components of the spatial frequency vector, l is in cm, and and q is in $\mathrm{cm^{-1}}$.

In scintillation theory, the main quantity is the phase-fluctuation structure function S (calculated in a linear geometrical-optics approximation):

$$D_S(\rho) = \langle[S(\rho_1+\rho) - S(\rho_1)]^2\rangle. \tag{6}$$

The quantity $D_S(\rho)$ is linearly related to $D_{\mathrm{DM}}(\rho)$:

$$\begin{aligned}D_S(\rho) &= K_1(f_0/f)^2 D_{\mathrm{DM}}(\rho),\\ K_1 &= 6.38\times 10^{14}\ \mathrm{pc^{-2}cm^6}.\end{aligned} \tag{7}$$

Formula (5) corresponds to the case when the integration path moves parallel to itself, which will be true for an indefinitely distant source (the plane-wave case). When the source is at a finite distance (the spherical-wave case), the gradient of the phase-fluctuation structure function should be used instead of D_S:

$$D(\rho) = dD_S(\rho)/dl. \tag{8}$$

For a fixed source position and displacement of the observer by the vector rho, the phase structure function for a spherical wave is expressed in the form

$$D_S(\rho) = \int_0^R drD[(r/R)\rho]. \tag{9}$$

Here, the integration is carried out from the source to the observer. The function $D(\rho)$ is related to the quadratic Fourier spectrum of the electron-density fluctuations [4]:

$$D(\rho) = 4\pi(\lambda r_e)^2 \tag{10}$$
$$\times\int d^2\mathbf{q}_\perp[1-\cos(\mathbf{q}_\perp\rho)]\Phi_{N_e}(\mathbf{q}_\perp, q_\parallel = 0).$$

If the position of the observer is fixed and the source position moves by an angle θ, the phase-fluctuation and dispersion-measure structure functions obey the relations

$$D_S(\theta) = \int_0^R drD[(R-r)\theta], \tag{11}$$

$$D_{\mathrm{DM}}(\theta) = (1/K_l)(f/f_0)^2 D_S(\theta). \tag{12}$$

Here, the integration is likewise carried out from the source to the observer.

When the source moves with a linear velocity $\mathbf{V}_\perp$ in the plane perpendicular to the line of sight, the angular displacement of the source over a time t is

$$\begin{aligned}\theta &= \mathbf{V}_\perp t/R = \Omega t,\\ \Omega &= \mathbf{V}_\perp/R\end{aligned} \tag{13}$$

and the temporal phase-fluctuation structure function is

$$D_S(t) = \int_0^R drD[\Omega t(R-r)/R], \tag{14}$$

where Ω is the angular velocity of the source.

Direct measurement of fluctuations of the dispersion measure or phase is possible for the largest scales of the ray divergence. For the smallest scales, the phase-fluctuation structure function can be determined by the coherence function of the field, which

corresponds to the response of an interferometer with the baseline ρ:

$$B_E(\rho) = \langle I\rangle \exp[-(1/2)D_S(\rho)], \qquad (15)$$

where $\langle I\rangle$ is the average flux of the source. Let the scale of the field coherence be

$$D_S(\rho_0) = 1. \qquad (16)$$

When the phase-fluctuation structure function depends only on the absolute value of ρ and has a quadratic form, the scale of the field coherence is related to the scattering angle θ_0 (the apparent angular radius of the source at half the maximum $B_E(\rho)$) as follows:

$$\theta_0 = 1/(k\rho_0), \qquad (17)$$

where k is the wave number. For isotropic inhomogeneities and a power-law form for $D_S(\rho)$, we obtain

$$D_S(\rho) = (k\theta_0\rho)^{n-2}, \qquad (18)$$

where n is the power-law index of the three-dimensional electron-density fluctuation spectrum $\Phi_{N_e}(q)$.

The phase-fluctuation structure function can be determined from the correlation function of the flux fluctuations associated with the diffractive scintillations:

$$B_I(t) = \langle I\rangle^2 \exp[-D_S(t)]. \qquad (19)$$

We define the scintillation timescale $t_{\rm dif}$ by the expression

$$D_S(t_{\rm dif}) = 1/2. \qquad (20)$$

The relationship between the scintillation timescale and the spatial scale of the diffractive scintillations, which is equal to the scale of the field coherence and is determined by (16), depends on the medium along the line of sight. For a statistically homogeneous medium,

$$\rho_0 = 2^{n-2}V_\perp t_{\rm dif} = \Omega R t_{\rm dif}. \qquad (21)$$

For a medium that is statistically inhomogeneous, the relationship between the spatial and temporal scales depends on the distribution of the medium along the line of sight. The spatial phase-fluctuation structure function is determined by an integral of the form (10), with the medium situated near the observer making the most important contribution. The temporal structure function is determined by an integral of the form (14), with the most important contribution being made near the source.

We can estimate the phase-fluctuation structure function for a scale on the order of the refractive-scintillation scale [4]

$$b_{\rm ref} \cong R\theta_0 \qquad (22)$$

using the refractive scintillation index. We obtain for isotropic inhomogeneities [4]

$$m^2_{\rm ref} = \lambda^2 r_e^2 R^2 \qquad (23)$$
$$\times \int dq_\perp q_\perp^5 \int_0^R dr (R/r)^2((R/r)-1)^2$$
$$\times \Phi_{N_e}[q_\perp(R/r), q_\parallel = 0]\exp(-F),$$

$$F = \int_0^r dr' D[(q_\perp r'/k)((R/r)-1)] \qquad (24)$$
$$+ \int_r^R dr' D[(q_\perp/k)(R-r')].$$

The scintillation index in (23) is determined by the turbulence spectrum Φ_{N_e} near the spatial frequency $1/b_{\rm ref}$ and by the filter $\exp(-F)$, which, in turn, is determined by the scattering angle θ_0 and cuts off the contribution of the turbulence spectrum at frequencies exceeding $1/b_{\rm ref}$. We can express the refractive-scintillation index in terms of the phase-fluctuation structure function on the scale of the refractive scintillations. We will use $VT_{\rm ref}$ for this scale, where $T_{\rm ref}$ is the characteristic timescale for refractive scintillations and V is the source velocity:

$$m^2_{\rm ref} = A(n)D_S(VT_{\rm ref})(T_{\rm ref}/t_{\rm dif})^{-2}. \qquad (25)$$

Here, $A(n)$ is a numerical coefficient that depends on the local power-law index n of the turbulence spectrum and on the distribution of the medium along the line of sight, and $t_{\rm dif}$ is the characteristic timescale for diffractive scintillations, determined by (20). For a statistically homogeneous medium with n close to four, we obtain

$$A(n) \cong 6(4-n), \quad 4-n \ll 1. \qquad (26)$$

Relations (25) and (26) remain valid for a statistically homogeneous layer near the source, with the temporal features of the scintillations being determined by the motion of the source. In this case, $D_S(VT_{\rm ref})$ describes the structure function of phase fluctuations at the outer boundary r_0 of the layer. The behavior of $m_{\rm ref}$, $D_S(VT_{\rm ref})$, $T_{\rm ref}$, and $t_{\rm dif}$ is presented in more detail in [4].

We can also estimate the phase-fluctuation structure function using the index for weak scintillations. We obtain for this regime [5]

$$m^2_{\rm weak} \cong m_0^2 = B(n)D_S(b_{Fr}). \qquad (27)$$

The numerical coefficient $B(n)$ depends on the index n and the distribution of the medium along the line of

sight. For a statistically homogeneous medium with n tending to four, we find

$$B(n) \cong \pi(4-n)/4, \quad 4-n \ll 1. \qquad (28)$$

We can also study the temporal phase-fluctuation structure function using the temporal structure function for intensity fluctuations due to weak scintillations. For small timescales,

$$t < t_{\rm weak}, \qquad (29)$$

where $t_{\rm weak}$ is the characteristic timescale for weak scintillations, we obtain

$$D_I(t) \cong D_S(t). \qquad (30)$$

We now consider the question of how to correct the D_S data derived from various observations to obtain uniform sampling. The recalculation of data from one frequency to another follows the function (7), which is general and does not depend on the models for the medium. The recalculation of the D_S value obtained for some dispersion measure DM to a standard DM_0 depends on the value of the dispersion measure itself. For low dispersion measures, the variation of DM is mainly determined by variations of the distance R [3]. For high dispersion measures, the variations of DM are due primarily to variations of the electron density N_e [3, 4]. The relation of D_S to DM takes the form [3, 4]

$$D_S(\rho, f, \mathrm{DM}) = (f_0/f)^2(\mathrm{DM}/\mathrm{DM}_0)D_S(\rho, f_0, \mathrm{DM}_0),$$
$$\mathrm{DM} < \mathrm{DM}_0 = 30\ \mathrm{pc/cm}^3, \qquad (31)$$
$$D_S(\rho, f, \mathrm{DM}) = (f_0/f)^2(\mathrm{DM}/\mathrm{DM}_0)^\gamma D_S(\rho, f_0, \mathrm{DM}_0),$$
$$\mathrm{DM} > \mathrm{DM}_0, \qquad (32)$$
$$\gamma \cong 4.$$

3. CONSTRUCTION OF THE PHASE STRUCTURE FUNCTIONS

To construct a composite phase structure function $D_S(\rho)$ describing a large range of spatial scales and amplitudes, we must use data obtained at various frequencies using various methods. In contrast to [1], we take into account the inhomogeneous component of the interstellar medium at distances of about 1 kpc and more from the Earth. For this purpose, we used data on diffractive and refractive scintillations of pulsars with dispersion measures from 30 to 100 pc cm^3, as well as measurements of scattering angles and variations of pulse arrival times introduced by inhomogeneities of the interstellar plasma along the line of sight. We used data on pulsars in globular clusters to obtain $D_S(\rho)$ data for the largest spatial scales.

3.1. Reduction of the Phase-Fluctuation Structure Function to the Same Physical Conditions

To compare data on the phase-fluctuation structure function obtained for various pulsars and various conditions for passage of the radiation through the interstellar medium, we must reduce these data to a single set of physical conditions, namely to a single effective thickness R_0 and equivalent electron density N_e for the medium.

It is known that the turbulent interstellar plasma consists of two main components: A and B [2]. The A component dominates at low dispersion measures $\mathrm{DM} < \mathrm{DM}_0 \cong 30$ pc cm^3. This medium corresponds to the space between the arms of the Galaxy. It is characterized by small variations of the electron density N_e, with variations of the distance R being the main origin of scintillations and variations in the scattering parameters. Consequently, the dispersion measure becomes a measure of distance: $\mathrm{DM} \propto R$. It is convenient to use the distance corresponding to DM_0 as a standard distance: $R_0 \cong 1$ kpc.

When reducing the D_S to the standard distance, we can use for the A component of the turbulent plasma the relation

$$D_{S,0,\mathrm{A}}(\rho) = D_S(\rho)(\mathrm{DM}_0/\mathrm{DM}). \qquad (33)$$

At high dispersion measures $\mathrm{DM} > \mathrm{DM}_0$, the B plasma component makes the main contribution to scattering and scintillations. This component corresponds to the spiral arms of the Galaxy. Here, the variations of the electron density N_e become the main source of variations in the dispersion measure, scattering parameters, and scintillation [2–4].

We can write for the parameter $C^2_{N_e}$ describing the electron-density fluctuations [4]

$$C^2_{N_e} \propto N_e^\alpha \propto \mathrm{DM}^\alpha. \qquad (34)$$

Consequently, the reduction of the phase-fluctuation structure function to a standard dispersion measure obeys the law

$$D_{S,0,\mathrm{B}}(\rho) = D_{S,\mathrm{B}}(\rho)(\mathrm{DM}_0/\mathrm{DM})^\alpha. \qquad (35)$$

When comparing data on the A and B components of the turbulent interstellar plasma, we must take into account the fact that identical dispersion measures DM do not correspond to identical thicknesses R and densities N_e. The B component represents an inhomogeneous medium, and the region of enhanced density has a characteristic angular size of the order of the arm thickness, $R_{0,\mathrm{B}} \cong 300$ pc. As a rule, scintillations for pulsars with $\mathrm{DM} > 30$ pc cm^3 occur in such regions of enhanced density. Correcting the $D_{S,0,\mathrm{B}}$ to the standard electron density and thickness of the A component, we obtain

$$D_{S,0,\mathrm{B}}(\rho)_{\mathrm{B}\to\mathrm{A}} = (L_{0,\mathrm{B}}/L_{0,\mathrm{A}})^{\alpha-1} D_{S,0,\mathrm{B}}(\rho). \qquad (36)$$

We will use these normalizing laws to construct the composite structure function for a large range of spatial scales. We shall determine the index α in Section 3.2 using observational data.

3.2. Data on Diffractive Scintillations and the Angular Sizes of Pulsars

We showed in Section 2 that the phase structure function is determined by the coherence scale of the field ρ, and we obtain for a power spectrum

$$D_S = (f/f_0)^2 \times (\rho_0/\rho)^\beta, \qquad (37)$$

where $\beta = n - 2$ and $\beta = 1.67$ for a Kolmogorov spectrum. For the normalization, we take $f_0 = 1000$ MHz and $\rho_0 = 7.84 \times 10^7$ m—the coherence scale for PSR 0329+54 at the frequency f_0. When using data on diffractive scintillation of pulsars, we assume that the coherence scale is equal to the spatial scale for the diffractive scintillations, which is

$$\rho\,[\mathrm{m}] = 2.77 \times 10^5 t_{\mathrm{dif}}[\mathrm{min}] \times R[\mathrm{kpc}] \times \Omega[10^{-3}\ \mathrm{arcsec/yr}], \qquad (38)$$

where Ω and R are the angular velocity and distance to the pulsar, which we took from the pulsar catalog [6]. We use characteristic pulsar scintillation timescales t_{dif} measured at various frequencies from the literature (published mainly in [2, 7–11]), including only those pulsars for which the angular velocity was measured with an accuracy not worse than 100% (see [6]). Pulsars in supernova remnants (the Crab and Vela pulsars) were omitted, since their scintillations are associated with a thin layer of high-density, turbulent plasma surrounding the pulsar, whereas the scintillations of the selected pulsars are due to inhomogeneities of the electron density in the spiral arms of the Galaxy.

Since the interstellar medium is strongly inhomogeneous at distances greater than 1 kpc (as was shown, for example, in [3, 4]) and we are using data on pulsars located at various distances and in various directions in our Galaxy, we must reduce these data to the same physical conditions, as was stated in Section 3.1. We have studied the coherence scale and phase structure function as functions of the dispersion measure DM. We used data on t_{dif} obtained at 1000 MHz to construct the function ρ(DM) plotted in Fig. 1. The dependence on the dispersion measure is clearly visible, with the correlation coefficient being -0.9. The slope of the least-squares line fit to the data corresponds to $\alpha = -2.6$. Figure 2 presents the function D_S(DM) on a logarithmic scale. Here, we have used $n = 11/3$ (a Kolmogorov spectrum), i.e., $\beta = 1.67$, and data for various frequencies. The dependence on the dispersion measure is clearly visible,

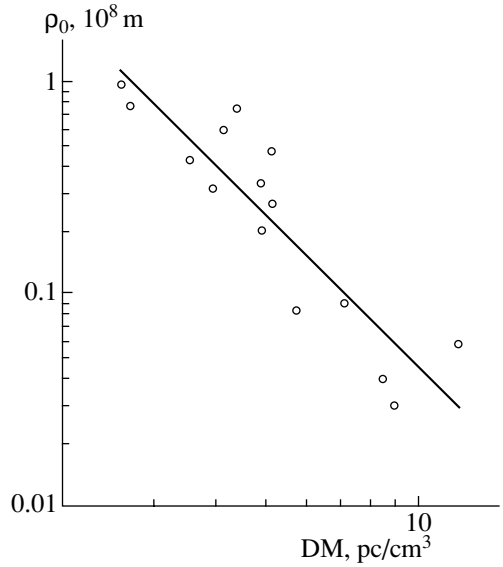

Fig. 1. The coherence scale as a function of the dispersion measure determined from the characteristic timescale for diffractive scintillations of pulsars at 1000 MHz. The line represents a least-squares fit to the data.

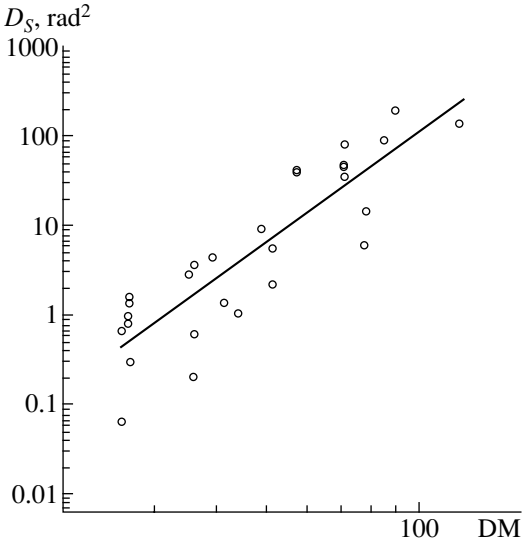

Fig. 2. Phase structure function as a function of the dispersion measure determined from pulsar scintillation data. The slope of the least-squares line shown corresponds to $\alpha = 4.1$. The data for various frequencies have been reduced to a frequency of 1000 MHz.

with the correlation coefficient being 0.89. The slope of the least-squares line corresponds to $\alpha = 4.1$. Note that α is also varied when β is varied; for example, $\alpha = 3.8$ when $\beta = 1.5$. If the interstellar medium were homogeneous, we would expect that $D_S \sim$ DM (the dispersion measure is a measure of the distance). However, the considerably steeper dependence on DM shows that the dispersion measures for pulsars

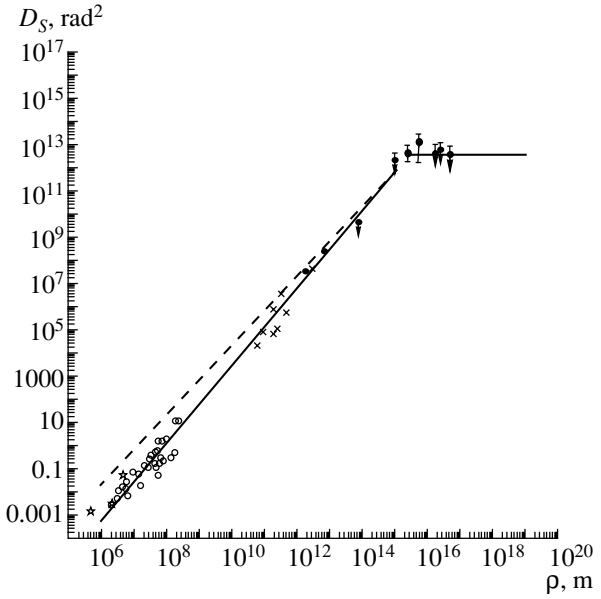

Fig. 3. Composite phase structure function as a function of the spatial scale of the electron density fluctuations in the interstellar medium. The open circles correspond to diffractive-scintillation measurements, the asterisks to scattering-angle measurements, the daggers to refractive-scintillation measurements, and the filled circles to pulsar timing measurements and measurements of variations of the dispersion measures in close pairs of pulsars in globular clusters. The normalization of the structure function reduces the observational data to the same physical conditions in the turbulent plasma, as is described in Section 3.1. The lines show the theoretical functions $D_S(\rho)$ [Eqs. (44) and (45)] for $n = 11/3$ (a Kolmogorov spectrum, solid) and for $n = 3.5$ (dashed), with the outer turbulence scale being $L_0 = 9 \times 10^{14}$ m and $\langle \Delta s^2 \rangle = 1.75 \times 10^{12}$.

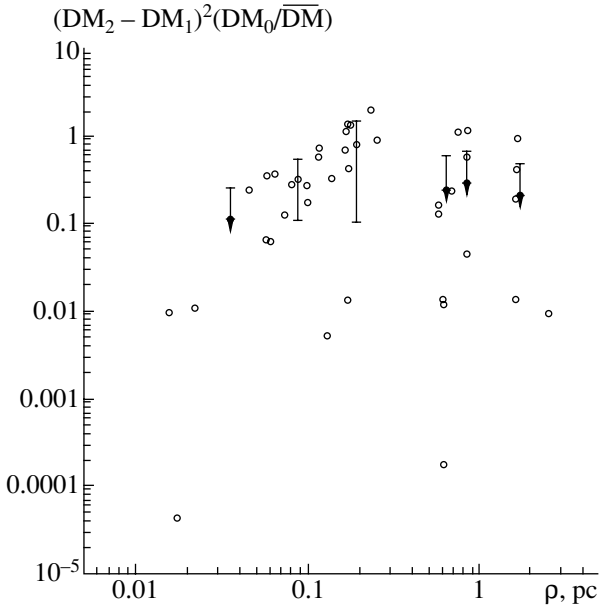

Fig. 4. Square of the difference of the dispersion measures for close pairs of pulsars in globular clusters reduced to $DM_0 = 30$ pc/cm^3 as a function of the distance between. The average values of this quantity in intervals for the distance between sources are also shown. Each interval contains no fewer than six pulsar pairs. The errors correspond to the rms deviation (1σ). The upper limits correspond to cases when σ was more than twice the values themselves.

with DM > 30 pc/cm^3 are predominantly determined by the plasma electron density, and not the distance to the pulsar. This was also indicated in [4, 12]. Further, we shall use the following normalization:

$$D_S = (f/f_0)^2 \times (\mathrm{DM_0/DM})^{4.1}, \qquad (39)$$

when calculating the structure functions obtained using various observational data. The data on diffractive scintillations are presented by the open circles in the composite structure function (Fig. 3).

When constructing D_S, we also used measurements of the scattering angles for several pulsars obtained at 326 MHz [13]. The characteristic spatial scale for the scattering was determined by the relation

$$\rho[\mathrm{m}] = 10^8/(f[10^2\ \mathrm{MHz}]\theta_{\mathrm{sc}}[\mathrm{angular\ ms}]), \qquad (40)$$

where θ_{sc} is the angular diameter of the scattering disk. The corresponding $D_S(\rho)$ values are shown by asterisks in Fig. 3.

3.3. Data on Refractive Scintillations of Pulsars and Variations of Pulse Arrival Times

The characteristic scintillation timescale $\mathrm{T_{ref}}$ and the pulsar velocity V (assumed to be much greater than the velocities of the observer and medium) determine the spatial scale for refractive scintillations:

$$\rho[\mathrm{m}] = 8.64 \times 10^{11}\ \mathrm{T_{ref}[days]}\ V[10^2\ \mathrm{km/s}]. \qquad (41)$$

We use the parameters for refractive scintillations of pulsars derived from observations of long-term variations of the signals at 610 MHz [4, 14] due to large-scale inhomogeneities of the interstellar plasma. The phase-fluctuation structure function is determined by (25) and (26). Data on refractive scintillations of pulsars are shown in Fig. 3 by daggers.

We also used estimates of the phase structure function at 1.4 GHz based on an analysis of long-term variations of the dispersion measure of the millisecond pulsar PSR 1821-24 [15]. These estimates, appropriately normalized, are shown in Fig. 3 by filled circles. We estimated an upper limit for $D_S(\rho)$ on spatial scales of 1.3×10^{14} m (Fig. 3) from the rms fluctuation $\sigma_{\delta t} = 1$ ms of the pulse arrival times for PSR 0329+54 obtained at 102 MHz over an interval of 30 yrs [16].

3.4. Data on Pulsars in Globular Clusters

To estimate the phase structure function for large spatial scales, we have analyzed variations of the dispersion measures for pairs of pulsars separated by small angular distances, $\Delta l \leq 0.1°$. The quantity Δl is the square root of the sum of the squared coordinates of the pulsars, i.e., their right ascensions and declinations from pulsar catalogs. We selected 52 pairs of pulsars in globular clusters that satisfy this condition, mainly in 57 Tuc and M15. Figure 4 shows the square of the differences of the dispersion measures for each pulsar pair reduced to the dispersion measure $\mathrm{DM}_0 = 30$ pc/cm^3 as a function of the projection ρ of the distance between pulsars onto the effective layer of the interstellar medium responsible for their scintillation. As for extragalactic sources, this layer turns out to correspond to the plane of the Galaxy, which has a thickness $R_0 \cong 1$ kpc. We defined ρ as follows: $\rho = R_0 \times \sin(\Delta l)/\sin b$, where b is the Galactic latitude of the pulsar. The filled circles represent averages for longitudinal intervals containing no fewer than six points. The resulting values represent an estimate of the structure function, and are shown in Fig. 3 (after normalizing) by the filled circles with error bars.

4. RESULTS

Figures 3 and 4 show that the structure function stops its growth at spatial scales $\rho \approx 0.05 - 2$ pc and takes on the constant value $D_{S,\mathrm{sc}}(\rho \to \infty) = 2\langle(\Delta S)^2\rangle \cong 3.5 \times 10^{12}$. Thus, we have detected the outer scale for the electron-density fluctuation spectrum. At the half-saturation level of the structure function, this scale is $\rho_S \approx 0.03$ pc. Note that the structure function is generally well described by a Kolmogorov spectrum over ten orders of magnitude in spatial scales for the inhomogeneities. However, the observational data can also be described by a spectrum with an index $n = 3.5$, if we admit a local steepening near the scale $\rho \approx 10^{11}$ m. Distinguishing confidently between models will require higher precision measurements.

To describe the turbulence spectrum more accurately over the entire range of scales while allowing for an outer scale, we used a Karman model for the quadratic Fourier spectrum of the electron-density (N_e) fluctuations [17]:

$$\Phi_{N_e}(\mathbf{q}) = K(n)\langle(\Delta N_e)^2\rangle L_0^3/(1 + |\mathbf{q}|^2 L_0^2)^{n/2}, \quad (42)$$
$$K(n) = \Gamma(n/2)/(\pi\sqrt{\pi}\,\Gamma((n-3)/2)),$$

where L_0 is the outer turbulence scale. Substituting the spectrum (42) into (10) and (11) yields the phase structure function for a statistically homogeneous medium:

$$D_{S,\mathrm{sc}} = 2\langle(\Delta S)^2\rangle \left[1 - (1/2)^{(n-2)/2}\Gamma((n-2)/2)\int_0^1 dx(\rho x/L_0)^{(n-2)/2}K_{(n-2)/2}\rho x/L_0\right]. \quad (43)$$

The function $D_{S,\mathrm{sc}}$ displays simple asymptotics. For large ρ,

$$D_{S,\mathrm{sph}} \cong 2\langle(\Delta S)^2\rangle, \quad \rho > L_0, \quad (44)$$
$$\langle(\Delta S)^2\rangle = G(n)(\lambda r_e)^2\langle(\Delta N_e)^2\rangle L_0 R,$$
$$G(n) = 2\pi\sqrt{\pi\Gamma((n-2)/2)/\Gamma((n-3)/2)}.$$

For small ρ, we obtain

$$D_{S,\mathrm{sc}}(\rho) \cong 2M(n)\langle(\Delta S)^2\rangle(\rho/L_0)^{(n-2)}, \quad \rho \ll L_0, \quad (45)$$
$$M(n) = \Gamma((n-2)/2)/[2^{n-2}(n-1)\Gamma(n/2)].$$

Figure 3 shows the asymptotics of (44) and (45). The solid curves show the asymptotics for $n = 11/3$, $L_0 = 9 \times 10^{14}$ m, and $\langle(\Delta S)^2\rangle = 1.75 \times 10^{12}$. The dashed curve shows the asymptotics of (45) for $n = 3.5$. We can see that a single turbulence spectrum with $n = 3.5$ is in worse agreement with the observations. Therefore, in the power-law interval, the real turbulence spectrum for the interstellar plasma is generally close to a Kolmogorov spectrum. This is true for both the diffusive component A [1] that is close to the Sun and component B (more precisely BI, in accordance with [18]) of the interstellar plasma associated with the spiral arms of the Galaxy. However, we must bear in mind that the spectrum may have a more complicated structure, whose detection requires more accurate measurements.

Figure 5 presents the structure function determined from the same observational data, but with the normalization used in [1] for the diffusive component:

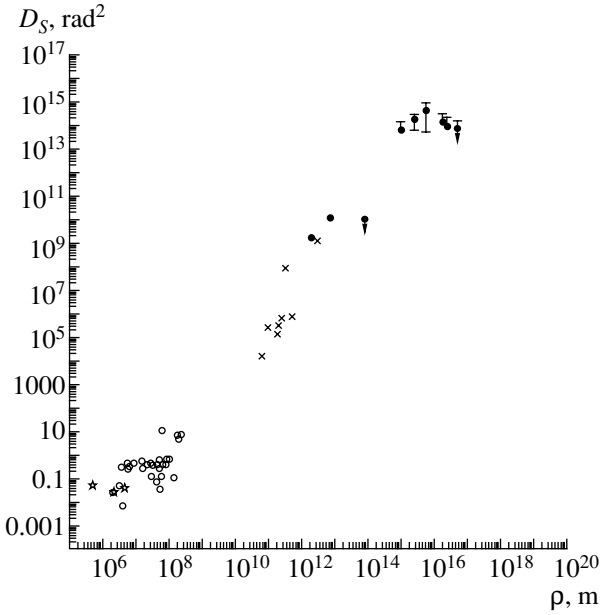

Fig. 5. Same as Fig. 3 but normalized to a single distance of $R_0 = 1$ kpc.

$D_S = D_{S,1\mathrm{GHz}}\,(R_0/R)$, where $R_0 = 1$ kpc. The scatter of the resulting values is more pronounced here, in support of our normalization.

5. DISCUSSION

We have found that the turbulence spectra for the A and BI (according to [18]) components of the interstellar plasma agree well with a Kolmogorov spectra on scales from a thousand kilometers to a hundredth of a parsec. We have also determined the outer turbulence scale to be $L_0 = 9 \times 10^{14}$ m. Strictly speaking, this scale corresponds only to component A, i.e., to the plasma between the spiral arms, since pulsars in globular clusters are high-latitude objects, and variations of their dispersion measures are associated with component A. Knowing $\langle(\Delta S)^2\rangle$ and L_0, we can determine the variance of the electron-density fluctuations:

$$\langle(\Delta N_e)^2\rangle = \langle(\Delta S)^2\rangle/[G(n)(\lambda r_e)^2 L_0 R]. \quad (46)$$

Assuming $n = 11/3$ and $R = 1$ kpc, we obtain

$$\langle(\Delta N_e)^2\rangle^{(1/2)} = 4.4 \times 10^{-3}\ \mathrm{cm}^{-3}. \quad (47)$$

We can determine $\langle N_e\rangle$ and $\langle N_e^2\rangle$ using $R =$ 1 kpc, DM = 30 pc/cm^3, and EM = 2 pc/cm^6 (with the emission measure EM taken from [3]):

$$\langle N_e\rangle = \mathrm{DM}/R = 0.03\ \mathrm{cm}^{-3}, \quad (48)$$

$$\langle(N_e)^2\rangle^{1/2} = (\mathrm{EM}/R)^{1/2} = 0.045\ \mathrm{cm}^{-3}. \quad (49)$$

We can also determine the filling factor

$$f = \langle N_e\rangle^2/\langle N_e^2\rangle = 0.5. \quad (50)$$

The relative level of the turbulent fluctuations is important for the physics of turbulence:

$$\delta = \langle(\Delta N_e)^2\rangle/\langle N_e^2\rangle \cong 10^{-2}. \quad (51)$$

Consequently, the plasma turbulence between the arms is undoubtedly weak. However, in spite of its relatively weak level, the turbulence can be important for the energy balance of the plasma. Via nonlinear cascade processes, the energy of the turbulent fluctuations is transferred from large scales to small scales and then goes into heating. The rate of the energy dissipation is on the order of

$$\Gamma = dW_{\mathrm{turb}}/dt \cong -\gamma W_{\mathrm{turb}}, \quad (52)$$

where γ is the nonlinear damping rate. When estimating γ, we shall use the scheme for the generation of turbulence described in [19] together with new data on the turbulence spectrum. We shall assume that the elementary turbulence is due to Alfven and magnetoacoustic waves. We shall also assume that the Alfven speed v_a is close to the sound speed v_s, and that the nonlinear wave interactions are determined by three-wave processes. In this case,

$$\gamma \approx \delta\omega_0 \approx \delta v_s/L_0, \quad (53)$$

where ω_0 is the main turbulence frequency. The energy of the turbulence can be expressed in terms of the thermal energy of the plasma W_T:

$$W_{\mathrm{turb}} \approx \delta W_T. \quad (54)$$

Substituting (53) and (54) into (52), we obtain

$$\Gamma \approx \delta^2(v_s/L_0)W_T. \quad (55)$$

Assuming $v_s = 10$ km/s and $T = 10\,000$ K yields

$$\Gamma \approx 4 \times 10^{-29}\ \mathrm{erg/cm^3\ s}. \quad (56)$$

The rate at which plasma energy is lost to radiation is determined by the expression [20]

$$\Lambda = N_e^2\lambda(T). \quad (57)$$

Assuming $N_e = 0.03$ cm^{-3}, $T = 10\,000$ K, and using the $\lambda(T)$ value tabulated in [20], we obtain

$$\Lambda \approx 3 \times 10^{-29}\ \mathrm{erg/cm^3\ s}. \quad (60)$$

Consequently, the turbulent source of heating compensates the radiation losses. Note that our estimates of the turbulence energy and plasma heating source are fairly rough. A more accurate estimate requires knowledge of the magnetic-field strength. However, our results make it quite clear that turbulence is an important energy component of the plasma, and must be taken into account when constructing a model for the turbulence or a general model for the generation of the plasma in the space between the spiral arms of the Galaxy.

ACKNOWLEDGMENTS

This work was supported by the Russian Foundation for Basic Research (project no. 00-02-17850) and INTAS (project 00-849) as well as the NSF (grant no. AST 0098685).

REFERENCES

1. J. W. Armstrong, B. J. Rickett, and S. R. Spangler, Astrophys. J. **443**, 209 (1995).
2. J. M. Cordes, J. M. Weisberg, and V. Boriakoff, Astrophys. J. **288**, 221 (1985).
3. A. V. Pynzar' and V. I. Shishov, Astron. Zh. **74**, 663 (1997) [Astron. Rep. **41**, 586 (1997)].
4. T. V. Smirnova, V. I. Shishov, and D. R. Stinebring, Astron. Zh. **75**, 866 (1998) [Astron. Rep. **42**, 766 (1998)].
5. A. M. Prokhorov, V. F. Bunkin, K. S. Gochelashvili, and V. I. Shishov, Usp. Fiz. Nauk **114**, 415 (1974) [Sov. Phys. Usp. **17**, 826 (1974)].
6. J. H. Taylor, R. N. Manchester, and A. G. Lyne, Astrophys. J., Suppl. Ser. **88**, 529 (1993).
7. J. M. Cordes, Astrophys. J. **311**, 183 (1986).
8. V. M. Malofeev, T. V. Smirnova, A. G. Soin, and N. V. Shapovalova, Pis'ma Astron. Zh. **21**, 691 (1995) [Astron. Lett. **21**, 619 (1995)].
9. N. D. R. Bhat, A. P. Rao, and Y. Gupta, Astrophys. J., Suppl. Ser. **121**, 483 (1999).
10. V. M. Malofeev, V. I. Shishov, W. Sieber, *et al.*, Astron. Astrophys. **308**, 180 (1996).
11. D. C. Backer, Astron. Astrophys. **43**, 395 (1975).
12. V. I. Shishov, V. M. Malofeev, A. V. Pynzar', and T. V. Smirnova, Astron. Zh. **72**, 485 (1995) [Astron. Rep. **39**, 428 (1995)].
13. C. R. Gwinn, N. Bartel, and J. M. Cordes, Astrophys. J. **410**, 673 (1993).
14. D. R. Stinebring, T. V. Smirnova, T. H. Hankins, *et al.*, Astrophys. J. **539**, 300 (2000).
15. I. Cognard and J.-F. Lestrade, Astron. Astrophys. **323**, 211 (1997).
16. T. V. Shabanova, Astrophys. J. **453**, 779 (1995).
17. V. I. Tatarskii, *Wave Propagation in a Turbulent Medium* (Nauka, Moscow, 1967; McGraw-Hill, New York, 1961).
18. A. V. Pynzar' and V. I. Shishov, Astron. Zh. **76**, 504 (1999) [Astron. Rep. **43**, 436 (1999)].
19. A. V. Chasheĭ and V. I. Shishov, Pis'ma Astron. Zh. **6**, 574 (1980) [Sov. Astron. Lett. **6**, 301 (1980)].
20. S. A. Kaplan and S. B. Pikel'ner, *Physics of the Interstellar Medium* [in Russian] (Nauka, Moscow, 1979).

Translated by V. Badin

Astronomy Reports, Vol. 46, No. 9, 2002, pp. 740–746. Translated from Astronomicheskiĭ Zhurnal, Vol. 79, No. 9, 2002, pp. 820–826.

Light-curve Synthesis for Close Binaries Overfilling Their Inner Roche Lobes

V. I. Mikhaĭlishin

Kazan State University, ul. Lenina 18, Kazan, 420008 Tatarstan, Russia

Received June 6, 2000; in final form, November 23, 2001

Abstract—We present a procedure for calculating theoretical monochromatic light curves of close binary systems overfilling their inner Roche lobes. The close binaries are considered in a Roche model with a cold spot on one of the components. The system radiation is calculated in both a blackbody approximation and using model stellar atmospheres, taking into account tidal deformations of the components, limb darkening, gravitational darkening, and the effect of mutual heating of the components. © *2002 MAIK "Nauka/Interperiodica".*

1. INTRODUCTION

Close binary systems have been widely studied using synthesized theoretical light curves. The most widely implemented techniques are those developed by Wilson and Devinney [1], Hill [2], and their modifications. Both methods consider the system geometry in the Roche approximation. The latest versions of codes for the synthesis of theoretical light curves enable the construction of light curves for both detached and contact systems, including those overfilling their inner Roche lobes. Unfortunately, these codes are mostly unavailable.

Here, we describe some procedures for calculating theoretical monochromatic light curves of close binary systems with overfilled inner Roche lobes, developed on the basis of the code of Antokhina [3]. We also use the technique for constructing an ellipsoidal light curve described by Balog *et al.* [4]. The model includes a cold spot on one of the components. We take into account tidal deformations, limb darkening, gravitational darkening, and mutual heating of the components. The radiation of the components is calculated in two ways: in a blackbody approximation and using model stellar atmospheres. We tested the code using the TU Boo [5] and SU Sep [6] systems.

2. CALCULATING THE GEOMETRY OF A CLOSE BINARY OVERFILLING ITS INNER ROCHE LOBE

Let us consider a contact binary consisting of two stars with thin atmospheres that have overfilled their inner Roche lobes and formed a system with a common envelope. We assume that the axial rotation of the components is synchronous with the orbital rotation. The orbits of the stars are taken to be circular. The shape of the common envelope coincides with the Roche equipotential surface of the stars.

We place the origin of a Cartesian coordinate system (X, Y, Z) at the center of mass of the primary, which eclipses the secondary at orbital phase $\Psi = 0$ (Fig. 1). The OX axis is directed along the line connecting the centers of mass of the components, the OY axis is placed in the orbital plane, and the OZ axis is perpendicular to this plane. We denote η to be the angle between the radius vector r to an arbitrary point on the stellar surface and the OX axis, and φ to be the angle between the projection of r onto the YOZ plane and the OY axis. The coordinates of a point in the Cartesian coordinate system can be calculated using the formulas

$$\begin{aligned} x &= r\lambda, \\ y &= r\nu, \\ z &= r\mu, \end{aligned} \tag{1}$$

where λ, ν, and μ denote the directional cosines:

$$\begin{aligned} \lambda &= \cos\eta, \\ \nu &= \sin\eta\cos\varphi, \\ \mu &= \sin\nu\sin\varphi. \end{aligned} \tag{2}$$

Let us suppose that m_1 is the mass of the primary and m_2 that of the secondary. The mass ratio of the components is $q = m_2/m_1 \leq 1$. The distance between the centers of mass of the stars d is taken to be unity. The equation for the equipotential surface in the Roche model in (r, η, φ) coordinates then has the form

$$\Psi = \frac{Gm_1}{d}(\Omega + \text{const}), \tag{3}$$

1063-7729/02/4609-0740$22.00

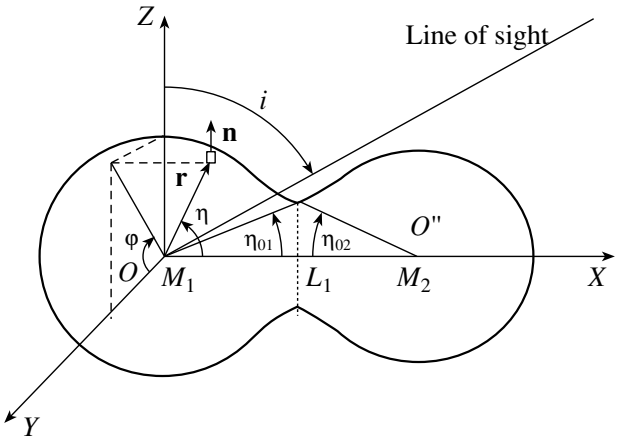

Fig. 1. Geometry of a contact binary ($q = 0.75$, $F = 1.45$).

where Ω is the dimensionless potential and const $= 2q^2/(1+q)^2$. The potential Ω can be written in the form [7]

$$\Omega = \frac{1}{r} + q\left(\frac{1}{\sqrt{1+r^2-2\lambda r}} - \lambda r\right) + \frac{1+q}{2}r^2(1-\nu^2). \qquad (4)$$

We can see from (3) that the potential Ω is a linear function of the true potential Ψ and can be used to determine the equipotential surface describing the shape of the contact close binary system. If necessary, Eq. (3) can be used to translate from the dimensionless to the true potential.

The entire surface of the stars is located between the inner and outer critical Roche surfaces containing the Lagrange points L_1 and L_2. To determine this surface, the coordinates for the inner and outer Lagrange points $L_1(\xi, 0, 0)$ and $L_2(\xi^*, 0, 0)$ must be calculated together with the corresponding potentials. Substituting the coordinates of the Lagrange points into (4), we obtain

$$\Omega_1 = \frac{1}{\xi} + q\left(\frac{1}{1-\xi} - \xi\right) + \frac{1+q}{2}\xi^2, \qquad (5)$$

$$\Omega_2 = \frac{1}{\xi^*} + q\left(\frac{1}{\xi^*-1} - \xi^*\right) + \frac{1+q}{2}\xi^{*2}.$$

The potentials Ω_1 and Ω_2 reach their minimum at the points L_1 and L_2, respectively, making it necessary to solve Eqs. (5) numerically via a direct linear search. The coordinates of the Lagrange points and the corresponding potentials are found simultaneously.

The surface of the primary is determined from (4) under the condition that Ω is constant. We use the overfilling factor F to describe the degree of overfilling

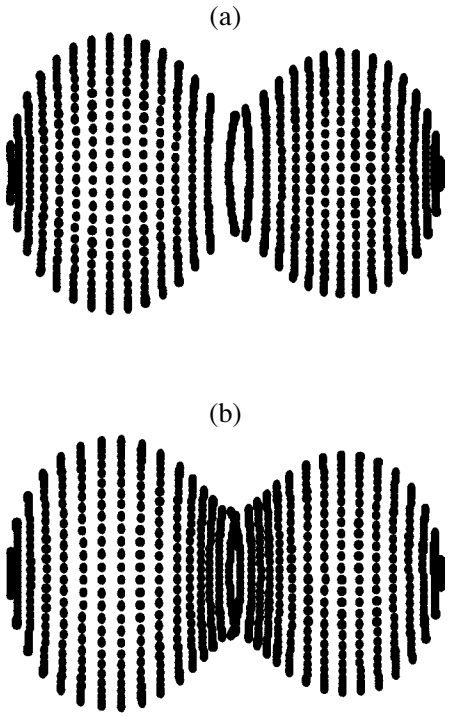

Fig. 2. Division of the contact-binary surface into area elements using (a) uniform and (b) variable steps ($q = 0.75$, $F = 1.45$).

of the inner Roche lobe, defined as follows:

$$F = \frac{\Omega - \Omega_2}{\Omega_1 - \Omega_2} + 1. \qquad (6)$$

Here, $\Omega_2 \le \Omega \le \Omega_1$ and $1 \le F \le 2$. In this way, specifying q and F makes it possible to calculate the potential Ω, which unambiguously determines the common-envelope surface. Let us divide the system into two parts corresponding to the primary and secondary, along the plane perpendicular to the orbital plane and containing the inner Lagrange point L_1. Calculation of the primary's surface requires the determination of the initial value for the angle η_{01}, corresponding to the boundary of the contact area of the stars (Fig. 1). It is apparent that

$$\cos\eta_{01} = \xi/r_{\min 1}. \qquad (7)$$

Further, the stellar surface is divided into area elements and the radius vectors of the areas $r(\eta, \varphi)$ are found from (4) for fixed values of η and φ. The procedure allows a variable step for the η division: starting from some η (which depends on the overfilling factor F), the interval of angles decreases by a factor of two at each step of the division. This method makes it possible to describe the contact region of the stars more exactly without increasing the number of area elements (Fig. 2). First, the temperature distribution in the contact region is calculated more accurately.

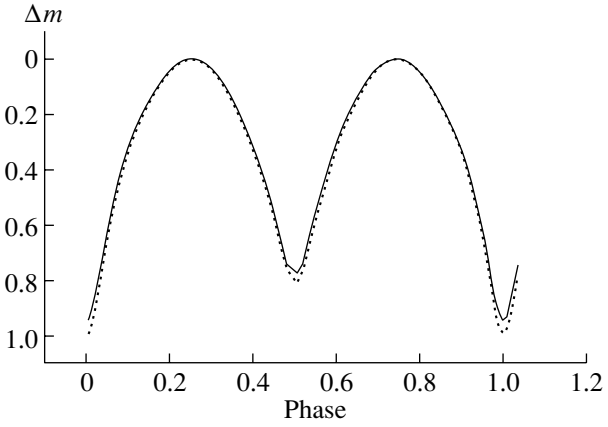

Fig. 3. Effect on the light curve of using variable steps in the division of the stars. The solid curve corresponds to a uniform and the dotted curve to a variable division. The graphs are plotted for $q = 0.6$, $i = 87°$, $F = 1.2$, $T_1 = 4300$ K, and $T_2 = 4500$ K.

Second, a more accurate value for the surface area of the stars is obtained. The use of a variable step when dividing each component into 3200 area elements increases the accuracy of the calculation of the component areas by 0.5–1.5%, depending on the overfilling factor F. Using a variable step during the division yields perceptible results for stars with radiative envelopes ($\beta = 0.25$), when there is a large temperature gradient in the contact region (Fig. 3). For stars with convective envelopes, the difference between the results obtained with variable and uniform steps is somewhat smaller, since, in this case, the increase in the accuracy is reached primarily due to the more accurate determination of the surface area of the components. The coordinates for the centers of area elements are then calculated from (1); they are needed to test the eclipse conditions. Next, the coordinates of the normals to the area elements are found:

$$\mathbf{n} = -\frac{\mathrm{grad}\Omega}{|\mathrm{grad}\Omega|} = (l, m, n). \tag{8}$$

In addition, it is necessary to determine the gravitational acceleration at a given point $g = |\mathrm{grad}\Omega|$, as well as the average gravitational acceleration over the surface of the primary g_{01}. Since the star has two planes of symmetry in the Roche model, sets of r, n, g for only one-quarter of the surface are calculated and stored in the computer memory.

The geometry of the secondary is calculated as follows. We introduce a coordinate system (X^*, Y^*, Z^*) with its origin at the center of mass of the secondary. The OX^* axis is directed towards the center of mass of the primary, the the OY^* axis is directed opposite to OY, and the OZ^* axis is parallel to the OZ axis. The relationship between the (X, Y, Z) and (X^*, Y^*, Z^*) systems is specified by the formulas

$$\begin{aligned} x &= 1 - x^*, \\ y &= -y^*, \\ z &= z^*. \end{aligned} \tag{9}$$

The surface of the secondary is calculated in accordance with (3); however, in this case, we substitute the inverse mass ratio $q^* = 1/q$. The angle η_{02} (Fig. 1) will now be the initial angle for the division into area elements, and is determined from the equation

$$\tan\eta_{02} = \xi\tan\eta_{01}/(1 - \xi). \tag{10}$$

All further calculations are analogous to those for the primary. The radius vectors, normal vectors, coordinates of the centers of area elements on the surface of the secondary, and gravitational acceleration are determined in the (X^*, Y^*, Z^*) coordinate system.

We verified the accuracy of our calculation of the contact system's geometry using the tables of Mochnacki [8]. When each star is divided into 3200 areas, the discrepancy with the tabulated values is less than 0.5% for both the area and three-dimensional radii of the components.

3. CALCULATION OF THE RADIATION OF A CLOSE BINARY

We will assume that the stars radiate as blackbodies. Let us consider the radiation from an area element dS on the surface of the primary. The intensity of the radiation emitted by the area at a given wavelength λ at an angle γ to the normal is specified by the formula

$$\begin{aligned} dI_\lambda \\ = B_\lambda(T)[1 - u_1(\lambda, T)(1 - \cos\gamma)]\cos\gamma dS, \end{aligned} \tag{11}$$

where $u_1(\lambda, T)$ is the linear limb darkening coefficient for the primary, $T(r)$ is the temperature of the area, and $B_\lambda(T)$ is the Planck function. The area of the area element is calculated from the formula

$$dS = \frac{r^2(\eta, \varphi)\sin\eta d\eta d\varphi}{\lambda_r l + \mu_r m + \nu_r n}. \tag{12}$$

The temperature of the area taking into account gravitational darkening is

$$T_0(r) = T_1\left[\frac{g(r)}{g_0}\right]^{\beta_1}, \tag{13}$$

where T_1 is the average effective temperature of the star without taking into account heating of its surface by radiation from its neighbor (to first approximation, this can be determined from the spectral type), and β_1 is the gravitational-darkening coefficient. Formula (13) is not valid in the vicinity of the Lagrange

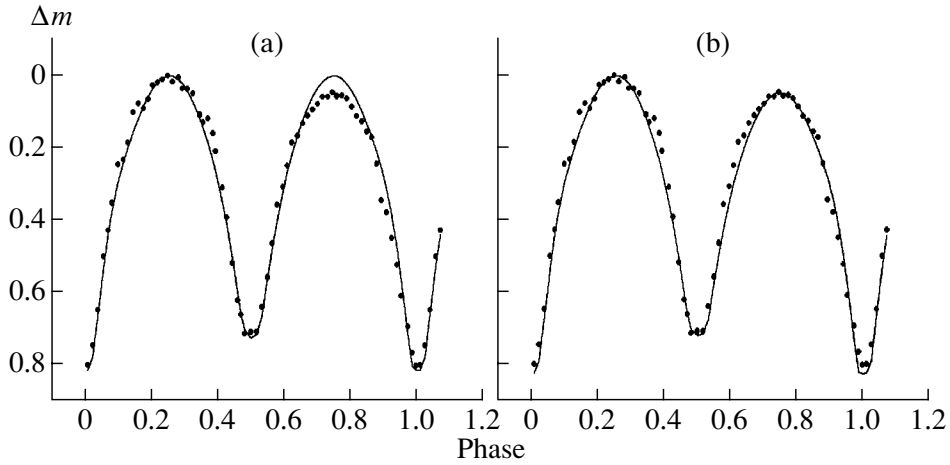

Fig. 4. Theoretical light curves of TU Boo (curve): (a) solution without a spot ($q = 0.498$, $i = 87°.3$, $F = 1.2856$, $T_1 = 5800$ K, $T_2 = 5735$ K, $\beta_1 = \beta_2 = 0.32$); (b) solution with a cold spot on the secondary ($q = 0.498$, $i = 87°.3$, $F = 1.2856$, $T_1 = 5800$ K; $T_2 = 5735$ K; $\beta_1 = \beta_2 = 0.32$, $\varphi_0 = 78°$, $\eta_0 = 90°$, $R = 17°$, $T_f = 0.857$ K). The observational data (points) were taken from [5].

point L_1. However, this region contributes fairly little to the total radiation of the system, and this can be neglected. Numerical calculations indicate that the variations in the light curve caused by a change in β by a factor of two in the contact region do not exceed 0.1%.

The temperature of an area element taking into account heating by radiation from the secondary and assuming that the secondary is a point source can be calculated from the formula

$$T(r) = \sqrt[4]{T_0^4(r) + \frac{A_1 \cos\alpha}{4\pi\rho_c^2\sigma} L_2}, \qquad (14)$$

where ρ_c is the distance from the center of the area element to that of the secondary, A_1 is the coefficient for reprocessing of the incident radiation, L_2 is the bolometric luminosity of the secondary, α is the angle between the normal to the area element and the direction towards the center of the secondary, and σ is the Stefan–Boltzmann constant. The effect of heating can be more accurately calculated using the formula

$$T(r) = \sqrt{T_0^4(r) + A_1 \sum_{i=1}^{N} \frac{T_{2i} dS_{2i} \cos\alpha_i \cos\Theta_i}{\pi\rho_i^2}}, \qquad (15)$$

where T_{2i} and dS_{2i} are the temperature and area of an area element on the surface of the secondary "illuminating" the area dS_1 on the primary, α_i is the angle between the normal to the area dS_1 and the direction towards the area dS_{2i}, Θ_i is the angle between the normal to the area dS_{2i} and the direction towards dS_1, and ρ_i is the distance between the areas dS_1 and dS_{2i}. Here, the summation is carried out for those area elements on the secondary surface that are visible from the center of the area dS_1.

In this approach, there will be a temperature discontinuity in the contact region of the stars, approximately equal to the difference between the average effective temperatures of the components. As a rule, this difference is small in contact binaries, and our model calculations indicate that this temperature break does not appreciably affect the shape of the light curves. Nonetheless, the code performs a parabolic smoothing of the temperature distribution in the contact region.

To calculate the radiation of a star at different orbital phases, we introduce the fixed coordinate system (X_0, Y_0, Z_0) with its origin at the center of mass of the primary. The OX_0 and OY_0 axes are in the orbital plane, and the OZ_0 axis coincides with the OZ axis. We also introduce the relative rotation angle of the components ϑ (the angle between the OX_0 and OX axes). At orbital phase $\Psi = 0$, when the lower conjunction of the primary occurs, $\vartheta = 0$, and the OX_0 and OX axes coincide.

The coordinates of the unit vector in the direction towards the observer in the moving (X, Y, Z) coordinate frame are specified as follows:

$$\mathbf{a}_0 = (-\sin i \cos\vartheta, -\sin i \sin\vartheta, \cos i). \qquad (16)$$

Then, given the coordinates of the unit vector $\mathbf{h}$ perpendicular to the area element, the cosine of the angle between the normal to the area and the direction towards the observer can be determined from the scalar product

$$\cos\gamma = (\mathbf{a}_0, \mathbf{n}). \qquad (17)$$

Calculated parameters of two close binaries

	TU Boo (B band)					SU Sep (V band)	
	[5]		Blackbody model		Model stellar atmosphere	[6]	Blackbody model
	without a spot	with a spot	without a spot	with a spot	without a spot		
q	0.498	0.498	0.498*	0.498*	0.498*	1.0	1.0*
i, deg	87.5	88.5	87.3	87.3	86.8	81.8	82.8
T_1, K	5800	5800*	5800*	5800	5800*	12100	12100*
T_2, K	5787	5815	5735	5735	5870	10000	10420
F	1.44	1.42	1.286	1.286	1.37	1.00	1.016
R, deg	–	17	–	17	–	–	–
ϕ_0, deg	–	78	–	78	–	–	–
ψ_0, deg	–	90	–	90	–	–	–
T_f	–	0.857	–	0.875	–	–	–
$(O-C)^2$	0.0849	0.0515	0.0820	0.0614	0.0897	0.037	0.042

* Asterisks denote parameters that were fixed.

The area element is visible if $\cos\gamma > 0$ and it is not eclipsed by the secondary. The eclipse condition is tested as follows. Let the coordinates of an area element on the surface of the primary be X_1, Y_1, Z_1. The parametric equation for the straight line passing through the center of the area parallel to the line of sight has the form

$$\begin{aligned} X &= X_1 - t\sin i\cos\vartheta, \\ Y &= Y_1 - t\sin i\sin\vartheta, \\ Z &= Z_1 + t\cos i. \end{aligned} \tag{18}$$

The potential at the point (X, Y, Z) on this straight line is determined from the formula

$$\begin{aligned} \Omega^* = &\frac{1}{\sqrt{X^2+Y^2+Z^2}} \\ &+q\left(\frac{1}{\sqrt{(X-1)^2+Y^2+Z^2}} - X\right) \\ &+\frac{q+1}{2}(X^2+Y^2). \end{aligned} \tag{19}$$

The area is not eclipsed if the straight line (18) does not intersect the surface of the secondary with the potential Ω, i.e., if $\Omega^* < \Omega$ along the straight line within the close binary system.

The brightness of the secondary is calculated in the same way. The difference is that, in this case, A_2 and L_2 must be substituted into (14) and (15) instead of A_1 and L_1, and ρ_c will correspond to the distance from an area element on the secondary surface to the center of the primary. Eclipsing of the secondary by the primary is taken into account in the same way as described above.

The contributions from the two components to the total radiation of the system are summed for each phase angle ϑ, taking eclipses into account. The total radiation is then normalized to the out-of-eclipse radiation (selecting the orbital phase $\vartheta = 0.25$), and the light curve of the magnitude differences is constructed. Figures 4 and 5 present examples of synthesized light curves for contact systems.

The code also takes into account the effect of the third component (the so-called third light), if it is present in the system. The third light is added to the total radiation of the system.

Model stellar atmospheres can also be used to calculate the radiation of a system. In this case, the temperature of an area element is initially determined from (13), taking gravitational darkening into account. The mutual heating of the components is then calculated using (14) or (15). L_2 and L_1 are determined from the model atmospheres, and the intensity of the radiation emitted by an area element is obtained from tables for the model atmospheres. The input data to the tables are T, g, and $\cos\gamma$, and interpolation is done between values for these parameters. The number of parameters specifying the system's radiation increases, since the gravitational acceleration g is

given in absolute units in model-atmosphere tables. Calculation of the absolute value of g requires that the absolute values of the mass and radius of one of the components be specified. The use of model atmospheres substantially increases the calculation time.

4. MODEL WITH SPOTS ON THE STELLAR SURFACES

Many authors (see, for example, [9]) have introduced cold spots on the surfaces of the stars to explain the asymmetrical light curves of contact binaries. Let us consider a contact binary with such spots present on only one of the components. To simplify the calculations, we will assume that the surface of the star contains one circular spot. Although a real spot forms a spherical segment, our calculations have demonstrated that deviations between a plane circular spot and a spot with the shape of a spherical segment are negligibly small. The position of the spot on the surface of the star is specified by two parameters: its longitude ϕ_0 and latitude ψ_0 (Fig. 4). A complete description of the spot requires that the angular radius of the spot R and the temperature factor T_f indicating the temperature difference between the star and spot be specified. T_f is defined by the relation

$$T_f = T_{i\rho}/T_i, \qquad (20)$$

where $T_{i\rho}$ is the temperature of a given area element of the spot and T_i is the temperature of the same area on the star in the absence of the spot, taking into account limb darkening and gravitational darkening.

The input parameters for the synthesis of the theoretical monochromatic light curve are the mass ratio $q = m_2/m_1$, the degree of overfilling of the inner Roche lobe F, the effective temperatures of the components T_1 and T_2, the gravitational-darkening coefficients β_1 and β_2, the orbital inclination i, the wavelength λ, the coefficients for reprocessing of the radiation due to mutual heating of the components A_1 and A_2, and the limb-darkening coefficients u_1 and u_2. In addition, the mass m and radius R of one of the components are introduced in the calculations based on model stellar atmospheres. When a spot on one of the components is added, the spot parameters ϕ_0, ψ_0, R, and T_f are also specified.

Our code for the synthesis of theoretical light curves of close binary systems are written in FORTRAN-77. A set of multi-wavelength light curves can be calculated simultaneously. We tested the capabilities of the codes using two examples of close binaries: TU Boo (W type) and SU Sep (A type). The system parameters were obtained via an exhaustive parameter search in the vicinity of the parameter values presented in [5, 6]. The Table

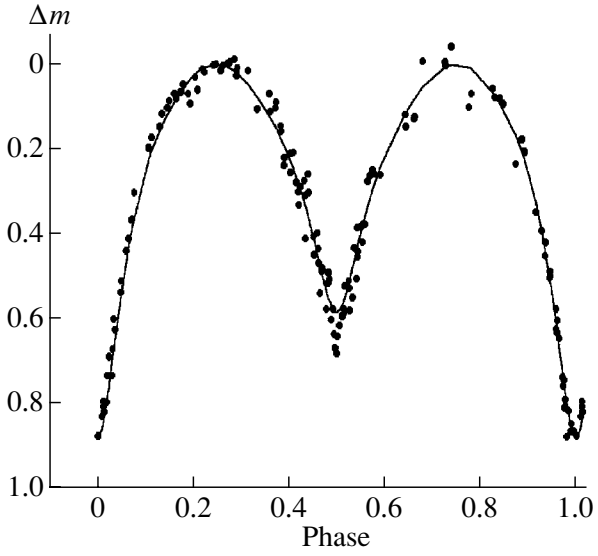

Fig. 5. Theoretical light curve of SU Sep (curve) obtained for $q = 1.0$, $i = 82°.8$, $F = 1.016$, $T_1 = 12\,100$ K, $T_2 = 10\,420$ K, and $\beta_1 = \beta_2 = 0.25$. The observations (points) are taken from [6].

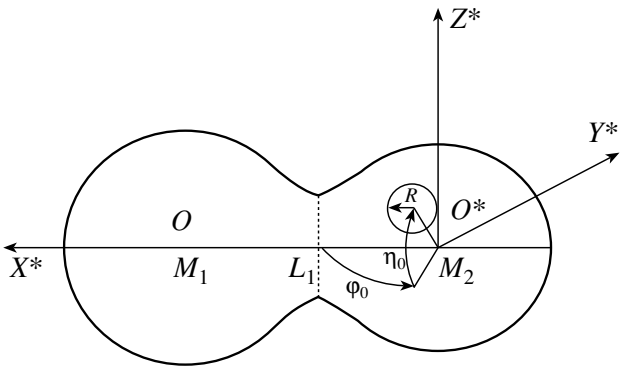

Fig. 6. Description of the position of a spot on the surface of the star. The (X^*, Y^*, Z^*) coordinate system fixed to the center of mass of the secondary is shown.

presents the results of these test calculations and a comparison with the results of other studies. It is apparent that most of the close-binary parameters obtained using our code correspond well to those obtained in other studies (within the usual range of deviations for these types of systems). The only exception is the degree of overfilling of the inner Roche lobe in TU Boo for the blackbody calculations of the system's radiation.

ACKNOWLEDGMENTS

The author thanks É.A. Antokhina for useful discussions and the permission to use her code as a basis for the developed light-curve synthesis procedure.

REFERENCES

1. R.E. Wilson and E. J. Devinney, Astrophys. J. **166**, 605 (1971).
2. G. Hill, Publ. Dom. Astrophys. Obs. **15**, 297 (1979).
3. É. A. Antokhina, Astron. Zh. **65**, 1164 (1988) [Sov. Astron. **32**, 608 (1988)].
4. N. I. Balog, A. V. Goncharskiĭ, Z. Yu. Metlitskaya, and A. M. Cherepashchuk, Perem. Zvezdy **21**, 695 (1982).
5. H. G. Niarcyos, M. Hoffmann, and H. W. Duerbeck, Astron. Astrophys., Suppl. Ser. **117**, 105 (1996).
6. Lu Meng and C. D. Skarfe, Publ. Astron. Soc. Pac. **104**, 884 (1992).
7. Z. Kopal, *Close Binary Systems* (Chapman and Hall, London, 1959).
8. S. W. Mochnacki, Astrophys. J. **300**, 304 (1986).
9. T. S. Khruzina and A. M. Cherepashchuk, Astron. Zh. **72** (2), 203 (1995) [Astron. Rep. **39**, 178 (1995)].

Translated by K. Maslennikov

Astronomy Reports, Vol. 46, No. 9, 2002, pp. 747–759. Translated from Astronomicheskiĭ Zhurnal, Vol. 79, No. 9, 2002, pp. 827–840.

Apsidal Motion in the Eclipsing Binary GG Ori

I. M. Volkov and Kh. F. Khaliullin

Sternberg Astronomical Institute, Universitetskiĭ pr. 13, Moscow, 119899 Russia

Received January 20, 2002; revised March 15, 2002

Abstract—High-precision $WBVR$ photoelectric observations of the eclipsing binary GG Ori (B9.5V + B9.5V), which has an eccentric orbit ($e = 0.22$), were carried out in 1988–2001 at the Moscow and high-altitude Tian-Shan Observatories of the Sternberg Astronomical Institute. The aim of these observations was investigation of the apsidal motion of the system. Analysis of the resulting 12-year series of observations enabled us for the first time to accurately (to within 11%) measure the rate of rotation of the orbit $\dot{\omega}_{\rm obs} = 0.046 \pm 0.005°$/yr and to appreciably improve estimates of the photometric and absolute parameters. The observed value of $\dot{\omega}_{\rm obs}$ is 28% higher than the theoretical prediction of $\dot{\omega}_{\rm th} = \dot{\omega}_{\rm cl} + \dot{\omega}_{\rm rel} = 0.036 \pm 0.001°$/yr. The relativistic part of the apsidal motion in this system $\dot{\omega}_{\rm rel}$ is a factor of 2.5 greater than the classical term $\dot{\omega}_{\rm cl}$ due to the tidal and rotational deformations of the components. The interstellar extinction in the direction of the star (at a distance of $r = 425$ pc) is very large ($A_v = 1.75^m$). A number of recently published results (in particular, the conclusion that the components of this eclipsing binary are young) are confirmed. © *2002 MAIK "Nauka/Interperiodica".*

1. INTRODUCTION

Variability of the eclipsing binary GG Ori (HD 290842 = GSC 4767.0857; $P = 6^{\rm d}.63$, $V = 10.37^{\rm m}$, Sp = B9.5V + B9.5V) was discovered by Hoffmeister [1] and later confirmed by Solov'ev [2] based on photographic observations. The correct value of the orbital period $P = 6.63^{\rm d}$ was obtained by Kordylewski [3], who also found that the secondary minimum does not occur at phase $0^p.5$, showing that the orbit of this system is eccentric ($e = 0.22$). The first photoelectric light curve of GG Ori in the $UBVR$ photometric system was published by Zakirov [4], who also determined the photometric elements of this binary using the method of Lavrov [5].

The most complete spectroscopic, photometric, and bibliographic study of this unique system was carried out recently by Torres *et al.* [6], who found the masses, absolute radii, and effective temperatures of the components and concluded that GG Ori is a young system, whose components are probably at the stage of gravitational compression preceding the main sequence. In spite of the fact that, in our opinion, the accuracy of these parameters was substantially overestimated, this fundamental study of GG Ori resolved many problems under discussion previously. However, the problem of the apsidal motion of this star has remained unsolved.

As early as 1985, Gimenez [7] included GG Ori in a list of binary systems to study the relativistic rotation of the elliptical orbit. Torres *et al.* [6] tried to estimate the rate of rotation of the orbit $\dot{\omega}_{\rm obs}$ via a combined analysis of the old photographic and visual and modern photoelectric and spectroscopic data. This yielded the estimate $\dot{\omega}_{\rm obs} = 0.034 \pm 0.014°$/yr. Unfortunately, as was emphasized by Torres *et al.*, the significance of this value was only 2.5σ. Moreover, because of the nonuniformity of the data used, such estimates are quite unreliable in general, regardless of their formal errors. We included this star in our program of photoelectric observations in 1988 precisely to investigate its apsidal motion.

2. OBSERVATIONS

The first period of our observations of GG Ori was 1988–1992. Standard differential measurements were carried out by I.M. Volkov using a $WBVR$ electrophotometer with an EMI 9863 photomultiplier mounted on the 48-cm reflector of the Tian-Shan Observatory of the Sternberg Astronomical Institute, located at an altitude of approximately 3000 m above sea level. The star C (GSC 4767.0561, $V = 9.43^m$, $B - V = 0.15^m$) was used as the primary standard, and the star K (GSC 4767.0762, $V = 8.80$, $B - V = 0.21^m$) as a secondary standard to check the calibration. All measurements were conducted with a $30''$ diaphragm. A region for measuring the background was determined before the observations based on obtaining a stable low readout on a clear moonless night. All observations were corrected for atmospheric extinction. The extinction parameters were determined for each observing time using the method of Moshkalev and Khaliullin [8]. The reference stars

1063-7729/02/4609-0747$22.00

Table 1. Photometric characteristics of GG Ori and reference stars

Star	V	$W-B$	$B-V$	$V-R$
C	9.428 ± 0.006^m	0.101 ± 0.012^m	0.152 ± 0.009^m	0.159 ± 0.009^m
K	8.803 ± 0.005	-0.326 ± 0.013	0.207 ± 0.009	0.276 ± 0.008
BD $-0°1062$	10.444 ± 0.015	–	0.471 ± 0.021	0.435 ± 0.021
GG Ori away from minima	10.371 ± 0.008	0.314 ± 0.011	0.498 ± 0.011	0.467 ± 0.010

Table 2. Depths of the minima in GG Ori

Minimum	ΔW	ΔB	ΔV	ΔR
Main	0.677 ± 0.005^m	0.682 ± 0.004^m	0.674 ± 0.003^m	0.676 ± 0.005^m
Secondary	0.658 ± 0.005	0.657 ± 0.004	0.652 ± 0.003	0.644 ± 0.005

were repeatedly compared with standard stars from the $WBVR$ catalog of 13 000 stars in the northern hemisphere [9] in the course of the observations. The results of these comparisons in the system of [9] are presented in Table 1.

The system of [9] almost coincides with the standard UBV photometric system of Johnson and Morgan in the V band. No variability in the reference stars was detected within $\pm 0.005^m$. The depths of the primary and secondary minima of the eclipsing binary system GG Ori determined from photoelectric measurements are presented in Table 2. Even a preliminary analysis of these data shows that a component whose spectrum is shifted to the blue is eclipsed in the secondary minimum. We shall consider this problem in more detail when analyzing the light curves.

A new series of observations of GG Ori aimed at measuring the rate of apsidal motion was carried out recently at the Moscow Observatory of the Sternberg Astronomical Institute using the 30-cm Carl Zeiss Jena refractor equipped with an ST-6 CCD camera and a filter realizing a photometric band close to the standard V band. Because of the limited field of view of the CCD camera, we had to employ other reference stars. The main standard was BD-$0°1062$ = GSC 4767.0727, located in the same frame as the variable. Observations of this star were repeatedly compared with those of star C, and the results are presented in Table 1. The results of individual measurements of GG Ori, corrected for atmospheric extinction and reduced to the $WBVR$ system of [9], are presented in a table that can be requested by email at the address imvsai.msu.ru. The errors of our photoelectric observations in 1988–1992 varied slightly from night to night, but did not exceed 0.005^m for most measurements in the V band. On the other hand, the CCD observations are characterized by a considerably lower accuracy, 0.019^m, and were therefore used primarily only to determine the times of minima.

3. PHYSICAL VARIABILITY OF THE COMPONENTS

When processing the measurements, we found that GG Ori experiences appreciable brightness fluctuations of $\pm 0.01^m$. These fluctuations are illustrated in Fig. 1, which shows the results of observations at the Tian-Shan Observatory on one of the nights with the highest and most stable transparency (JD 2447943). Analysis of the ratio of the brightnesses of the reference stars C and K demonstrates that GG Ori is responsible for these brightness fluctuations. Both components of GG Ori seem to be physically variable stars with characteristic periods for their brightness variations of 1–2 h. In contrast to random measurement errors, such variability imposed on the effects of eclipses can result in appreciable systematic errors in the photometric elements. This is probably one of the reasons the radii of the components determined in [4] and [6] differ by 6%, while the accuracies of the corresponding values were estimated in both papers to be about 1%. A similar situation arises in a comparison of other photometric elements presented in these two papers, which are based on different series of photoelectric measurements. The only way to decrease the systematic errors is to average a large number of the eclipsing curves. Therefore, we hoped that our long-term series of measurements would enable us to increase the accuracy of the photometric elements of this system.

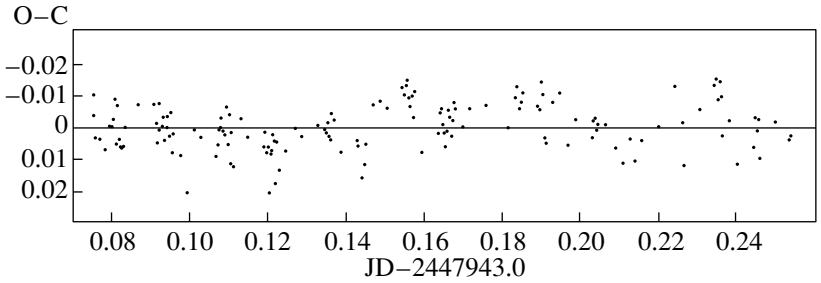

Fig. 1. Photoelectric observations of GG Ori in the V band over 4 h. Physical fluctuations of the brightness are visible.

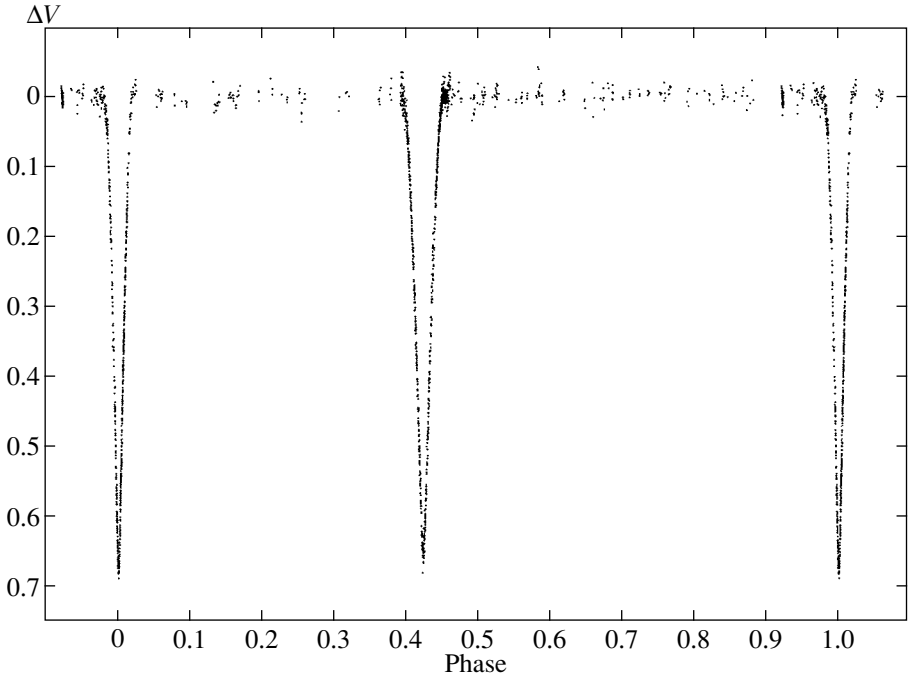

Fig. 2. Master photoelectric light curve of GG Ori in the photometric V band including observations of all authors considered.

4. PHOTOMETRIC AND ABSOLUTE ELEMENTS OF THE SYSTEM

Figure 2 presents a master light curve for GG Ori in the V band. Along with our own observations, the data of [4, 6] are included. We can see that the components are well separated, and no effects of proximity of the components are present in the light curve. Accordingly, to determine the photometric elements, we used the iterative differential-correction method developed by Khaliullina and Khaliullin [10], intended for the analysis of light curves of eclipsing systems with eccentric orbits uncorrected for the effects of reflection and the ellipsoidal shape of the components.

We first analyzed our own photomultiplier V-band measurements of GG Ori, since they are the most accurate ($\sigma_{\rm obs} = 0.006^m$) and numerous ($N = 850$). The results of an independent search for all the photometric elements using these data are presented in the usual way in the second column of Table 4. Along with the photometric elements, this table gives the following calculated parameters below the horizontal rule: the ratio of the surface brightness J_2/J_1, the ratio and sum of the component radii $k = r_2/r_1$ and $r_1 + r_2$, the luminosity of the secondary as a fraction of the total luminosity of the system $L_2 = 1 - L_1$, and the number of individual measurements N and the rms deviation of the observations from the corresponding theoretical light curve $\sigma_{\rm O-C}$. Special calculations aimed at searching for third light in the system L_3 yielded $L_3 = 0.000 \pm 0.005$. Accordingly, we assumed in all subsequent calculations that $L_2 = 1 - L_1$. The light curves in the regions of the primary and secondary minima constructed from our V observations, and the deviations O–C of the observed points from theoretical light curves corresponding

Table 3. Photometric elements of GG Ori in the V, B, and R bands obtained via a free search for all parameters

Parameter	Our observations V	Zakirov [4] V	TLCS [6] V	Master curve V	Our observations B	TLCS [6] B	Our observations R
r_1	0.0768(2)	0.0743(10)	0.0710(6)	0.0772(3)	0.0703(4)	0.0700(8)	0.0785(6)
r_2	0.0696(2)	0.0704(10)	0.0772(6)	0.0700(3)	0.0769(5)	0.0794(8)	0.0721(9)
i, deg	89.56(5)	89.37(10)	89.33(7)	89.46(5)	89.57(7)	89.20(8)	89.55(9)
e	0.2138(20)	0.2080(55)	0.2408(35)	0.2080(27)	0.2297(33)	0.2673(40)	0.2163(53)
ω, deg	123.99(38)	125.38(75)	119.59(60)	125.07(54)	121.22(65)	116.16(82)	123.39(80)
L_1	0.547(3)	0.530(11)	0.472(11)	0.542(5)	0.466(6)	0.468(7)	0.550(7)
u_1	0.32(7)	0.27(25)	0.26(16)	0.46(9)	0.10(11)	0.06(20)	0.00(26)
u_2	0.39(5)	0.72(43)	0.72(10)	0.27(25)	0.44(20)	1.00(20)	0.52(30)
L_2	0.453	0.470	0.528	0.458	0.534	0.532	0.450
J_2/J_1	1.0098	0.9728	0.9444	1.0314	0.9556	0.8836	0.9693
r_2/r_1	0.9058	0.9475	1.0873	0.9059	1.0948	1.1343	0.9187
$r_1 + r_2$	0.1464	0.1447	0.1482	0.1472	0.1472	0.1494	0.1506
N	850	226	255	1920	118	255	121
$\sigma_{\mathrm{O-C}}$	0.0085^m	0.0146^m	0.0091^m	0.0120^m	0.0049^m	0.0139^m	0.0112^m

to the refined photometric elements are presented in Figs. 3 and 4.

We performed a similar analysis for our individual measurements of GG Ori in the B and R bands, the V data of Zakirov [4], the B and V data of Torres *et al.* [6] (marked by TLCS in the table), and the master V light curve presented in Fig. 2. The results are presented in columns 3–8 of Table 3. In this and other tables, the errors of the corresponding parameters are given in parantheses in units of the last digit. In the differential-correction method, these errors are obtained along with the values of the photometric elements. Because of the nonlinear character of the light-curve analysis and the physical microvariability of the components, these errors should be treated only as formal quantities [11]. The real parameter errors are considerably higher, as can be seen from the scatter of the values for the photometric elements in table.

The following conclusions can be drawn from considering these independent series of photometric elements.

First of all, despite the high accuracy and large number of measurements, the limb-darkening coefficients of the components u_1 and u_2 cannot be determined accurately by fitting the light curves. Therefore, we decided to fix them in our subsequent calculations in accordance with their theoretical values from [12].

Second, the scatter of the independent estimates of the component radii r_1 and r_2 exceeds 10%, while the variations in $r_1 + r_2$ are considerably less. A large scatter (up to 16%) is also observed for the values of L_1 and L_2, even within the V band. Moreover, the photometric elements in this table often contradict each other. For example, the analysis of the most representative, master V light curve indicates that r_1 is 10% larger than r_2 and L_1 is 18% higher than L_2, while the surface brightness J_1 is 3% lower than J_2. The component masses are equal to within about 0.5% [6]. On the other hand, the light curve of [6] exhibits very different features: r_1 is 9% smaller than r_2, L_1 is 12% lower than L_2, and J_1 is 6% higher than J_2.

To clarify the situation, we obtained a series of solutions from the light curves for various fixed values of the ratio $k = r_2/r_1$. The corresponding results are presented in Fig. 5, which shows the dependence of $\sigma_{\mathrm{O-C}}$ on k, where $\sigma_{\mathrm{O-C}}$ is the rms deviation of the observations from the theoretical light curve for the given value of k. A comparison of the three light curves presented in the figure shows that the best solutions (corresponding to $\sigma_{\min}$) are obtained for completely different values of k. However, the values of $\sigma_{\mathrm{O-C}}$ vary only slightly in the interval $k = 0.90$–1.09. Therefore, all the light curves of GG Ori have approximately the same accuracy in this interval for

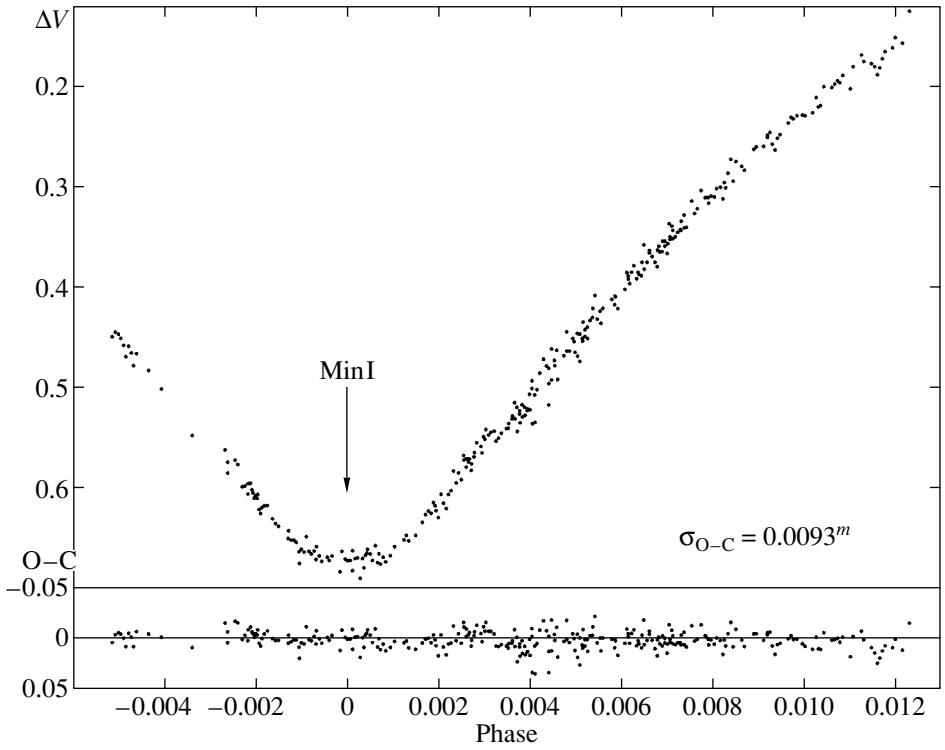

Fig. 3. Light curve of GG Ori in the V band near the primary minimum based on our photoelectric measurements in 1988–1992. The deviations O–C of the observed points from the theoretical curve corresponding to the refined photometric elements are presented below.

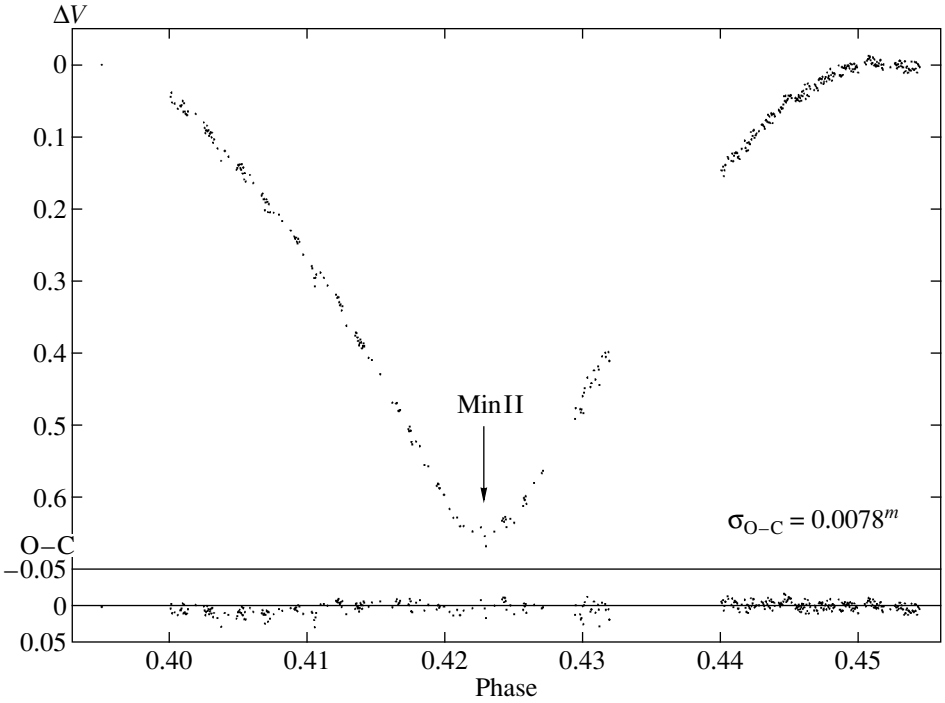

Fig. 4. Same as Fig. 3 near the secondary minimum.

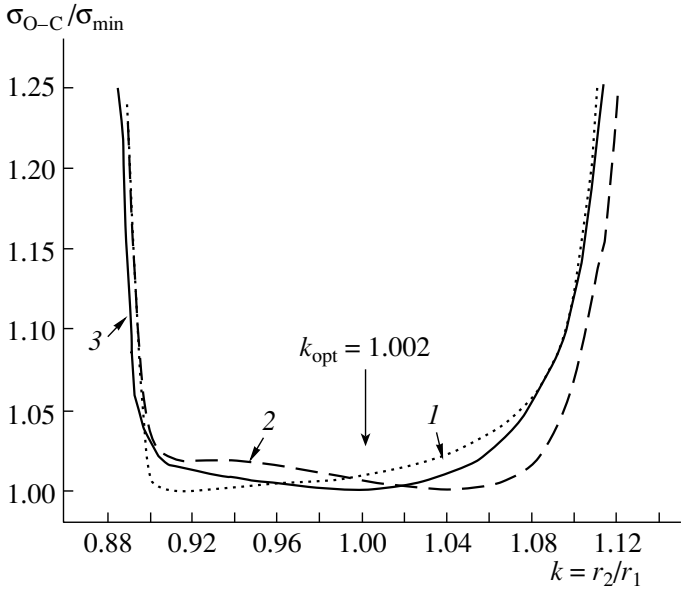

Fig. 5. Dependence of the rms deviation $\sigma_{O-C}/\sigma_{min}$ of the observations from the theoretical light curves corresponding to various fixed values of $k = r_2/r_1$ for our photoelectric observations (curve *1*), the observations of Torres *et al.* [6] (*2*), and the master curve compiled from all the published data (*3*), all in the V band.

any fixed value of k. The impossibility of determining k by fitting the light curves was already noted in [4, 6]. Thus, k must be fixed based on some additional considerations. One basis for choosing k is the approximate equality between the component masses. In fitting the light curves, we initially fixed the radii to be equal, $k = 1$. Unfortunately, this results in quite contradictory photometric elements for the master light curve: the surface brightness of the secondary turns out to be appreciably greater than the brightness of the primary, and the $W-B$ and $B-R$ color indices of the secondary are shifted to the blue relative to the indices of the primary. Therefore, we can assume that the radius of the secondary should be larger than that of the primary. In the end, we fixed the ratio of the radii to be $k = r_2/r_1 = 1.002$. This yielded a self-consistent set of solutions both for the master light curve and for our measurements in all the $WBVR$ bands.

Table 4 presents the photometric elements obtained by fitting the various light curves for fixed $k = 1.002$ and with the limb-darkening coefficients in each photometric band fixed at their theoretical values [12] for the spectral class of the components, B9.5V (see below); the structure of this table is similar to Table 3. All the results were improved by more an order of magnitude after fixing the values of k, u_1, and u_2: the scatter of r_1 and r_2 decreased from 10 to 1%, and the scatter in the relative luminosities from 16 to 0.5%. The weighted-mean geometric elements of GG Ori adopted as the final elements for all the light curves and photometric bands are given in the last (ninth) column of Table 4. Their agreement with the observations is demonstrated in Fig. 6, which presents the master V light curve near the minima, derived from all the observations, as well as the deviations O−C of the observed points from the theoretical curve constructed using these final elements. The absence of any significant systematic variations in the behavior of O−C as a function of the orbital phase demonstrates that the adopted geometric parameters adequately describe the data of all the studies considered.

Table 6 presents the relative luminosities and surface-brightness ratios of the components of GG Ori for various filters in the $WBVR$ photometric system, obtained by fitting the corresponding light curves with fixed values of u_1 and u_2, and with the geometric parameters fixed in accordance with the final elements from the ninth column of Table 4.

The absolute magnitudes and color indices for both components can be found from the information in this table together with the results of calibrating the data for GG Ori as a whole relative to standards of the $WBVR$ system, i.e., standards from the catalog [9] (Table 1). These parameters are presented in Table 6. We can see that the components have very similar photometric characteristics. However, in contrast to the conclusions of [4, 6], we find that a star with a blue excess, higher surface brightness, and greater luminosity is eclipsed in the secondary rather than the primary minimum (which is deeper according to Table 2). This surprising feature is due to the ellipticity

Table 4. Photometric elements of GG Ori for fixed $k = r_2/r_1 = 1.002$ and the theoretical limb-darkening coefficients

Parameter	Our observations V	Zakirov [4] V	TLCS [6] V	Total curve V	Our observations B	TLCS [6] B	Our observations R	Accepted values
r_1	0.07324(26)	0.07239(67)	0.07398(27)	0.07366(25)	0.07323(42)	0.07429(39)	0.07459(72)	0.07357(39)
r_2	0.07339(27)	0.07255(72)	0.07416(29)	0.07381(27)	0.07337(46)	0.07444(42)	0.07473(74)	0.07372(40)
i, deg	89.325(9)	89.375(29)	89.351(12)	89.312(11)	89.347(10)	89.276(18)	89.313(19)	89.322(15)
e	0.2176(15)	0.2061(44)	0.2277(17)	0.2144(15)	0.2264(27)	0.2402(26)	0.2223(57)	0.2184(46)
ω, deg	123.29(27)	125.69(89)	121.62(28)	123.82(29)	121.72(46)	119.66(36)	122.35(99)	123.10(90)
L_1	0.4963(17)	0.4996(48)	0.4992(19)	0.4967(18)	0.4980(29)	0.5015(27)	0.4986(67)	–
L_2	0.5037	0.5004	0.5008	0.5033	0.5020	0.4985	0.5014	–
$u_1 = u_2$	0.406	0.406	0.406	0.406	0.496	0.496	0.340	–
J_2/J_1	1.0108	0.9975	0.9982	1.0090	1.0039	0.9901	1.0019	–
$r_1 + r_2$	0.1466	0.1449	0.1481	0.1475	0.1466	0.1487	0.1493	0.1473
$\sigma_{\mathrm{O-C}}$	0.0086^m	0.0149^m	0.0093^m	0.0122^m	0.0055^m	0.0145^m	0.0115^m	–

Table 5. Relative luminosities and surface-brightness ratios of the components of GG Ori for various $WBVR$ filters

Parameter	W	B	V	R
L_1	0.4956(8)	0.4974(4)	0.4964(4)	0.4987(7)
L_2	0.5044(8)	0.5026(4)	0.5036(4)	0.5013(7)
$u_1 = u_2$	0.486	0.496	0.406	0.340
J_2/J_1	1.0136(30)	1.0065(20)	1.0105(15)	1.0011(25)
$\sigma_{\mathrm{O-C}}$	0.0260^m	0.0058^m	0.0088^m	0.0115^m

Table 6. Absolute elements of GG Ori

Parameter	Main component	Secondary component
Mass M according to [6]	$2.342 \pm 0.016 M_\odot$	$2.338 \pm 0.017 M_\odot$
Mass M adopted in this paper	$2.336 \pm 0.023 M_\odot$	$2.343 \pm 0.023 M_\odot$
Radius, R	$1.827 \pm 0.021 R_\odot$	$1.831 \pm 0.021 R_\odot$
Logarithm of luminosity, $\log L/L_\odot$	1.471 ± 0.022	1.478 ± 0.022
Effective temperature, T_{eff}	$9975 \pm 120K$	$10000 \pm 120K$
Spectral class from $WBVR$ photometry, Sp	B9.5V	B9.5V
Gravitational acceleration, $\log g$	4.283 ± 0.010	4.282 ± 0.010
Radius excess, $\Delta \log R$	0.020 ± 0.004	0.021 ± 0.004
Luminosity excess, $\Delta \log L$	0.024 ± 0.022	0.025 ± 0.022
V	11.131 ± 0.008^m	11.116 ± 0.008^m
$W-B$	0.318 ± 0.011^m	0.310 ± 0.011^m
$B-V$	0.496 ± 0.011^m	0.500 ± 0.011^m
$V-R$	0.472 ± 0.010^m	0.462 ± 0.010^m
Bolometric absolute magnitude, M_{bol}	1.01 ± 0.07^m	0.99 ± 0.07^m
Visual absolute magnitude, M_v	1.24 ± 0.07^m	1.22 ± 0.07^m
Interstellar absorption, A_v	1.75 ± 0.07^m	
Distance modulus, $(m_v - M_v - A_v)$	8.14 ± 0.10^m	
Distance to the system, d	425 ± 22 pc	
Photometric parallax, π''_{ph}	0.00235 ± 0.00012	
Age of the system, t	$(75 \pm 15) \times 10^6$ yr	

of the orbit and the deviation of the orbital inclination from 90°. The ratio of the depths of the minima will periodically change in the course of the apsidal rotation; this ratio should become inverted as the orbit rotates in the course of its evolution, so that the minimum that is the primary one at the present time will always be less deep. In general, the component masses $M_1 = 2.342(16)M_\odot$ and $M_2 = 2.338(17)M_\odot$ obtained in [6] are consistent with this picture. To obtain agreement between the photometric and spectroscopic data, we must adopt the inverse mass ratio: $M_1 = 2.336(23)M_\odot$ and $M_2 = 2.343(23)M_\odot$. These values are in nearly as good agreement with the component radial velocities presented in Tables 1 and 2 of [6] as the original values. Therefore, we also present these revised values of M_1 and M_2 in Table 6.

Figure 7 plots the components of GG Ori and the standard stars C and K in a $(W-B, B-V)$ two-color

diagram [13] in the system of [9]. The solid curve describes the behavior of main-sequence stars with their spectral classes and the unreddened positions of stars of luminosity class V indicated. The standard interstellar-absorption line [14] passing through the position of GG Ori intersects this diagram twice, near spectral classes A7V and B9.5V. Given the component masses and absolute radii (Table 6), it is natural to chose B9.5V as the spectral class for both components. We emphasize that the same conclusion can be reached using narrow-band *ubvy* photometry data [15] or the results of absolute UBV photometry of GG Ori [16].

The position of the star in the two-color diagram and its spectral and luminosity classes enables us to determine the color excess $E_{B-V} = 0.53^m \pm 0.02^m$, the total interstellar absorption $A_V = 3.3E_{B-V} = 1.75^m \pm 0.07^m$, the effective temperatures of the components $T_1 = 9975 \pm 120$ K and $T_2 = 10\,000 \pm 120$ K, and the distance to the system $d = 425 \pm 22$ pc. The mean effective temperatures of the components for their spectral class B9.5V were taken in accordance with the results of the absolute calibration presented in [17, 18]. The difference of 25 K between T_2 and T_1 follows from the ratio of the surface brightnesses of the components in the $WBVR$ bands (Table 5) and the Planck radiation law. Although the error in the absolute values of T_1 and T_2 is as large as 120 K, the difference in the temperatures $T_2 - T_1 = 25$ K is significant, since the surface-brightness ratio for the components is determined with the best accuracy by fitting the light curves. Thus, the parameters listed above can be used with known relations to find the complete set of physical and geometrical characteristics of GG Ori presented in Table 6.

The data in Table 6 along with the theoretical stellar-evolutionary models of Claret and Gimenez [19] indicate that the components of GG Ori are very young. Table 6 contains the radius excesses $\Delta \log R$ and luminosity excesses $\Delta \log L$, as well as the age of the components $t = (75 \pm 15) \times 10^6$ yr, determined assuming that these stars are on the main sequence. On the other hand, the obtained parameters of the stars do not exclude the possibility that they are only at the stage of gravitational compression before the main sequence, consistent with the conclusions of [6]. From this point of view, GG Ori is quite attractive for studies of the physical state and early evolution of the youngest stars, and especially for determining the apsidal parameters k_2. The problem of the apsidal motion of this system will be considered in more detail in the next section. We draw attention to the fact that the total interstellar absorption $A_V = 1.75^m$ ($l = 205.6°$, $b = -15.5°$) for GG Ori seems to be very large, given that the star is located at a distance of only 425 pc. Unfortunately, the spectral classes for most of the standard stars near GG Ori used in our own and earlier studies have not been determined spectroscopically. Therefore, these stars are not suitable for studying the interstellar absorption in this region. Spectral-class information is available only for star K (BD−1°.1013; B7V−IV) [20], which was used as a calibration verification source in our observations. Therefore, using the photometric characteristics of this star derived in our study (Table 1), the visual absolute magnitude $M_V = -0.4^m$ for this spectral class according to the absolute calibration of [18], and the star's position in the two-color diagram (Fig. 7), we can derive the following characteristics:

$$E_{B-V} = 0.31^m; \quad A_v = 3.3E_{B-V} = 1.02^m;$$
$$m - M = 8.18^m; \quad d = 433 \text{ pc}.$$

Therefore, this star is separated from GG Ori by only 17′ and seems to be located very close to GG Ori in space. Both stars belong to the Orion OB1 association. Therefore, it is very surprising that their A_v values are substantially different. We cannot explain this difference, and the nature of the very large interstellar absorption in the direction of GG Ori remains unclear.

5. APSIDAL MOTION

It is known [21, 23] that, due to the tidal and rotational deformation of the components, the elliptical orbit of a close binary system rotates at a rate that depends on the physical and geometrical characteristics of the system and the distribution of matter along the component radii. We shall not write here the cumbersome relations that describe this rotation; all the necessary expressions in modern notation are presented in [24]. We will call this the classical rotation, and denote its angular rate $\dot{\omega}_{\rm cl}$. In addition, even in the case of pointlike or completely rigid components, the binary orbit will rotate due to general relativistic effects [25]. We denote the rate of this rotation $\dot{\omega}_{\rm rel}$. Both these motions are in the same direction. Therefore, the expected theoretical total rotation rate should be $\dot{\omega}_{\rm th} = \dot{\omega}_{\rm cl} + \dot{\omega}_{\rm rel}$. In other words, we cannot separate these two effects and can observe only their joint action. Using the physical and geometrical characteristics of the system obtained above (Tables 4, 6) and known relations, we can calculate the expected theoretical speeds:

$$\dot{\omega}_{\rm cl} = 0.011 \pm 0.001°/\text{yr};$$
$$\dot{\omega}_{\rm rel} = 0.025 \pm 0.001°/\text{yr},$$
$$\dot{\omega}_{\rm th} = \dot{\omega}_{\rm cl} + \dot{\omega}_{\rm rel} = 0.036 \pm 0.001°/\text{yr}.$$

We can see that the expected relativistic part of the apsidal motion should be a factor of 2.5 greater than the classical part. The apsidal parameter k_2, which

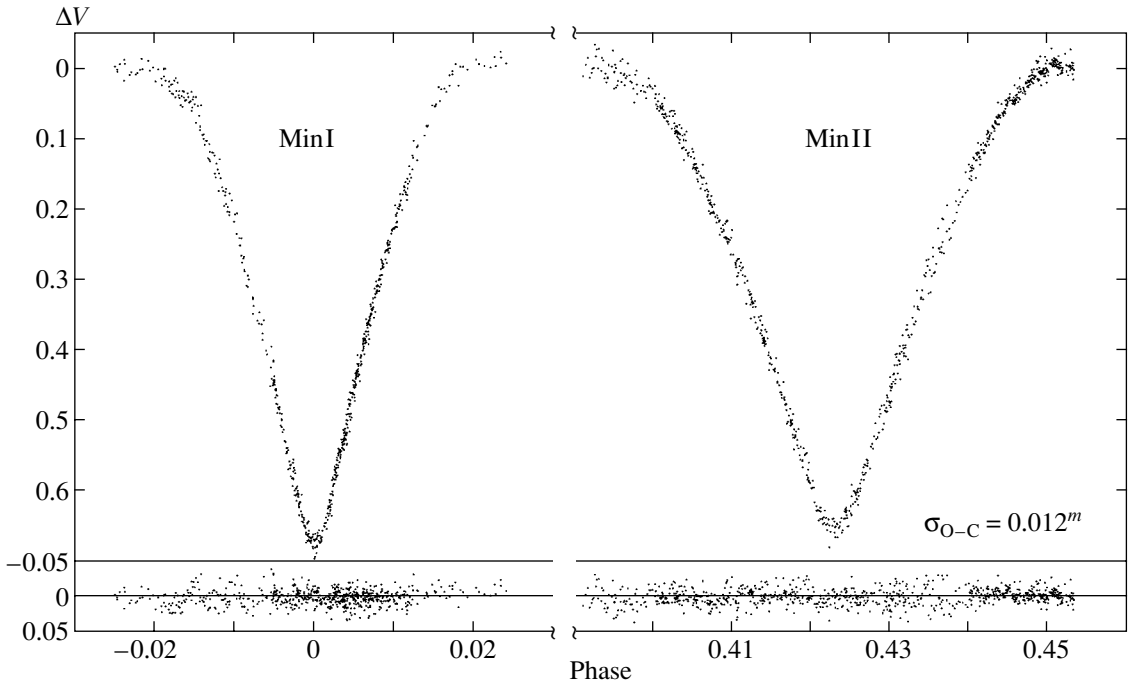

Fig. 6. Master V photoelectric light curve of GG Ori on an expanded scale near the primary and secondary minima. The O−C deviations of the observations from the theoretical light curve calculated using the photometric elements from the ninth column of Table 4 are given below.

determines the internal structure of the star and depends on its evolutionary state, was used in calculating $\dot{\omega}_{\rm cl}$. Based on the similar physical characteristics of the components, the young age of the system, and the stellar evolutionary models of Claret and Gimenez [19], we adopted $k_{2,1} = k_{2,2} = 0.0048$. This value of k_2 corresponds to a star on the main sequence with age 75×10^6 yr, solar chemical composition ($X = 0.70$, $Z = 0.02$), and mass $M = 2.34 M_\odot$.

Next, let us determine the observed rate of the apsidal motion $\dot{\omega}_{\rm obs}$ in the GG Ori system. This can be done using the relation [24]

$$\frac{P_{\rm I} - P_{\rm II}}{P} = 4e\frac{P}{U}\left(\sin\omega - e^2 \times \frac{1 + 3\sqrt{1-e^2}}{(1+\sqrt{1-e^2})^3}\sin 3\omega\right), \quad (1)$$

where P is the anomalistic orbital period of the system, $P_{\rm I}$ and $P_{\rm II}$ are the periods with which the primary and secondary minima occur, U is the period of the apsidal motion, and e and ω are the eccentricity and longitude of periastron of the orbit. To find U from this relation, we must determine the period difference $\Delta P = (P_{\rm I} - P_{\rm II})$, since all other parameters have already been found (Tables 5, 7). To determine ΔP, we collected in Table 7 all the times of both the primary and secondary minima of GG Ori recorded photoelectrically. We re-reduced all published results of individual photoelectric observations carried out by various authors using a single method to obtain a more uniform series of data. We first used the data in this table to try to describe the times of minima using a single orbital period. As a result, we obtained the following ephemerides:

$$\begin{aligned} \text{MinI} &= \text{JD}_{\rm hel}2447814.42316 \\ &\quad + 6.6314920^{\rm d}E, \\ \text{MinII} &= \text{JD}_{\rm hel}2447817.22769 \\ &\quad + 6.6314920^{\rm d}E. \end{aligned} \quad (2)$$

The deviations $(\text{O}-\text{C})_1$ of the observed times from those calculated by the ephemerides (2) are presented in the third column of Table 7. The same deviations are shown in Fig. 8 via the dependence of $(\text{O}-\text{C})_1$ on the observing epoch. This figure clearly demonstrates that Min I and Min II cannot be represented by a single period: the interval between minima changes, testifying to the rotation of the orbit. An independent description of the times Min I and Min II obtained via a least-square fit results in the ephemerides

$$\begin{aligned} \text{MinI} &= \text{JD}_{\rm hel}2447814.42316(7) \\ &\quad +6.6314975(3)^{\rm d}E, \\ \text{MinII} &= \text{JD}_{\rm hel}2447817.22769(8) \\ &\quad + 6.6314864(3)^{\rm d}E, \end{aligned} \quad (3)$$

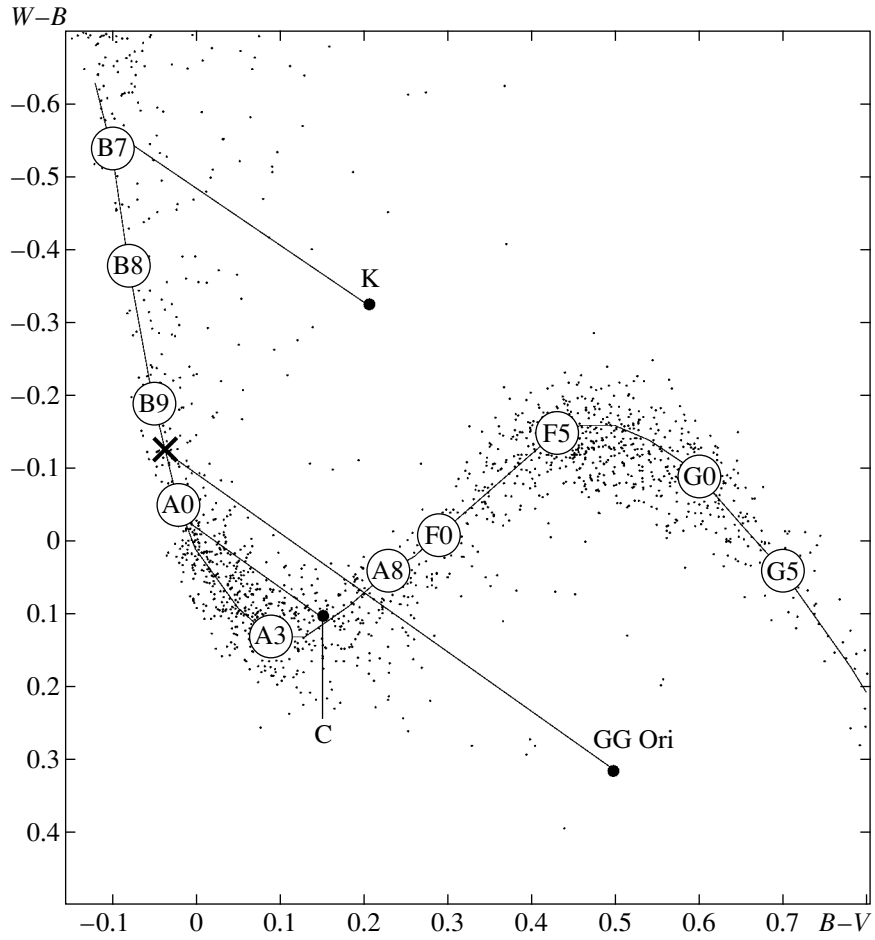

Fig. 7. Positions of the components of GG Ori and the reference stars in the ($W-B$, $B-V$) two-color diagram.

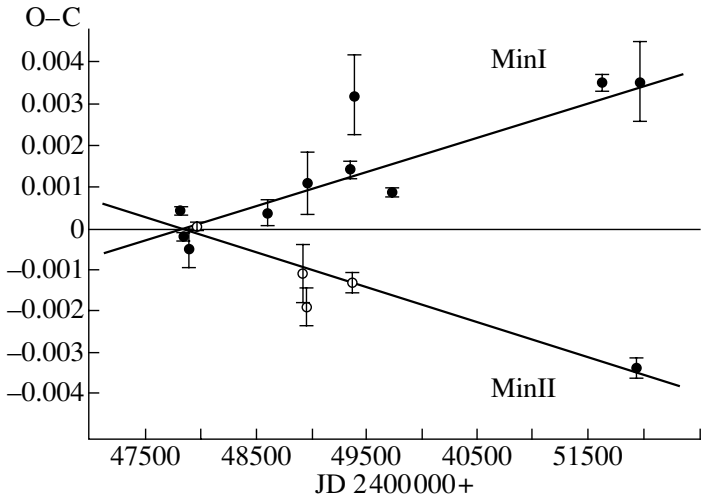

Fig. 8. Dependence of the deviations of the times Min I (filled circles) and Min II (open circles) from the linear ephemerides (2) with the same (anomalistic) period.

Table 7. Times of the primary (I) and secondary (II) minima of GG Ori from photoelectric observations and their deviations from the linear ephemerides

JD_{hel} 2400000+	Minimum	$(O-C)_1$ $P_I = P_{II} = P_a$	$(O-C)_2$ $P_I - P_{II} = 0.96^s$	Observations
47814.42361(09)	I	+0.00045	+0.00045	Torres *et al.* [6]
47834.31746(09)	I	−0.00018	−0.00019	This paper
47887.36911(50)	I	−0.00046	−0.00052	Zakirov [4]
47943.22611(11)	II	+0.00007	+0.00018	This paper
48590.30813(33)	I	+0.00041	−0.00024	Zakirov [4]
48911.42281(72)	II	−0.00106	−0.00014	Torres *et al.* [6]
48948.40941(75)	I	+0.00112	+0.00017	Zakirov [4]
48951.21094(45)	II	−0.00188	-0.00093	Zakirov [4]
49339.66777(22)	I	+0.00145	+0.00018	Torres *et al.* [6]
49355.73255(23)	II	−0.00128	+0.00001	Torres *et al.* [6]
49366.19553(96)	I	+0.00325	+0.00195	Zakirov [4]
49717.66225(11)	I	+0.00089	−0.00070	Torres *et al.* [6]
51614.27164(19)	I	+0.00357	+0.00040	This paper
51935.38090(23)	II	−0.00331	+0.00013	This paper
51952.47774(97)	I	+0.00358	+0.00012	This paper

where the errors of the elements are given in parentheses in units of the last digit. Precisely the ephemerides (3) were used to reduce the observations of all authors in all photometric bands to the single epoch JD 2447814 in order to calculate the orbital phases when fitting the light curves. The secondary minimum corresponds to phase $0^P.42291(2)$ of this epoch. The deviations $(O-C)_2$, which are similar to $(O-C)_1$ but calculated using the final ephemerides (3), are presented in the fourth column of Table 7. We can see that P_I and P_{II} differ appreciably:

$$\Delta P = P_I - P_{II} = 0.0000111(4)^d = 0.96 \pm 0.04^s.$$

Substituting the resulting values for ΔP into (1), we obtain

$$U = 7900 \pm 900 \text{ yr}; \dot{\omega}_{obs} = 360^\circ/U = 0.046 \pm 0.005^\circ/\text{yr}.$$

Thus, our analysis of a 12-year series of photoelectric measurements of GG Ori has enabled us for the first time to determine the rate of apsidal motion of the system with an accuracy of about 11%.

6. CONCLUSION

Comparison of the observed and theoretical rates of apsidal motion shows that $\dot{\omega}_{obs}$ is greater than $\dot{\omega}_{th}$ by 28%. The new information we have obtained is not sufficient for us to draw definite conclusions about the origin of this discrepancy. Deviations from the theoretical predictions have been detected in some eclipsing systems, but the observed rates of apsidal motion were always less than the predicted ones [26–28]. Thus, GG Ori has become the first system whose observed rate of apsidal motion has turned out to be appreciably greater than the theoretical one. New photoelectric observations of this system are needed to refine the values of $\dot{\omega}_{obs}$ and the photometric elements if we wish to be able to draw firmer conclusions.

In addition, it is desirable to carry out spectroscopic studies of GG Ori and neighboring stars. These observations would be useful, first, to study the nature of the extremely high interstellar absorption in the direction of GG Ori and, second, to confirm the spectral classes B9.5V of the components of this eclipsing system, which thus far have been determined only photometrically.

ACKNOWLEDGMENTS

We are grateful to N.S. Volkova for help during the observations.

REFERENCES

1. C. Hoffmeister, Astron. Nachr. **253**, 195 (1934).
2. A. Solov'ev, Astron. Tsirk. **41**, 8 (1945).
3. K. Kordylewski, Acta Astron. Ser. C **4**, 134 (1951).
4. M. M. Zakirov, Pis'ma Astron. Zh. **23**, 626 (1997) [Astron. Lett. **23**, 550 (1997)].
5. M. I. Lavrov, Tr. Kazan. Gor. Astron. Obs. **53**, 34 (1993).
6. G. Torres, C. H. S. Lacy, A. Claret, *et al.*, Astron. J. **120**, 3226 (2000).
7. A. Giménez, Astrophys. J. **297**, 405 (1985).
8. V. G. Moshkalev and Kh. F. Khaliullin, Astron. Zh. **62**, 393 (1985) [Sov. Astron. **29**, 227 (1985)].
9. V. G. Kornilov, I. M. Volkov, A. I. Zakharov, *et al.*, *WBVR Catalog of Bright Northern Stars* [in Russian] (Mosk. Gos. Univ., Moscow, 1991).
10. A. I. Khaliullina and Kh. F. Khaliullin, Astron. Zh. **61**, 393 (1984) [Sov. Astron. **28**, 228 (1984)].
11. A. V. Goncharskiĭ, A. M. Cherepashchuk, and A. G. Yagola, *Some Problems in Astrophysics* [in Russian] (Nauka, Moscow, 1985), p. 95.
12. A. A. Rubashevskiĭ, Byull. Akad. Nauk Gruz. SSR, Abastumanskaya Astrofiz. Obs. **58**, 389 (1985).
13. L. N. Kornilova, private communication (2001).
14. V. Straizys, *Multicolor Stellar Photometry* (Mokslas, Vil'nyus, 1977; Pachart Publ. House, Tucson, 1992).
15. R. W. Hilditch. and G. Hill, Mem. R. Astron. Soc. **79**, 101 (1975).
16. C. H. S. Lacy, Astron. J. **104**, 801 (1992).
17. D. M. Popper, Annu. Rev. Astron. Astrophys. **18**, 115 (1980).
18. V. Straizys, *Metal Deficit Stars* (Mokslas, Vilnius, 1982), p. 298.
19. A. Claret and A. Giménez, Astron. Astrophys., Suppl. Ser. **96**, 255 (1992).
20. W. H. Warren and J. E. Hesser, Astrophys. J., Suppl. Ser. **34**, 115 (1977).
21. H. N. Russel, Mon. Not. R. Astron. Soc. **88**, 642 (1928).
22. T. E. Sterne, Mon. Not. R. Astron. Soc. **99**, 451 (1939).
23. Z. Kopal, *Dynamics of Close Binary Systems* (Reidel, Dordrecht, 1978).
24. Kh. F. Khaliullin, in *Binary Stars,* [in Russian] Ed. by A. G. Masevich (Kosmosinform, Moscow, 1997), p. 139.
25. T. Levi-Civita, Am. J. Math. **59**, 225 (1937).
26. D. Ya. Martynov and Kh. F. Khaliullin, Astrophys. Space Sci. **71**, 147 (1980).
27. Kh. F. Khaliullin and V. S. Kozyreva, Astrophys. Space Sci. **94**, 115 (1983).
28. I. M. Volkov, Inf. Bull. Var. Stars, No. 3876 (1993).

Translated by Yu. Dumin

Astronomy Reports, Vol. 46, No. 9, 2002, pp. 760–764. Translated from Astronomicheskiĭ Zhurnal, Vol. 79, No. 9, 2002, pp. 841–846.

Abundances of Carbon, Nitrogen, Oxygen, and Other Elements in the Atmosphere of the Giant 20 Peg

T. M. Rachkovskaya

Crimean Astrophysical Observatory, Nauchnyĭ, Crimea, 98409 Ukraine

Received June 26, 2000; in final form, March 15, 2002

Abstract—We have studied the giant 20 Peg using high-resolution spectra. We derive the star's effective temperature, $T_{\rm eff} = 6970$ K, gravity, $\log g = 3.35$, and microturbulence velocity from FeI lines, $\xi_t = 2.70$ km/s, and from NiI lines, $\xi_t = 2.45$ km/s. The abundances of carbon, $\log\varepsilon(\mathrm{C}) = 8.78$, nitrogen, $\log\varepsilon(\mathrm{N}) = 8.28$, and silicon, $\log\varepsilon(\mathrm{Si}) = 7.85$, are enhanced compared to the solar values by 0.23, 0.31, and 0.30 dex, respectively. The abundances of oxygen, $\log\varepsilon(\mathrm{O}) = 8.83$, sodium, $\log\varepsilon(\mathrm{Na}) = 6.37$, and sulfur, $\log\varepsilon(\mathrm{S}) = 7.33$, are nearly solar. Calcium and nickel show normal abundances, $\log\varepsilon(\mathrm{Ca}) = 6.44$ and $\log\varepsilon(\mathrm{Ni}) = 6.32$. Iron $\log\varepsilon(\mathrm{Fe}) = 7.63$ and yttrium $\log\varepsilon(\mathrm{Y}) = 2.41$ are only slightly overabundant compared to the solar values (by 0.13 and 0.17 dex). We find a rather large (0.95 dex) overabundance of barium $\log\varepsilon(\mathrm{Ba}) = 3.08$. © *2002 MAIK "Nauka/Interperiodica".*

1. INTRODUCTION

A and F stars located near the main sequence in the Hertzsprung–Russell diagram display chemical abundance anomalies. These anomalies are especially pronounced for Ap and Am stars, and are more modest for pulsating δ Scuti stars and A–F giants. Our studies [1] of the spectra of eight δ Scuti stars showed that some displayed overabundances of all or some elements, whereas others, like classical Am stars, demonstrated enhanced calcium and scandium abundances and elemental abundances that increased with the atomic number. We paid special attention to analyses for carbon, nitrogen, and oxygen [2]—elements participating in the CNO cycle, and thus of interest in connection with stellar evolution. The abundances of these elements for δ Scuti stars were found to be close to or slightly lower than the solar values. A comparison with results for Am stars shows that, at similar effective temperatures, the mean underabundances of carbon, nitrogen, and oxygen are smaller for δ Scuti stars than for Am stars.

His detailed spectroscopic analysis of eight A–F giants led Berthet [3, 4] to conclude that their elemental abundances were similar to those of δ Scuti stars. Berthet's studies [3, 4] were based on spectroscopic observations in selected parts of the wavelength intervals $\lambda\lambda$4420-5040 Å and $\lambda\lambda$3980-4865 Å. No determinations of the C, N, and O abundances were presented in [3, 4], except for carbon abundance estimates for three stars. This stimulated our own research, aimed at supplementing existing information on the abundances of red giants with data on their C, N, and O abundances. It was also of interest to use our uniform observations to compare the abundances of these elements in the atmospheres of red giants and δ Scuti stars.

Our program included six objects of the lists [3, 4] observable at the latitude of the Crimean Astrophysical Observatory. Here, we present results for 20 Peg (HR 8392 = HD 209166, $m_v = 5.59$, Sp F3III); this star differs from the rest of our selected stars primarily in its low rotational velocity, $v \sin i \leq 20$ km/s, and the fact that most of its spectral lines are unblended or only partially blended, making it possible to reliably estimate their equivalent widths. Because our greatest interest was in C, N, and O, the observed spectral intervals were centered on the CI λ5052, NI λ8683, and OI λ6156 lines. The selected spectral intervals also contain lines of other elements, whose abundances we estimated as well. In addition, we observed the H_α, H_β, and H_γ lines and used their equivalent widths when constructing a model atmosphere for 20 Peg. As a result, along with carbon, nitrogen, and oxygen, we have also obtained the first sodium, silicon, and sulfur abundances for 20 Peg.

2. OBSERVATIONS

Our observations were acquired with the 2.6 m reflector of the Crimean Astrophysical Observatory using an American-made EEV15-11 CCD array (1024×256 pixels) in September–October, 1995 and in January and October, 1999. The CCD was mounted at the Coudé focus. We observed in the second order of the diffraction grating, and the observations covered about 70 Å width. The H_α region

1063-7729/02/4609-0760$22.00

was observed in the first order as well, recording an interval of approximately 120 Å. In the first case, the reciprocal linear dispersion of the spectra was 3 Å/mm and, in the second case, 6 Å/mm. The spectroscopic resolution was 30 000, and the signal-to-noise ratio was $S/N = 80$–150. The spectra were reduced using standard techniques: dark current elimination, flat-fielding, removal of chance cosmic-ray traces, correction for the night-sky background, and normalization to the continuum. The wavelength calibration was performed using thorium and argon lines of a comparison spectrum.

3. EQUIVALENT WIDTHS. OSCILLATOR STRENGTHS

The list of the studied lines is presented in Table 1. The columns contain for various elements line wavelengths λ, excitation potentials of the ground level χ, oscillator strengths $\log gf$, and equivalent widths W_λ and abundances $\log\varepsilon$ derived from individual lines. We identified lines in the spectrum of 20 Peg using lists from the Vienna database [5] and our previous papers (for example, see [2]). The values of χ and $\log gf$ were also taken from [5] for all lines of all elements, except for three silicon lines, SiI λ6142, λ6145, and λ6155, for which we used the oscillator strengths from [6]. Since the oscillator strengths for the CI and NI lines from [5] differ somewhat from those we used in our study of δ Scuti stars [2], we decided to compute $\log\varepsilon$(C) and $\log\varepsilon$(N) for the old values of $\log gf$ as well. These results are given in parantheses in Table 1. In our equivalent-width computations, the line profiles were assumed to be Gaussian.

4. ATMOSPHERIC PARAMETERS

We analyzed the atmosphere of 20 Peg using Kurucz models [7]. A detailed description of the analysis techniques, based on a comparison between the observed and model characteristics, can be found in [8].

EFFECTIVE TEMPERATURE AND GRAVITY. When comparing our observations to the theoretical data, we used the following criteria: (1) the H_α, H_β, and H_γ equivalent widths W_λ; (2) the ionization equilibrium for iron; (3) the photometric index $[c_1] = c_1 - 0.2(b-y) = 0.691$ of the four-band $ubvy$ system, known to be extinction independent; (4) the photometric index β. As noted above, the theoretical data are given by Kurucz [7]. We derived the observed H_α, H_β, and H_γ equivalent widths. The values of c_1 and $(b-y)$, needed to compute $[c_1]$, and the index $\beta = 2.704$ were taken from Hauck and Mermilliod [9].

Let us consider the determination of the hydrogen-line equivalent widths. In our observations of the H_β and H_γ lines, we were not able to simultaneously record the entire spectral interval corresponding to the neighborhood of the line wings, needed to trace the continuum as well as the wings themselves. Therefore, we observed overlapping intervals of the lines and then joined them. Nevertheless, because of the presence of strong blending and the considerable width of the wings, we could not be sure that the established continuum level was correct. Therefore, we proceeded as follows. We first measured the W_λ values for "truncated" hydrogen-line profiles, i.e., relative to the continuum derived from two points $\Delta\lambda$ in the wings, at comparatively small separations from the line center: ±30 Å for H_α and H_γ and ±32 Å for H_β. The points used to trace the continuum must correspond to unblended parts of the wings. We then reduced the W_λ values thus determined for the truncated profiles to the line equivalent widths for wing widths of ±100 Å using coefficients derived from the theoretical profiles of Kurucz [7]. Table 2 presents the hydrogen-line W_λ values for various continuum levels. From the first-order spectrum for H_α, when the entire profile and the adjacent continuum were recorded simultaneously, we could directly integrate the profile and estimate the H_α equivalent width. The H_α equivalent widths derived using the two methods differ by no more than 5%. Note that we had three independent observations for different seasons for H_β and two independent observations for each of H_α and H_γ.

The values $T_{\rm eff} = 6970 \pm 80$ K and $\log g = 3.35 \pm 0.18$ were found by averaging the parameters corresponding to crossing points of the β, H_α, H_β, and H_γ curves with each of the $[c_1]$ and Fe curves in Fig. 1. The dot in the figure designates the adopted model, which is close to that obtained earlier by Berthet [4]:

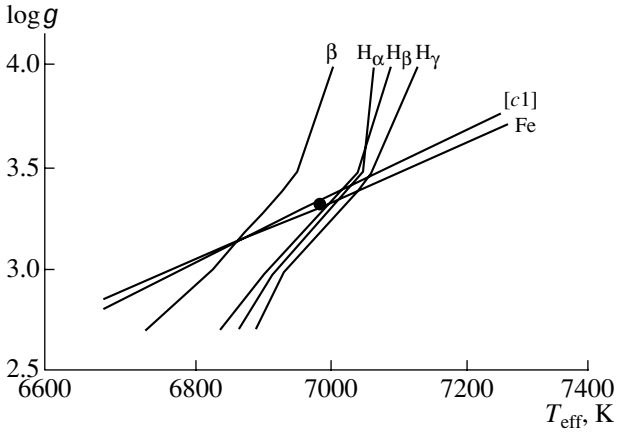

Fig. 1. Diagram used to determine the effective temperature and gravity of 20 Peg. The dot corresponds to the adopted model.

Table 1. Lines studied in the spectrum of 20 Peg

Element λ, Å	χ, eV	$\log gf$	W_λ, mÅ	$\log \varepsilon$	Element λ, Å	χ, eV	$\log gf$	W_λ, mÅ	$\log \varepsilon$
CI					5051.64	0.92	−2.80	114	7.78
5052.17	7.68	−1.65	92	8.78	5054.64	3.64	−1.92	20	7.69
		(−1.49)		(8.53)	5057.50	4.19	−1.56	14	7.57
NI					5067.15	4.22	−0.97	48	7.73
8680.29	10.34	+0.35	115	8.55	5068.77	2.94	−1.04	108	7.62
		(+0.40)		(8.50)	5072.67	4.22	−1.22	43	7.89
8683.40	10.33	−0.21	39	8.11	5074.75	4.22	−0.20	106	7.80
		(+0.14)		(7.75)	5076.26	4.30	−0.77	50	7.63
8686.15	10.33	−0.30	38	8.18	5079.74	0.99	−3.22	76	7.71
		(−0.27)		(8.15)	5083.34	0.96	−2.96	82	7.50
OI					6136.62	2.45	−1.40	117	7.63
6155.98	10.74	−0.70	20	8.92	6137.69	2.59	−1.40	100	7.50
6156.76	10.74	−0.48	21	8.73	6151.62	2.18	−3.30	11	7.57
6158.19	10.74	−0.34	30	8.83	6157.72	4.08	−1.26	34	7.68
NaI					6165.36	4.14	−1.55	17	7.64
6154.23	2.10	−1.56	14	6.38	6170.50	4.80	−0.65	42	7.77
6160.75	2.10	−1.26	18	6.36	6173.34	2.22	−2.88	26	7.63
SiI					6180.20	2.73	−2.59	16	7.48
6142.48	5.62	−1.56	25	7.85	6187.99	3.94	−1.72	17	7.65
6145.01	5.62	−1.48	18	7.60	6191.56	2.43	−1.42	116	7.62
6155.13	5.62	−0.84	55	7.63	7780.55	4.47	−0.27	82	7.62
7760.63	6.21	−1.56	16	8.06	7807.95	4.99	−0.70	27	7.69
7799.18	6.18	−1.11	37	8.07	8674.75	2.83	−1.80	62	7.38
8686.35	6.20	−1.20	38	8.04	8688.63	2.18	−1.21	179	7.68
SiII					8699.45	4.95	−0.38	43	7.45
5055.98	10.07	+0.59	57	7.69	8710.39	4.91	−0.65	52	7.81
SI					FeII				
6175.84	8.05	−1.09	33	7.99	5036.92	2.83	−4.52	12	7.20
8671.28	7.87	−0.64	28	7.13	6147.74	3.89	−2.72	84	7.50
8679.62	7.87	−0.41	62	7.43	6149.26	3.89	−2.92	76	7.60
8680.41	7.87	−0.21	39	6.91	6150.10	3.22	−4.75	8	7.55
8693.14	7.87	−1.37	4	6.93	6175.15	6.22	−1.98	33	7.91
8694.63	7.87	+0.08	119	7.62	6179.38	5.57	−2.81	13	7.73
CaI					8671.88	6.14	−2.79	6	7.67
6161.30	2.52	−1.02	41	6.40	NiI				
6162.17	1.90	+0.10	188	6.82	5035.36	3.64	+0.29	96	6.30
6166.44	2.52	−0.90	42	6.30	5035.96	3.66	−0.23	64	6.37
6169.05	2.52	−0.55	70	6.33	5038.59	3.83	−0.22	60	6.45
6169.56	2.53	−0.27	93	6.37	5048.84	3.85	−0.38	38	6.31
TiI					5080.53	3.66	+0.33	97	6.29
5036.46	1.44	+0.13	41	5.22	5081.11	3.85	+0.30	82	6.25
5038.40	1.43	+0.01	60	5.61	5082.34	3.66	−0.54	34	6.25
5039.96	0.02	−1.13	47	5.41	5084.09	3.68	+0.03	76	6.30
FeI					6176.81	4.09	−0.26	30	6.23
5027.76	4.21	−1.25	32	7.75	6186.71	4.10	−0.96	10	6.36
5028.13	3.57	−1.12	68	7.63	7788.94	1.95	−2.42	24	6.47
5029.62	3.42	−2.05	14	7.44	7797.59	3.90	−0.26	48	6.29
5041.85	4.28	−0.82	48	7.63	YII				
5044.21	2.85	−2.04	36	7.52	5087.42	1.08	−0.17	94	2.41
5048.44	3.96	−1.03	58	7.72	BaII				
5049.82	2.28	−1.36	120	7.59	6141.71	0.70	−0.08	201	3.08

$T_{\rm eff} = 7000$ K, $\log g = 3.3$. The quoted uncertainties of $T_{\rm eff}$ and $\log g$ are formal.

MICROTURBULENCE VELOCITY. The microturbulence velocity, ξ_t, can be determined by requiring that the abundances derived from the lines of an ion not vary systematically with increasing equivalent width. The lines must be sufficiently numerous and their equivalent widths must cover a sufficient range. Among the lines observed by us in the spectrum of 20 Peg, the lines of neutral iron, FeI, were the most numerous (33 lines). In addition, we used lines of nickel, NiI, to estimate ξ_t, though only 12 such lines were observed. Applying our model, we computed the abundances of iron, $\log\varepsilon$(Fe), and of nickel, $\log\varepsilon$(Ni), for several ξ_t values. It appeared that there was no correlation between $\log\varepsilon$ and W_λ in the case of $\xi_t = 2.45$ km/s for NiI and $\xi_t = 2.70$ km/s for FeI (see Fig. 2, where the abundances are plotted versus the equivalent widths). Here, the formal uncertainties do not exceed ± 0.05 km/s. We finally adopted the value $\xi_t = 2.65$ km/s for our abundance computations. Note that Berthet [4] derived a lower microturbulence velocity, $\xi_t = 1.5$ km/s, from FeI lines in the blue.

5. CHEMICAL ABUNDANCES

The elemental abundances, $\log\varepsilon$(El), in the atmosphere of 20 Peg were determined using the parameters $T_{\rm eff} = 6970$ K, $\log g = 3.35$, and $\xi_t = 2.65$ km/s, assuming local thermodynamic equilibrium. Our abundance estimates from individual lines, $\log\varepsilon(\mathrm{El}) = \log[N(\mathrm{El})/N(\mathrm{H})] + 12$ (on this scale, the hydrogen abundance is $\log\varepsilon(\mathrm{H}) = 12$), are presented in the last column of Table 1. The average abundances for each ion are given in the second column of Table 3, followed in parantheses by the numbers of lines used to compute the average $\log\varepsilon$(El) value. Recall that the $\log\varepsilon$ values for carbon and nitrogen derived with the old oscillator strengths are also given in parantheses. The third column contains the values of σ, the rms deviation from the mean abundance. The fourth column gives $[X] = [\log\varepsilon(\mathrm{El})_* - \log\varepsilon(\mathrm{El})]_\odot$ abundances in the atmosphere of 20 Peg relative to the Sun [10], with weighted mean $\log\varepsilon$ values used for 20 Peg when elements were observed in several ionization states. Finally, the last column compares the abundances of the elements in common for this study and the study of Berthet [4] in the atmosphere of 20 Peg, $\Delta\log\varepsilon = [\log\varepsilon(\mathrm{El}) - \log\varepsilon(\mathrm{Fe})]_{\rm author} - [\log\varepsilon(\mathrm{El}) - \log\varepsilon(\mathrm{Fe})]_{[4]}$; to eliminate the influence of errors in the atmospheric parameters, the abundances are considered relative to the abundance of iron, which is determined with the most certainty.

Table 3 leads to the following conclusions. The atmospheric carbon abundances of 20 Peg, $\log\varepsilon$(C), for the two oscillator strengths derived from the CI λ5052 line are within 0.02–0.23 dex of the solar value; i.e., it is slightly higher than or equal to the solar value. An overabundance of nitrogen by 0.16–0.30 dex is observed. Our results show near-solar abundances for oxygen, sodium, sulfur, calcium, and nickel. The abundances of iron and yttrium were enhanced by 0.13 and 0.17 dex, respectively, relative to the solar values. We can probably be certain that there are overabundances of silicon by 0.30 dex, of titanium by 0.40 dex, and barium by 0.95 dex, although the barium abundance, like those of yttrium and carbon, is based on a single line.

Comparison of our estimates with those of Berthet [4] (the last column of Table 3) shows that both studies yielded similar abundances for calcium, nickel, and, probably, titanium. In the case of titanium, the abundance we derived from lines of the neutral titanium, TiI ($\log\varepsilon(\mathrm{Ti}) = 5.42$), is close to the value

Table 2. Equivalent widths of the hydrogen lines

Line	$\Delta\lambda$, Å	W_λ, Å	No. of observations
H_α	±30	6.01 ± 0.20	2
	±100	7.63	
H_β	±32	7.53 ± 0.18	3
	±100	9.38	
H_γ	±30	8.19 ± 0.44	2
	±100	10.14	

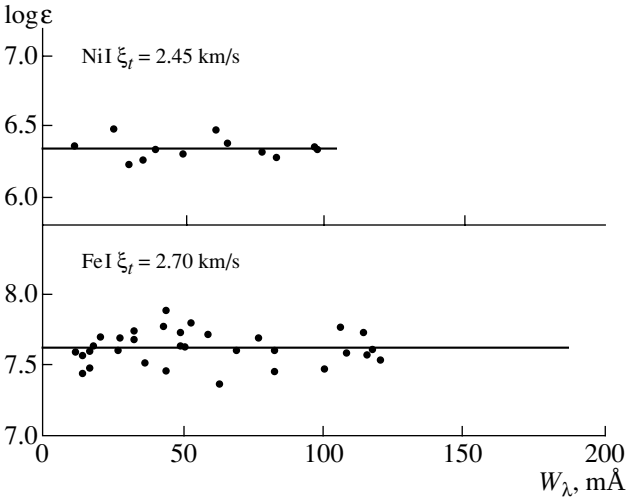

Fig. 2. Abundances derived from the NiI and FeI lines as a function of equivalent width, for $\xi_t = 2.45$ km/s and $\xi_t = 2.70$ km/s.

Table 3. Elemental abundances in the atmosphere of 20 Peg

Element	$\log\varepsilon$	σ	[X]	$\Delta\log\varepsilon$(El)
CI	8.78(1)	–	+0.23	
	(8.53)		(−0.02)	
NI	8.28(3)	0.24	+0.31	
	(8.13)		(+0.16)	
OI	8.83(3)	0.10	−0.04	
NaI	6.37(2)	0.00	+0.04	
SiI	7.88(6)	0.22		
SiII	7.69(1)			
	7.85(7)		+0.30	
SI	7.33(6)	0.42	0.00	
CaI	6.44(5)	0.21	+0.08	−0.02
TiI	5.42(3)	0.20	+0.40	+0.47 (+0.10)
FeI	7.64(33)	0.12		
FeII	7.60(7)	0.22		
	7.63(40)		+0.13	
NiI	6.32(12)	0.08	+0.07	+0.07
YII	2.41(1)		+0.17	−0.42
BaII	3.08(1)		+0.95	+0.66

obtained by Berthet from lines of ionized titanium, TiII ($\log\varepsilon(\mathrm{Ti}) = 5.47$), whereas Berthet's value for TiI lines is lower, $\log\varepsilon(\mathrm{Ti}) = 5.10$. Table 3 shows that our estimates differ from those of Berthet most strongly for yttrium and barium. It is difficult to identify the origin of this discrepancy at this time. We can note only that our abundances for each of these elements were based on a single line, whereas Berthet observed three yttrium lines and two barium lines. Nevertheless, we believe that the most likely explanation of the discrepancy is the different oscillator strengths used.

We conclude that the C, N, and O abundances for 20 Peg are either near-solar or slightly overabundant, whereas we observed [2] either near-solar abundances or underabundances of these elements for δ Scuti stars. This suggests that A–F stars gradually lose the elemental abundance peculiarities of Am stars.

6. CONCLUSIONS

The main results of our study of 20 Peg follow.

We have estimated the star's atmospheric parameters: its effective temperature $T_{\mathrm{eff}} = 6970 \pm 80$ K, gravity $\log g = 3.35 \pm 0.18$, and microturbulence velocity $\xi_t = 2.70 \pm 0.05$ km/s from FeI lines and $\xi_t = 2.45 \pm 0.05$ km/s from NiI lines. We adopted $\xi_t = 2.65$ km/s in our analysis.

We have determined the abundances of carbon, nitrogen, oxygen, sodium, silicon, and sulfur for 20 Peg for the first time. The abundances of carbon, $\log\varepsilon(\mathrm{C}) = 8.78$, and of nitrogen, $\log\varepsilon(\mathrm{N}) = 8.28$, are not lower than the solar values, and the abundances of oxygen, $\log\varepsilon(\mathrm{O}) = 8.83$, sodium, $\log\varepsilon(\mathrm{Na}) = 6.37$, and sulfur, $\log\varepsilon(\mathrm{S}) = 7.33$, likewise do not differ from the solar abundances. The δ Scuti stars studied in our earlier paper [2] demonstrated either normal abundances or underabundances of C, N, and O.

The following can be concluded about the abundances of other elements. The abundances of calcium, $\log\varepsilon(\mathrm{Ca}) = 6.44$, and nickel, $\log\varepsilon(\mathrm{Ni}) = 6.32$, are nearly solar, whereas iron and yttrium are slightly overabundant, $\log\varepsilon(\mathrm{Fe}) = 7.63$ (0.13 dex) and $\log\varepsilon(\mathrm{Y}) = 2.41$ (0.17 dex). The abundances of silicon, $\log\varepsilon(\mathrm{Si}) = 7.85$, and titanium, $\log\varepsilon(\mathrm{Ti}) = 5.42$, are enhanced in the atmosphere of 20 Peg by 0.30 and 0.40 dex, respectively, and the greatest overabundance (up to 0.95 dex) is observed for barium ($\log\varepsilon(\mathrm{Ba}) = 3.08$).

REFERENCES

1. T. M. Rachkovskaya, Izv. Krym. Astrofiz. Obs. **80**, 3 (1988).
2. T. M. Rachkovskaya, Astron. Zh. **77**, 264 (2000) [Astron. Rep. **44**, 227 (2000)].
3. S. Berthet, Astron. Astrophys. **227**, 156 (1990).
4. S. Berthet, Astron. Astrophys. **251**, 171 (1991).
5. N. E. Piskunov, F. Kupka, T. A. Ryabchikova, *et al.*, Astron. Astrophys., Suppl. Ser. **112**, 525 (1995).
6. F. Thevenin, Astron. Astrophys., Suppl. Ser. **82**, 179 (1990).
7. R. L. Kurucz, CD-Rom No. 13 (1993).
8. L. S. Lyubimkov, *Chemical Composition of Stars: Method and Results of Analysis* [in Russian] (Astroprint, Odessa, 1995).
9. B. Hauck and M. Mermilliod, Astron. Astrophys., Suppl. Ser. **129**, 431 (1998).
10. N. Grevesse and A. Noels, Astron. Soc. Pac. Conf. Ser. **99**, 118 (1996).

Translated by N. Samus'

Astronomy Reports, Vol. 46, No. 9, 2002, pp. 765–778. Translated from Astronomicheskiĭ Zhurnal, Vol. 79, No. 9, 2002, pp. 847–861.

Evolution of Close Stellar Binaries with Black Holes under the Action of Gravitational Radiation and Magnetic and Induced Stellar Winds of the Donor

A. V. Tutukov and A. V. Fedorova

Institute of Astronomy, Russian Academy of Sciences, ul. Pyatnitskaya 48, Moscow, 109017 Russia

Received December 15, 2001; revised February 1, 2002

Abstract—We show that semi-detached close binary systems with massive ($4-25M_\odot$) black holes are formed in the evolution of massive stellar binaries in which the initial mass of the primary exceeds $\sim 25M_\odot$. The mass exchange in such systems is maintained by the nuclear evolution of the donor and by its magnetic and induced stellar winds. The donor in such systems can be a main-sequence star, subgiant, non-degenerate helium star, or white dwarf. The evolution of corresponding systems with black-hole masses of $10M_\odot$ is investigated. © *2002 MAIK "Nauka/Interperiodica".*

1. INTRODUCTION

The evolution of X-ray binaries with low-mass donors was studied in detail in our earlier paper [1], where we took the accreting component to be a neutron star. The driving forces behind the evolution of these systems were the nuclear evolution and magnetic stellar wind (MSW) of the donor, gravitational-wave radiation (GWR), and the induced stellar wind (ISW) of the donor due to its irradiation by hard radiation during periods of accretion. This numerical modeling of the evolution of low-mass X-ray binaries with neutron stars enabled us to understand their distribution of orbital periods and the X-ray luminosities of the accreting stars.

The induced stellar winds of the donors can explain the overall flux of X-rays from Galactic low-mass close binaries. The rate of their formation in the Galaxy is $\sim (1-6) \times 10^{-6}$ per year [2]. A typical initial mass for the donor is $\sim 1\ M_\odot$, and about 10% of the donor mass is accreted during the evolution of the neutron star [1]. The resulting Galactic X-ray flux from low-mass X-ray binaries with total accretion rates of $\sim (1-6) \times 10^{-7}\ M_\odot$/yr should be $\sim (1-6) \times 10^{39}$ erg/s. The observed X-ray fluxes from these systems are $\sim (2-3) \times 10^{39}$ erg/s [3]. Thus, introducing an induced stellar wind makes it possible to obtain agreement between the observed and theoretical X-ray fluxes of binaries in our own Galaxy, and probably in M31 as well [4]. Supposing an accretion efficiency of 10% enables us to explain the observed rotational periods of accreting neutron stars in low-mass X-ray binaries as well [5].

It is interesting that applying the same logic to massive X-ray binaries with integrated X-ray luminosities of $\sim (2-3) \times 10^{38}$ erg/s [3] and total mass-exchange rates of $\sim 5 \times 10^{-8}\ M_\odot$/yr implies a low efficiency for the accretion in these systems, $\sim 10^{-6}$. This follows from the theoretical rate of their formation, $\sim 3 \times 10^{-3}$ per year, and the typical donor mass, $\sim 10\ M_\odot$ [3]. It is clear that induced stellar winds cannot explain such a low efficiency for the transformation of the energy of the accreted matter of the donor into X-ray radiation. Only the formation of common envelopes that limit the life times of bright, massive X-ray sources to several thousand years is able to explain such low efficiencies for the mass exchange between the components of such systems.

Analyses of observational data for X-ray binaries in our Galaxy have shown that some of these sources have X-ray luminosities reaching $\sim 10^{39}$ erg/s; i.e., they have accretion rates of $\dot{M}_{\rm acc} \approx 10^{-7}\ M_\odot$/yr [1, 6], which exceeds the limiting accretion rate for neutron stars by about an order of magnitude. Such high accretion rates are also observed in X-ray binaries in some nearby galaxies, such as the Antennae, M82, NGC 1808, NGC 6240, and NGC 7331 [7]. It is clear that this is the result of the accretion of the donor material by black holes with masses $5-10\ M_\odot$ [8]. Many of these systems have main-sequence (MS) stars with masses less than the solar mass as donors, and the orbital periods of these systems are in the interval 0.17–0.52 days. This last circumstance admits the possibility of the active participation of the magnetic stellar wind of the donor in the evolution of these systems. Examples of such systems include V616 Mon, QZ Vul, MM Vel, GU Mus [8], and XTE J1118+480 [9]. The orbital periods of some X-ray binaries reach ~ 6.5 days, as in V404 Cyg [8].

1063-7729/02/4609-0765$22.00

The donors of these systems are evolved, low-mass stars. Finally, the donor in a system with a black hole can be a non-degenerate helium star or degenerate, low-mass white dwarf. As shown in [1], in this latter case, it is possible to obtain systems with orbital periods down to ~ 10 min. Our aim in the current study is to obtain and analyze numerical simulations of all such systems.

2. CONDITIONS FOR THE FORMATION OF X-RAY BINARIES WITH BLACK-HOLE ACCRETORS AND LOW-MASS DONORS

Estimates of the masses of black holes in observed X-ray binaries fall in the range $\sim 4\ M_\odot$(MM Vel)$\div$ $\sim 16\ M_\odot$ (Cyg X-1) [8]. The upper bound of black-hole masses for systems with low-mass donors does not exceed $\sim 13\ M_\odot$ (V404 Cyg). If we take the mass of the helium remnant of the initially massive component to be $0.1(M_{10}/M_\odot)^{1.4}$ [10] and the mass of the secondary to be $\sim M_\odot$, the condition for the system to survive the primary's supernova explosion has the form

$$\frac{M_{10}}{M_\odot} \lesssim 5.1\left(2\frac{M_{BH}}{M_\odot}+1\right)^{0.71}, \qquad (1)$$

where M_{BH} is the mass of the black hole that is formed. The known limits for the observed masses in X-ray binaries with black holes indicated above can be used to estimate the minimum initial masses of the primaries in close binary systems that produce black holes as the end products of their evolution: $25\ M_\odot$. Note that similar estimates were obtained in [11] based on computations of stellar core collapse and the evolution of binary stars. Stars with lower initial masses (10–$25\ M_\odot$) produce neutron stars. Stars with initial masses $\gtrsim 50\ M_\odot$ do not expand due to the intense loss of matter via their stellar winds [12]. Therefore, common envelopes do not form in systems containing such massive stars, and these systems do not become sufficiently close for gravitational radiation and the magnetic stellar wind to lead to the secondary filling its Roche lobe.

Let us consider in more detail the condition for the formation of X-ray binaries in which the accretor is a black hole and the donor is a low-mass ($\sim M_\odot$) MS star [10]. We also admit the possibility that the donor could be a non-degenerate helium star with a mass of 0.4–$1\ M_\odot$ or a degenerate dwarf with a mass of 0.1–$0.5\ M_\odot$. Due to the large initial component-mass ratio, such systems unavoidably pass through a common-envelope stage after depletion of the hydrogen in the core of the primary and its expansion. The dispersal of the common envelope causes the components to approach, and the helium core of the star collapses, forming a black hole. If condition (1) is satisfied, the system survives this process. The further evolution of the system depends on the semi-major axis at the time of the explosion and the mass of the secondary, i.e., the potential donor.

Let us first consider a system with a MS donor (Fig. 1a). If the donor is fully convective (i.e., if its mass is less than $\sim 0.3\ M_\odot$), the only driving force for the evolution of the system is the radiation of gravitational waves [13]. The absence of a magnetic stellar wind in MS stars with masses lower than $\sim 0.3\ M_\odot$ (and spectral types later than M3) is confirmed by the rapid rotation of these stars [14, 15]. The upper limit for the semi-major axes of systems that are able to become semi-detached over the Hubble time is given by the condition that the characteristic time scale for the radiation of gravitational energy by the system $\tau_{\rm GWR}$ be equal to the Hubble time $\tau_{\rm H}$. The Hubble time is estimated to be 1.5×10^{10} yrs, and $\tau_{\rm GWR}$ is given by the formula [16]:

$$\tau_{\rm GWR} = 6\times10^8\left(\frac{a}{R_\odot}\right)^4\frac{M_\odot^3}{M_1M_2(M_1+M_2)}\ \text{yrs}. \qquad (2)$$

Here, a is the semi-major axis of the system. The line corresponding to equality of $\tau_{\rm GWR}$ and $\tau_{\rm H}$ is shown in Fig. 1a (curve *1*).

The main driving force for the evolution of systems with donors with masses $M_2 = (0.3$–$1.5)M_\odot$ is the magnetic stellar wind, which carries away the angular momentum of the axial rotation of the donor and, via the spin–orbital interaction, the orbital angular momentum of the system as well. According to the semi-empirical formula of Skumanich [17], the characteristic time for the loss of orbital angular momentum via the donor's magnetic stellar wind $\tau_{\rm MSW}$ is given by the relation [13]:

$$\tau_{\rm MSW} = 3\times10^6\left(\frac{a}{R_\odot}\right)^5\frac{M_1}{M_\odot}\frac{M_\odot^6}{M_2^4(M_1+M_2)^2}\ \text{yrs}. \qquad (3)$$

Setting this equal to the Hubble time, we find a limit for the semi-major axis of a system with $M_2 = (0.3$–$0.9)M_\odot$, show by the dashed line *2* in Fig. 1a. For systems with more massive donors, the limit for the life times of detached systems becomes the time for depletion of hydrogen in the donor core $\tau_{\rm MS} = 10^{10}(M_\odot/M_2)^{3.5}$ yrs (line *3* in Fig. 1a).

The semi-major axes of the systems considered are bounded from below by the condition that the donor fill its Roche lobe, whose mean radius can be estimated from the formula $R_{\rm R} = 0.5a(M_2/(M_2+M_{BH}))^{0.44}$ [10]. Curve *4* in Fig. 1a corresponds to this limit. As a result, a region containing systems that are the direct precursors of X-ray systems with

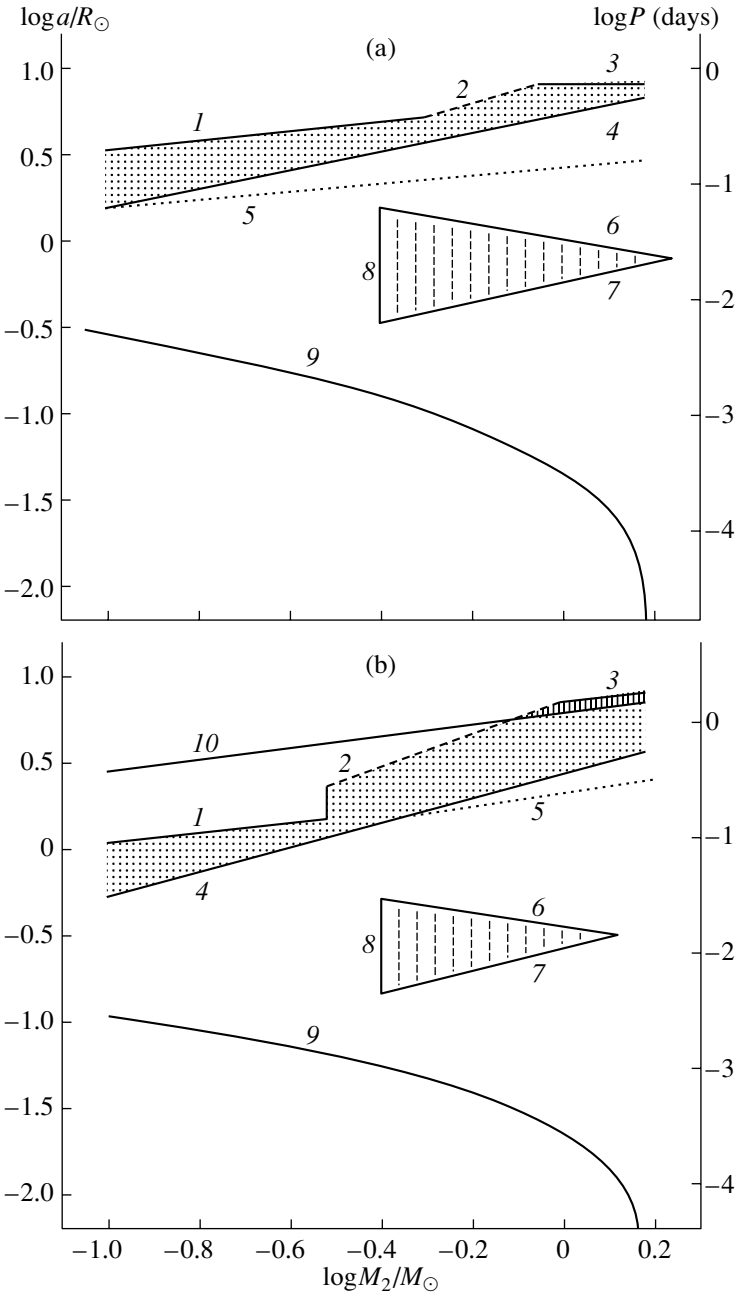

Fig. 1. Region for the formation of X-ray binary systems in which the accretors are (a) black holes with masses of 10 $M_\odot$ and (b) neutron stars or degenerate dwarfs with masses of 1 $M_\odot$. The upper region corresponds to the formation of systems with low-mass MS donors and the lower region to the formation of systems with non-degenerate helium-star donors. See the text for further information about the notation.

MS donors is delineated in Fig. 1a. The mass of these donors is bounded from above by the condition $M_2 \lesssim 1.5\ M_\odot$, which is equivalent to the requirement that the donor have a convective envelope that makes possible the existence of a magnetic stellar wind. In the mass-conserving case, the system evolves downward in Fig. 1a in the indicated region to contact of the donor with its Roche lobe, then proceeds to the left along the line corresponding to this contact. It is important to realize that the donor remains in thermal equilibrium in the semi-detached phase of the evolution, since the line corresponding to equality between the thermal time scale of the donor τ_{KH} and the characteristic time for the loss of the system's orbital angular momentum τ_{MSW} (dotted curve *5* in Fig. 1a) passes below the boundary for contact systems. As a result, we see that X-ray binaries with low-mass MS donors and black-hole accretors occur in a nar-

row interval of semi-major axes $\Delta\log(a) \approx 0.2$, which predetermines the low rate of their formation.

Another class of X-ray binaries with low-mass donors is possible—systems whose donors are non-degenerate helium stars. Such stars form during the evolution of the secondary components of close binary systems if their initial masses exceed $\sim 2.5\ M_\odot$; the mass of the helium star will exceed $\sim 0.4\ M_\odot$ [18]. Helium stars do not possess magnetic stellar winds, and the only driving force behind the evolution of such systems is gravitational radiation. This constrains their position in the a—M_2 plane to be above the line $\tau_{\rm GWR} = \tau_{\rm He}$, where $\tau_{\rm He}$ is the time scale for the depletion of helium in the cores of helium stars, which can be estimated using the formula [19] $\tau_{\rm He} \approx 10^7 (M_\odot/M_2)^{3.1}$ yrs. Line *6* in Fig. 1a corresponds to this constraint. This region is bounded from below by the condition that the donor fill its Roche lobe (line *7*). The left boundary of the region of precursors of X-ray binaries with non-degenerate helium donors is determined by the condition for helium burning in a non-generate star with $M_2 \gtrsim 0.4\ M_\odot$ (line *8*).

Finally, the formation of the closest systems with black-hole accretors and degenerate-dwarf donors is possible if, after the second common-envelope stage, the semi-major axis of the system falls in the range 0.2–4 $R_\odot$, or between line *9* in Fig. 1a marking the position of semi-detached systems with degenerate-dwarf donors and the boundary of the zone in which the influence of gravitational-wave radiation by the system is important ($\tau_{\rm GWR} = \tau_{\rm H}$, line *1*). The radii of the degenerate dwarfs were taken to be $R_{dd}/R_\odot = 0.0196 - 0.0116 M_{dd}/M_\odot$ [20]. The evolution of this type of semi-detached system can occur only in the direction of increasing orbital period, since the radius of the degenerate star increases as its mass decreases.

In this way, we have considered the formation of the three main classes of X-ray binary systems with black-hole accretors and low-mass donors. To investigate the influence of the accretor mass on the parameters of the X-ray binary precursors, we constructed the plot in Fig. 1b, where we have taken the mass of the compact accretor to be one solar mass. The accretor in such systems could be a neutron star, degenerate dwarf, or even a MS star (for example, as in the W UMa system). Decreasing the mass of the accretor by a factor of ten leads to a small shift of the studied regions toward smaller semi-major axes and shorter orbital periods.

Two new circumstances arising as the mass of the accretor decreases are worthy of attention. First, the line $\tau_{\rm MSW} = \tau_{KH}$ (line *5* in Fig. 1b) now intersects line *4*, corresponding to the donor filling its Roche lobe. This means that the decrease in the mass of the MS donor under the action of the magnetic stellar wind now takes the star out of thermal equilibrium. Its radius becomes somewhat larger than the radius of the MS star, which is important when the orbital period of the system is decreased to ~ 3 hrs [13]. At the same time, as the donor's mass decreases, it becomes fully convective, so that its magnetic stellar wind is switched off. As a result, the star loses contact with its Roche lobe for some time and the system becomes detached. After the cessation of the mass loss, the donor radius decreases to its equilibrium value, extending the detached stage. However, after some time, the emission of gravitational radiation again causes the components to approach, and the donor again fills its Roche lobe. This leads to a "gap" in the distribution of orbital periods for cataclysmic binary systems. Observations show that the number of systems in the region of this gap is indeed reduced. The orbital-period gap extends approximately from two to three hours.

The second circumstance connected with restrictions on the semi-major orbital axes of young binaries in the solar neighborhood is the value of $a/R_\odot \gtrsim 6(M_2/M_\odot)^{1/3}$ [10], which is shown by line *10* in Fig. 1b. Figure 1b shows that, as a result, there should not be any W UMa contact binaries with $M_2 \lesssim 0.8\ M_\odot$, corresponding to $P \lesssim 7$ hrs (where P is the orbital period of the system). Analytical estimates have shown that the magnetic stellar wind is not able to shift the components of such wide systems over their MS life times. Indeed, observations [10, 21] indicate that the shortest orbital periods of W UMa close binaries are 6–8 hrs. The agreement between the observed minimum periods for this type of system and the theoretical estimates provides additional support for the quantitative description we have adopted for the efficiency of the magnetic stellar wind in carrying away the orbital angular momentum of the system. It also follows from Fig. 1b that W UMa contact binaries belong to a rather rare type of binary star whose rate of formation in our Galaxy does not exceed 0.01 per year. Only the comparative ease with which the very probable eclipses in these systems can be detected has led to their good representation in catalogs of close binaries. The restriction on the minimum masses of the precursors of W UMa systems should exclude them from globular clusters. Indeed, a detailed study of the globular cluster NGC 3201 detected only one system of this type. This question is worthy of further study.

3. ACCOUNT OF THE INDUCED STELLAR WIND

The main difference between our current study and a number of previous investigations of the evolution of X-ray binaries with black holes, such as [22, 23], is

that we have taken into account the evaporation of the donor under the action of incident hard radiation [24]. Some observational data suggest the existence of stellar winds for the donors of X-ray binaries and companions of millisecond pulsars. For example, the long durations of the eclipses observed for several binary millisecond pulsars testify to the presence of extended halos around the low-mass companions of the neutron stars, interpreted as evidence of intense mass loss by these companions in the form of stellar winds [25, 26]. In addition, the existence of single millisecond pulsars, for which, as a rule, their companions have completely dissipated, can also be taken as evidence for induced stellar winds irradiating the donors [27].

In our computations, we used a comparatively simple self-consistent analytical model to describe the induced stellar wind [28, 29]. The rate of mass loss via the induced stellar wind is determined by the balance between heating of the expanding corona of the star by X-ray radiation and its radiative cooling. We also took into account the energy that must be spent to raise the donor material from the surface of the star. This approach is described in detail in [1], and we present here only the main resulting formulas. The formula for the donor mass-loss rate has the form

$$\dot{M}_{\rm ISW} = 2.47\times10^{-10} f \frac{\alpha_{\rm ISW}^2 M_2^2}{R_2} \times \left[\left(1+9.53\times10^{13}\frac{R_2^4}{\alpha_{\rm ISW}^2 M_2^3 a^2}\dot{M}_{\rm ACC}\right)^{1/2}-1\right]. \quad (4)$$

Here,

$$\alpha_{\rm ISW} = v_{\rm ISW}/(2GM_2/R_2)^{1/2} \quad (5)$$

is the ratio of the speed of the stellar wind to the parabolic speed at the donor surface and $\dot{M}_{\rm ACC}$ is the accretion rate at the surface of the accretor. If the donor fills its Roche lobe, $\dot{M}_{\rm ACC} = \dot{M}_{\rm ACC,ISW} + \dot{M}_{\rm L1}$, where $\dot{M}_{\rm ACC,ISW}$ is the rate at which the material of the induced stellar wind is captured by the accretor and $\dot{M}_{\rm L1}$ is the rate of mass exchange through the point L1. If the donor does not fill its Roche lobe, $\dot{M}_{\rm ACC} = \dot{M}_{\rm ACC,ISW}$. In addition, if the accretion rate exceeds the Eddington limit for the accretor, this limit is adopted for $\dot{M}_{\rm ACC}$, and the remaining material is taken to be lost from the system. The factor f is added to the above formula to allow for uncertainty in the adopted formalism.

We calculated the rate at which the ISW material is captured by the accretor using the classical Bondi–Hoyle formula:

$$\dot{M}_{\rm ACC,ISW} = \frac{1}{4\alpha_{\rm ISW}^4}\left(\frac{M_1}{M_2}\frac{R_2}{a}\right)^2 \dot{M}_{\rm ISW}. \quad (6)$$

When the donor does not fill its Roche lobe and the energy required to raise material from the donor surface is much less than the energy incident onto its surface, we can obtain from (4) and (6) analytical formulas for the mass-loss rate of the donor and accretion rate:

$$\dot{M}_{\rm ISW} = 1.45\times10^{-6}\alpha_{\rm ISW}^{-2}\frac{M_1^2}{M_2}\left(\frac{R_2}{a}\right)^4, \quad (7)$$

$$\dot{M}_{\rm ACC,ISW} = 3.63\times10^{-7}\alpha_{\rm ISW}^{-6}\frac{M_1^4}{M_2^3}\left(\frac{R_2}{a}\right)^6. \quad (8)$$

Note the strong dependence of these quantities on $\alpha_{\rm ISW}$. The larger this parameter (i.e., the larger the stellar-wind speed), the smaller the fraction of the donor material captured by the accretor. Accordingly, the energy release during the accretion is decreased, together with the irradiation of the donor and the intensity of the induced stellar wind. The energy that must be spent to overcome the gravitation of the donor imposes conditions on the existence of induced stellar winds in detached systems, which are expressed by the formula

$$\left(\frac{R_2}{a}\right) > 0.136\alpha_{\rm ISW}\left(\frac{M_2}{M_1}\right)^{1/2}\left(\frac{M_2}{R_2}\right)^{1/4}\frac{1}{f^{1/4}}. \quad (9)$$

A number of studies have developed fairly detailed hydrodynamical models for induced stellar winds, i.e., numerical computations of flows of material from irradiated stellar coronas. First and foremost, we note the work of Tavani and London [27], who carried out computations of a spherically symmetric flow of matter in the presence of a specified irradiation of a star. Note that the values of $\alpha_{\rm ISW}$ obtained in [27] reach 0.7–0.9 at distances of about the stellar radius from the stellar surface. We compared the mass-loss rates obtained in [27] with those given by our ISW model for the same total energy irradiating the donor. This comparison showed that the mass-loss rates in our model are a factor of 1.3–1.6 lower than those in the model of Tavani and London [27], with the difference between the models decreasing as the irradiating energy decreases. We therefore conclude that our simple model yields fairly realistic values for the mass-loss rates due to the induced stellar wind.

It is important to keep in mind that the donor can appreciably change its radius under the influence of irradiation [30]. This circumstance must also be taken into account in a complete theory. We have not considered this effect here.

4. MAIN FACTORS DETERMINING THE EVOLUTION OF CLOSE BINARIES WITH BLACK HOLES

As we indicated above, the evolution of close binaries is determined by the loss of angular momentum from the system due to gravitational radiation and/or the magnetic stellar wind of the donor, mass exchange between the components, and the loss of matter from the system. Standard models for the evolution of close binary systems assume that the mass exchange between the components does not change the total angular momentum of the system. Formulas for the variations in the angular momentum and semi-major axis of a system corresponding to these processes have been presented by us earlier in a number of papers (see, for example, [1, 31]), and we consider these processes here only briefly and qualitatively.

(1) *Exchange of matter between the components.* If the donor is less massive then the accretor, mass exchange increases the semi-major axis of the system. In the absence of an induced stellar wind, mass exchange is possible only when the donor fills its Roche lobe. However, in the presence of an induced stellar wind, exchange becomes possible even without the donor filling its Roche lobe, since the accretor will capture some of the donor's stellar wind, facilitating continued irradiation of the donor with hard radiation. In this case, the condition for efficient mass exchange becomes a fairly high degree of Roche-lobe filling by the donor.

(2) *Mass loss from the system.* In the absence of an induced stellar wind, matter is lost from the system when the rate of mass loss by the donor exceeds the Eddington limit for the accretion rate. In this case, the matter leaving the system carries away some of the specific angular momentum of the accretor. In the presence of an induced stellar wind, there is additional mass loss from the system—that part of the stellar wind that is not captured by the accretor leaves the system, carrying away specific angular momentum from the donor (the so-called Jeans mode). This type of mass loss results in an increase in the semi-major axis of the system. Thus, induced stellar winds lead to an additional process that separates the components.

(3) *Loss of momentum from the system via the magnetic stellar wind of the donor.* We computed the effect of this process, which leads to a decrease in the orbital axis, using the semi-empirical formula (3). We chose the coefficient in the formula for the resulting variations in the semi-major axis so that the theoretical value for the gap in the orbital periods of cataclysmic binaries corresponded with the observed gap.

(4) *Loss of momentum from the system as a result of gravitational radiation.* This process also tends to decrease the orbital axis. It plays an important role only in systems with orbital periods less than ~ 8 hrs, and is essentially negligible in long-period systems.

The competition between these processes is what determines the direction of evolution in a system: whether the semi-major axis and period of the orbit increase or decrease with time. It also determines the rate of mass loss by the donor.

5. BRIEF DESCRIPTION OF THE PROGRAM USED TO COMPUTE THE EVOLUTION OF CLOSE BINARIES

In our numerical studies of the evolution of close binaries with compact accretors, we simultaneously computed the evolution of the donor and time variations in the semi-major axis of the binary orbit. We did not include the evolution of the accretor, except for variations in its mass. We used the method proposed by Kolb and Ritter [32] to compute the donor mass-loss rate for a specified donor radius and mean Roche-lobe radius. We investigated the evolution of the donor using evolutionary code based on a fitting method. The equation of state of the matter was adopted in accordance with [33, 34]. We estimated the opacity of the matter using the tables of [35, 36], and the rates of nuclear reactions were taken from [37, 38]. We estimated neutrino energy losses using the formulas of Beaudet *et al.* [39]. The ratio l/H_p in mixing-length theory was taken to be 1.8, since this corresponds to the value for the standard model for the modern Sun obtained using this program. We applied the Schwarzschild criteria when computing the boundaries of convective zones. The initial mass of the black holes was taken to be 10 $M_\odot$ for all the computed tracks. We adopted the value 1.5 for the parameter $\alpha_{\rm ISW}$.

6. COMPUTATION RESULTS

6.1. Systems with Low-Mass MS Donors

To study these systems, we computed a series of tracks with donors with initial masses of 0.8 $M_\odot$ located on the main sequence at the beginning of the mass exchange. Figures 2 and 3 demonstrate the dependences of the resulting tracks in the $\log P$–$\log \dot{M}_2$ diagram on the main parameters of the computations. Figure 2 presents the dependence on the coefficient f [Eq. (4)], which varies the intensity of the induced stellar wind. Figure 3 shows the dependence on the initial degree of Roche-lobe filling by the donor D, taken to be equal to the initial ratio of the donor radius and the mean radius of the Roche lobe, for $f = 0.5$. A standard track with no induced stellar wind is also depicted in these figures. It is clear that the induced

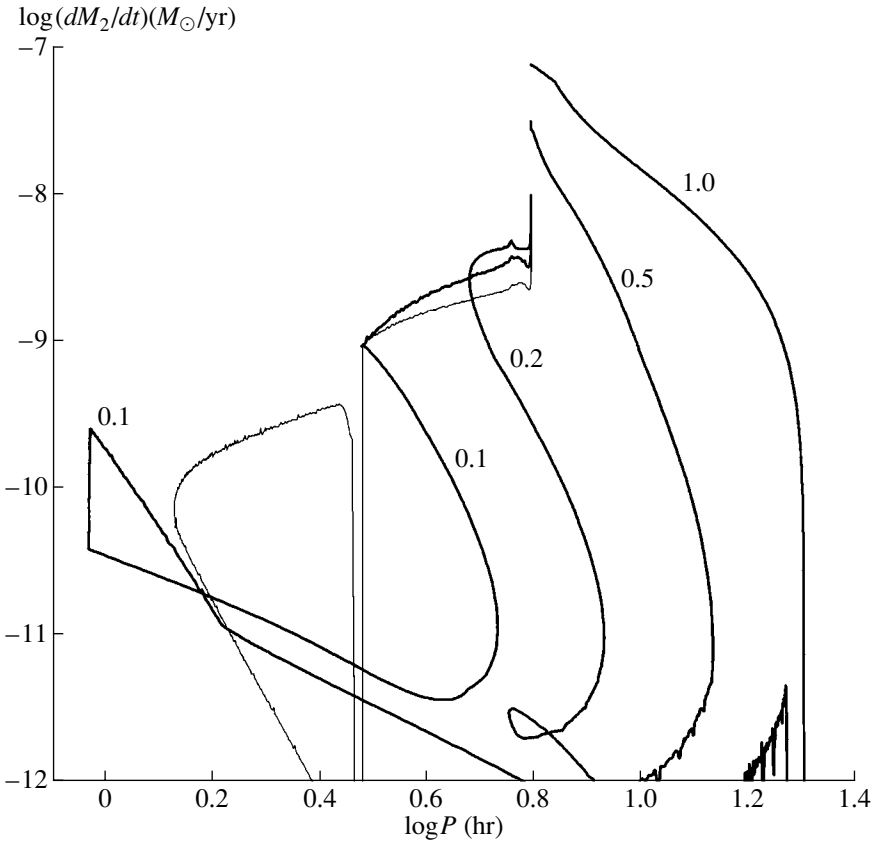

Fig. 2. Tracks for systems with donors that are MS stars with masses of 0.8 $M_\odot$ in a log(period)—log(donor mass-loss rate) diagram. The thin curve depicts the standard model with no induced stellar wind, while the thick curves show tracks for models with an induced stellar wind. The numbers indicate the value of f, and D is equal to unity for all the tracks with induced stellar wind.

stellar wind appreciably changes the evolution of the system, causing the donor to lose contact with its Roche lobe. This contact is preserved until the donor becomes fully convective only when the intensity of the induced stellar wind is reduced by a factor of ten ($f = 0.1$ in Fig. 2). However, afterwards, instead of a modest gap (see the standard track), a prolonged stage without contact is initiated, and the direction of the system's evolution is changed: instead of decreasing, the orbital period increases. This behavior is characteristic of all the tracks with induced stellar wind, and is due to the presence of an additional process moving the stars apart. However, after a substantial decrease in the donor mass, the intensity of the induced stellar wind falls, and the period of the system begins to decrease. When $f = 0.1$, the donor fills its Roche lobe anew, but then again loses contact with the Roche lobe when the mass-loss rate through the point L_1 falls. On the tracks with $f \geq 0.2$, the donor loses contact with its Roche lobe in the initial stage of the evolution and does not regain it.

If the mass exchange begins when $D < 1$, the Roche-lobe filling never occurs (Fig. 3). In these cases, the evolution differs little from the case $D = 1$ and $f \geq 0.5$. The differences begin only at small D ($D = 0.4$ in Fig. 3), when the induced stellar wind is weakened by the large distance between components and the main role is played by processes that cause the stars to approach. On most tracks, the period begins to decrease only in the final stage, when the intensity of the induced stellar wind falls due to the large decrease in the donor mass. In the presence of an intense induced stellar wind, the system spends nearly its entire life time in the region of relatively large orbital periods. The prolonged stage of decreasing P characteristic of cataclysmic binaries does not occur.

The ratios of the accreted mass to the mass lost by the donor for the tracks with induced stellar wind with $D = 1$ and $f = 0.1$, 0.2, 0.5, and 1.0 are 0.72, 0.41, 0.23, and 0.24, respectively, while this ratio is equal to 0.22, 0.09, 0.12, and 0.17, respectively, when $f = 0.5$ and $D = 1.0$, 0.8, 0.6, and 0.4. Thus, about 10% of the mass lost by the donor can be accreted when the induced stellar wind is intense and the degree of Roche-lobe filling by the donor is slightly less than unity.

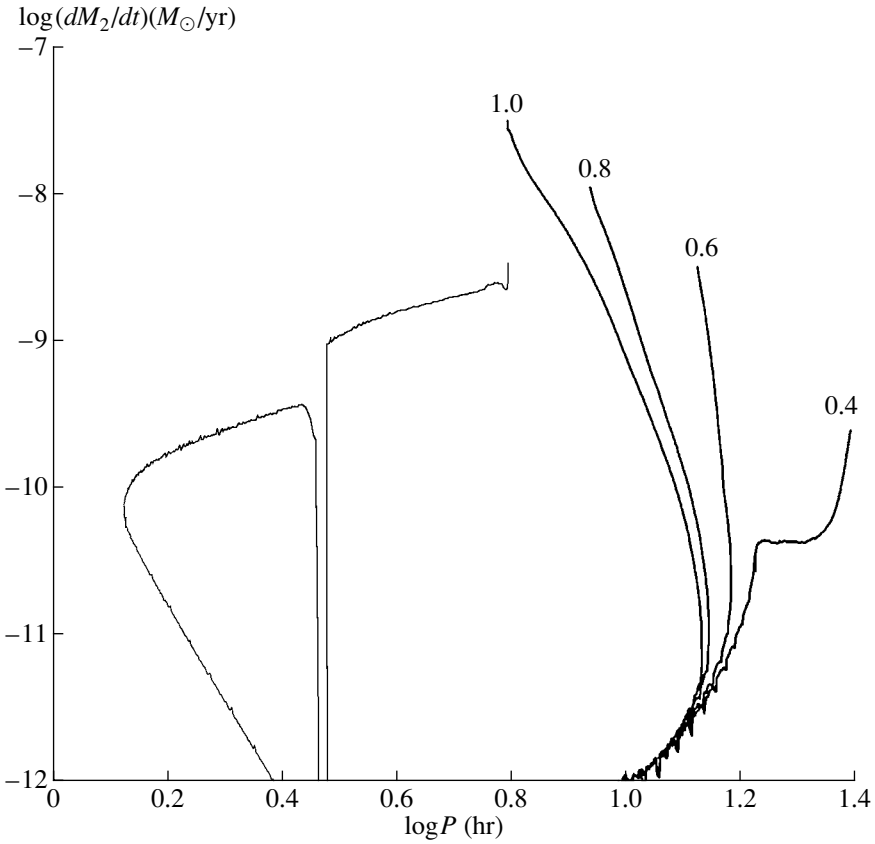

Fig. 3. Tracks for systems with MS donors with masses of 0.8 $M_\odot$ in a log(period)—log(donor mass-loss rate) diagram. The thin curve depicts the standard model with no induced stellar wind, while the thick curves show tracks for models with an induced stellar wind. The numbers indicate the value of D, and f is equal to 0.5 for all the tracks with an induced stellar wind.

6.2. Systems with Evolved, Low-Mass Donors

We investigated this case by considering a system with an evolved donor with initial mass 1 $M_\odot$. The relative mass of the donor's helium core is 0.19 at the onset of the mass exchange. Figure 4a presents tracks for models with an induced stellar wind for $D = 1.0$ and $D = 0.5$, with $f = 0.5$, as well as a track for the case with no induced stellar wind. One characteristic feature of this last track is that the evolution of the system is determined by the nuclear evolution of the donor, accompanied by its expansion, leading to an increase in the period of the system. Evolution with an induced stellar wind also leads to an increasing period, but the mass-loss rate of the donor in the initial stages is increased due to this wind. Therefore, the donor is transformed into a helium core on these tracks. The rate of mass loss by the donor via the induced stellar wind first decreases sharply due to the strong decrease in the donor radius and the degree of Roche-lobe filling, after which the induced stellar wind ceases. Note that, when $D = 1$, the donor maintains contact with its Roche lobe only in the initial stage, and this contact is never established when $D = 0.5$. Thus, in this case as well, there is an appreciable change in the evolution of the system in the presence of an induced stellar wind.

The ratio of accreted mass to mass lost by the donor for the tracks with an induced stellar wind with $D = 1.0$ and 0.5 is 0.37 and 0.25, respectively.

6.3. Systems with Moderate-Mass MS Donors

To study this case, we computed the evolution of a system whose donor has an initial mass of 2 $M_\odot$ and is located on the main sequence at the onset of the mass exchange. There is no magnetic stellar wind in this case, and gravitational radiation is negligible. Figure 4b depicts tracks with the same ISW parameters as in Fig. 4a. The track for no induced stellar wind is qualitatively very similar to the previous track, since the rapid evolution of the more massive MS donor yields the same general pattern as the evolution of a donor that is less massive but already has a helium core by the onset of the mass exchange. (The non-monotonic change in the mass-loss rate at the beginning of the track is due to the depletion of hydrogen at the center of the star and the disappearance of the convective core.) Here, the two ISW tracks

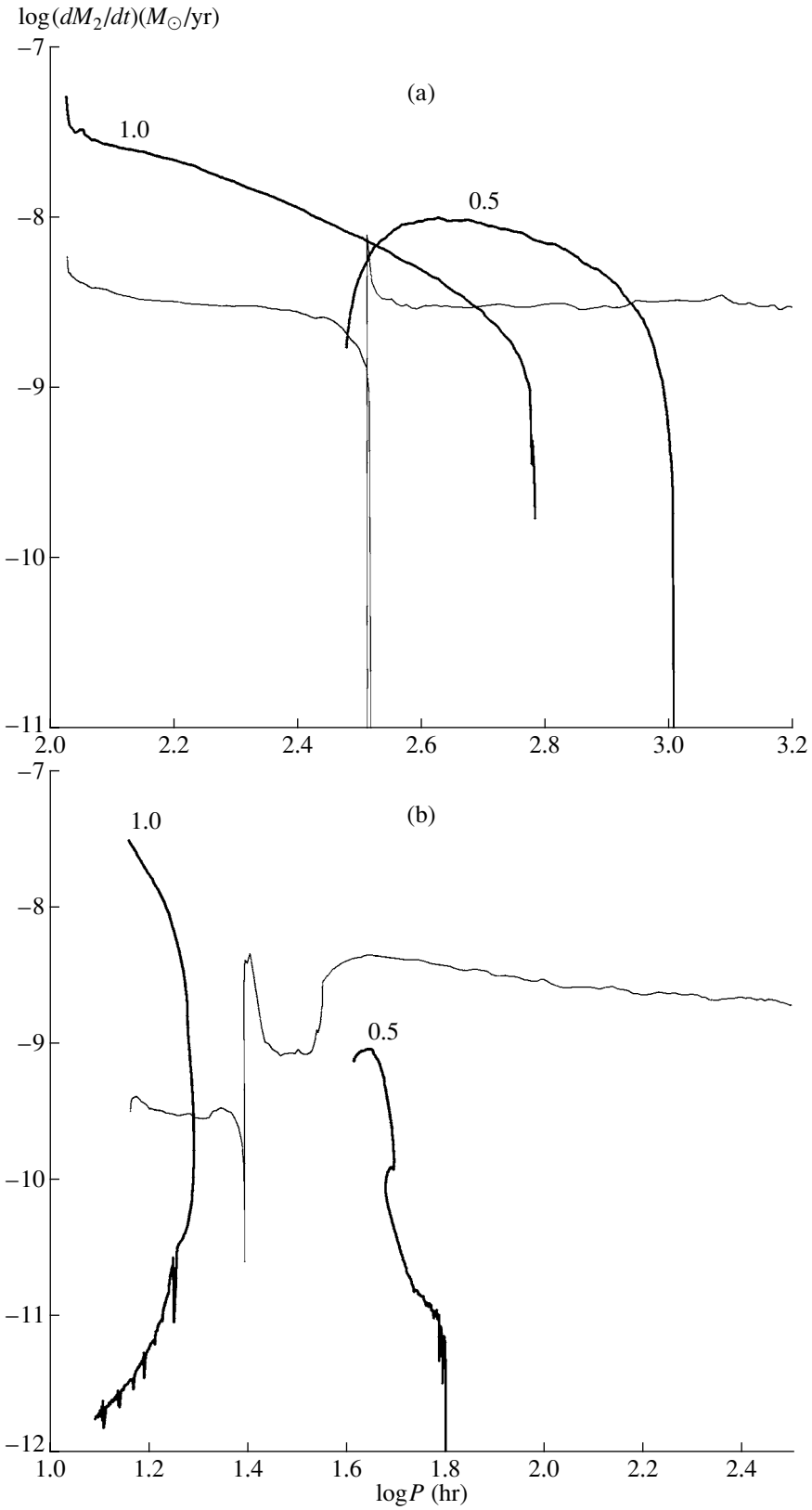

Fig. 4. Tracks for systems with (a) evolved donors with masses of 1 $M_\odot$ and (b) MS donors with masses of 2 $M_\odot$ in a log(period)—log(donor mass-loss rate) diagram. The thin curve depicts the standard model with no induced stellar wind, while the thick curves show tracks for models with an induced stellar wind. The numbers indicate the value of D, and f is equal to 0.5 for all the tracks with an induced stellar wind.

are somewhat different: on the track with $D = 1$, the nuclear evolution of the donor has virtually no effect due to the rapid mass decrease brought about by the induced stellar wind, and this track has the same form as that for an unevolved, low-mass donor in Fig. 3. The mass-loss rate for the track with $D = 0.5$ is lower, due to the large distance between the stars, and the donor is able to form a compact helium core and expand. Therefore, the evolution brings about an increase in the period and, as in the previous case, ends with the cessation of the induced stellar wind. As a result, the tracks with induced stellar wind reach much shorter orbital periods that those without such a wind.

The ratios of accreted mass to mass lost by the donor for the tracks with an induced stellar wind for $D = 1.0$ and 0.5 are 0.08 and 0.04, respectively.

6.4. Systems with Helium-Star Donors

We investigated this case by computing the evolution of a system whose donor is a non-degenerate helium star with a mass of 0.5 $M_\odot$. Figure 5a shows a track without an induced stellar wind and a track with such a wind for $D = 0.5$. The influence of the induced stellar wind on the evolution of the system is substantially reduced in this case. The induced stellar wind is weak due to the large gravitational potential at the surface of the helium donor. The periods of systems with dwarf donors are very small, and the leading role in this case is played by the loss of momentum from the system via gravitational radiation. As a result, the tracks with and without an induced stellar wind differ only in the initial and final stages. The initial stage is characterized by an approach of the stars in the detached stage. After the donor fills its Roche lobe, the tracks are virtually identical, since $\dot{M}_{\rm ISW}$ is substantially smaller than $\dot{M}_{\rm L1}$. However, when the period increases and the mass-loss rate falls as a consequence of the degeneracy of the donor, there comes a time when $\dot{M}_{\rm ISW}$ and $\dot{M}_{\rm L1}$ are comparable. Further, the induced stellar wind begins to play a leading role in the system's evolution. Under its influence, the donor loses contact with its Roche lobe, and the orbital period begins to increase more rapidly than for the track with no induced stellar wind. The ratios of the accreted mass to the mass lost by the donor on the ISW tracks are virtually identical to the ratio for the track with no induced stellar wind. In both cases, nearly all of the mass lost by the donor is accreted.

6.5. Systems with White-Dwarf Donors

We investigated this case using the example of a system whose donor is a degenerate white dwarf with a mass of 0.6 $M_\odot$. Figure 5b shows tracks both without and with an induced stellar wind computed for $D = 0.5$. As in the previous case, the tracks with and without an induced stellar wind differ only at the beginning and end of the evolution, and these differences have precisely the same character. Accordingly, we conclude that the influence of induced stellar winds is very small in systems with degenerate dwarfs.

7. COMPARISON WITH OBSERVATIONS

We compared the results of our computations with observational data using log (orbital period)—log (donor mass) diagrams (Figs. 6, 7). These figures display parameters of observed X-ray binaries whose donors have masses less than $\sim 3\ M_\odot$ [40–42]. The thick grey curve shows the positions of donors that are equilibrium MS stars filling their Roche lobes. It is easy to show that, if the mass of a donor filling its Roche lobe is small compared to the mass of the accretor, the orbital period of the system is determined only by the donor's parameters: $P = 8.92 R_2^{3/2}/M_2^{1/2}$. Figure 6 presents standard tracks for systems with black holes and with no induced stellar wind, with the numbers near the tracks indicating the initial mass of the donor. Figure 7 shows tracks with induced stellar wind, with the figures again indicating the initial mass of the donor; for two tracks, the inital degree of filling of the Roche lobe is indicated in parantheses (for the remaining tracks, this was close to unity). The donors for all tracks were located on the main sequence at the initial time, since low-mass stars have the highest probability of filling their Roche lobes, as they are not yet evolved. The horizontal tick marks on the tracks indicate times when the donor mass-loss rate decreases to $10^{-9.5}\ M_\odot$/yr.

One characteristic feature of the observed systems is that they are located fairly far from the curve corresponding to contact of the MS donors with their Roche lobes. This may indicate that all their donors are evolved, or alternatively that the donors are not in contact with their Roche lobes.

The standard tracks without an induced stellar wind (Fig. 6) correspond to the first of these explanations: although the donors are located on the main sequence at the initial time, they have had time to evolve somewhat in the first stages of the evolution, when their initial mass is more than 1 $M_\odot$. (Note that the track for 1 $M_\odot$ nearly merges with the line of contact for MS donors, since the donor for this track remains unevolved.) Let us consider the group of observed systems with low-mass donors and comparatively short orbital periods, located in the left part of the figure. The interval of MS-donor masses for these systems estimated from the tracks without an induced stellar wind turns out to be too narrow—approximately from 1.5 to 1.7 $M_\odot$—since less massive donors do not have sufficient time to

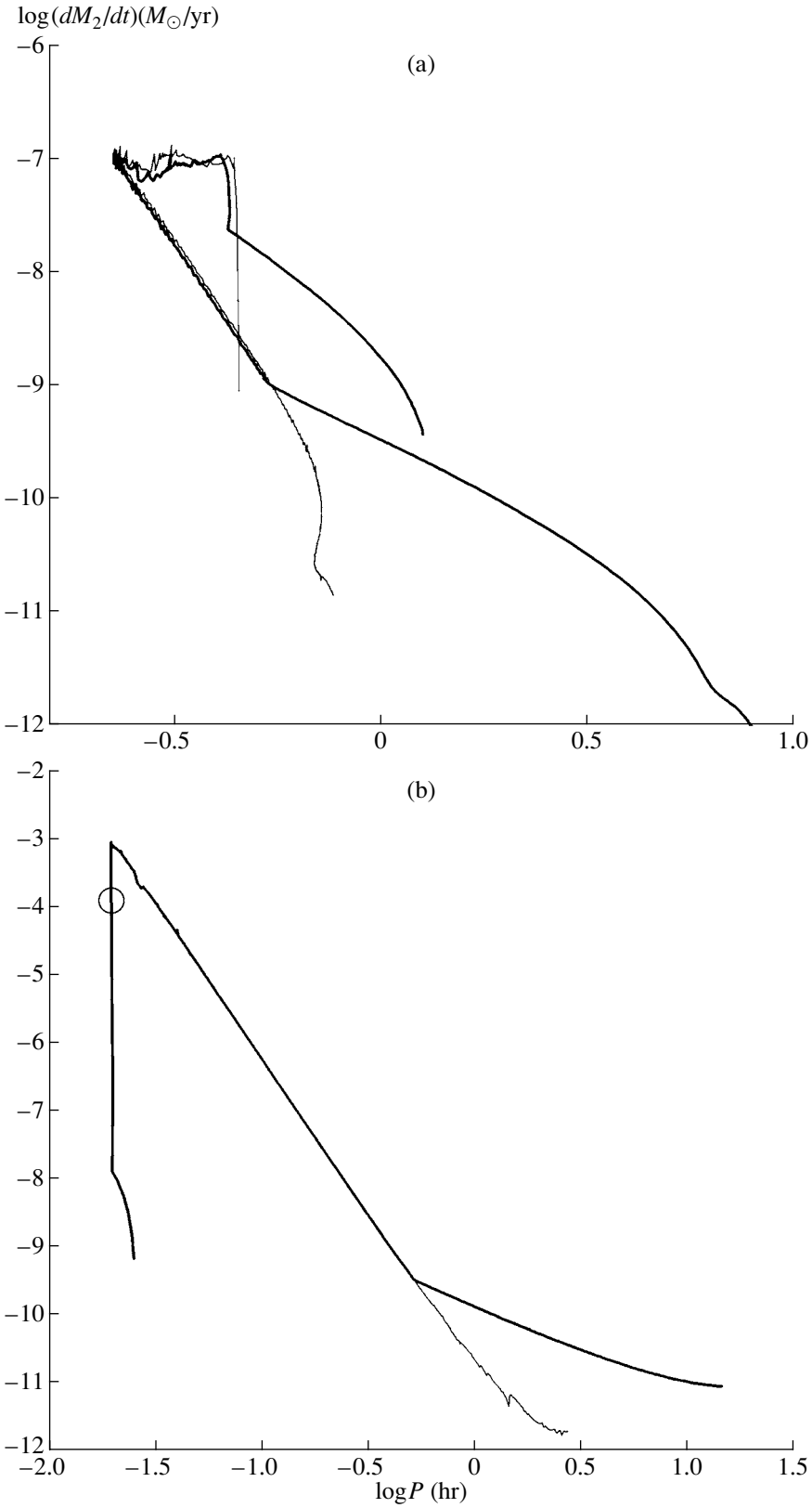

Fig. 5. Tracks for systems with (a) degenerate helium donors with masses of 0.5 $M_\odot$ and (b) degenerate dwarf donors with masses of 0.6 $M_\odot$ in a log(period)—log(donor mass-loss rate) diagram. The thin curve depicts the standard model with no induced stellar wind, while the thick curve shows the track for an induced stellar wind with $D = 0.5$ and $f = 0.5$. The circle in the second diagram marks the beginning of the standard track.

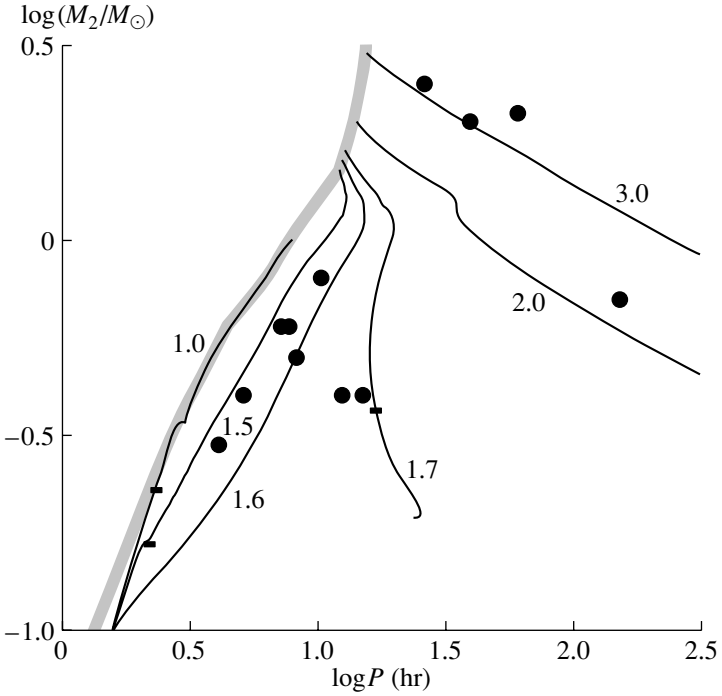

Fig. 6. Log (period)—log (donor mass) diagram. The filled circles indicate the parameters for observed X-ray binaries with black holes. The thick greay curve shows the positions of donors that are MS stars that fill their Roche lobes. The thin curves depict standard tracks without an induced stellar wind, with the figures indicating the initial masses of the donors in $M_\odot$. The horizontal tick marks on the tracks indicate times when the donor's mass-loss rate decreases to $10^{-9.5}\ M_\odot$/yr.

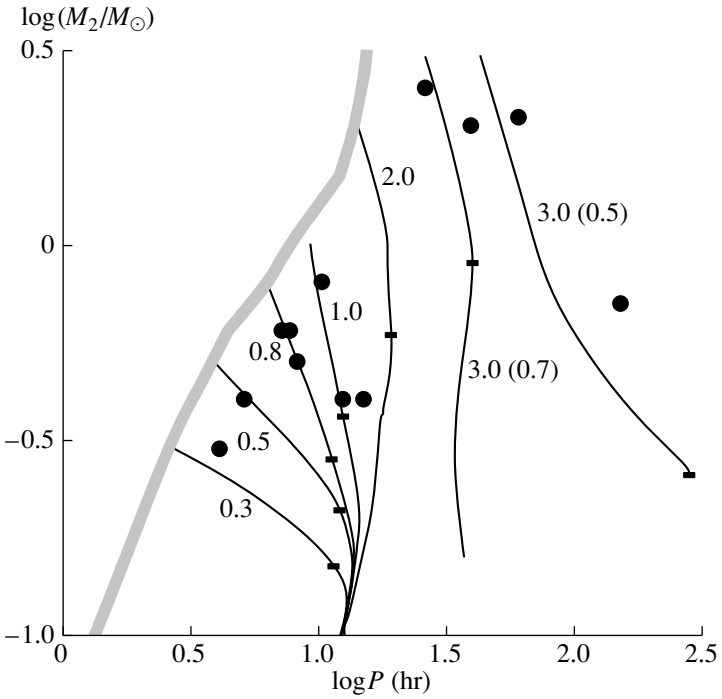

Fig. 7. Same diagram as in Fig. 6. The thin curves depict tracks with an induced stellar wind, with the figures indicating the initial donor masses in $M_\odot$ and the figures in parantheses indicating the initial degree of Roche-lobe filling by the donor. The horizontal tick marks on the tracks indicate times when the donor's mass-loss rate decreases to $10^{-9.5}\ M_\odot$/yr.

evolve and more massive donors evolve too rapidly. An additional deficiency of this system of tracks is the absence of observed systems with orbital periods less than ~ 4 hrs, which should be well represented in the absence of an induced stellar wind, as shown by the example of cataclysmic systems.

The tracks with induced stellar winds (Fig. 7) correspond to the second explanation above: the donors do not fill their Roche lobes, and the mass exchange proceeds via the induced stellar wind. The donors for the ISW tracks are not necessarily evolved, and the interval of initial donor masses on tracks passing through the group of observed systems with low-mass donors and comparatively short periods is fairly wide. Note that evolution with an induced stellar wind can explain the absence of systems with very short periods (less than ~ 4 hrs), while such systems should exist for standard evolutionary tracks (Fig. 6). There are, indeed, no observed systems with very short periods. The collection of points on tracks corresponding to a decrease in the donor mass-loss rate to $10^{-9.5}\ M_\odot$/yr form a fairly satisfactory boundary from below for the region occupied by the observed systems. Thus, our computations of evolution with an induced stellar wind are able to explain the observed distribution of systems with black holes in the orbital period—donor mass diagram.

8. CONCLUSION

The intensity of the induced stellar wind is determined by parameters whose precise values cannot be estimated at this time. Therefore, our computations of the evolution of X-ray binaries with black holes taking into account an induced stellar wind currently represent a primarily qualitative illustration of the possible characteristics of the evolution of close binaries with compact accretors and induced stellar wind. Nevertheless, they enable us to draw certain conclusions.

The computations show that induced stellar wind can substantially change the evolution of the systems considered. First, mass exchange becomes possible even when the donor does not fill its Roche lobe. Second, as a rule, in the case of intense induced stellar wind, the donor loses contact with its Roche lobe, or even never reaches the Roche lobe, during the course of the system's evolution. A comparison of the theoretical computations and observations shows that the donors in some observed systems may, indeed, not fill their Roche lobes, which may provide evidence in support of the presence of a fairly intense induced stellar wind. Third, the direction for variation of the system's period changes on the ISW tracks for low-mass donors: during a large part of the evolution, the period increases rather than decreases. The absence of observed systems with short periods may represent evidence in support of precisely this type of evolution. Fourth, an appreciable fraction of the mass lost by the donor leaves the system; when the induced stellar wind is intense, the fraction of accreted matter reaches $\sim 10\%$. A number of observational data testify that the fraction of accreted matter should, indeed, be about this value.

Note that the parameters of the observed systems can also be interpreted using standard tracks without an induced stellar wind, but two problems arise in this case: the interval of initial donor masses for most systems is too narrow, and theoretically predicted systems with periods shorter than ~ 4 hrs are absent.

ACKNOWLEDGMENTS

This work was supported by the Russian Foundation for Basic Research, project no. 99-02-17619.

REFERENCES

1. I. Iben, A. V. Tutukov, and A. V. Fedorova, Astrophys. J. **486**, 955 (1997).
2. A. V. Tutukov and L. R. Yungel'son, Astron. Zh. **79**, 738 (2002)
3. H. J. Grimm, M. Gilfanov, and R. A. Sunyaev, astro-ph/0109239.
4. R. Supper, G. Hasinger, W. H. G. Lewin, *et al.*, Astron. Astrophys. **373**, 63 (2001).
5. T. E. Strohmayer, astro-ph/0109559.
6. J. van Paradijs, in *X-Ray Binaries,* Ed. by W. H. G. Lewin, J. van Paradijs, and E. P. J. van den Heuvel (Cambridge Univ. Press, Cambridge, 1995), p. 536.
7. A. Zezas, G. Fabbiano, A. Prestwich, *et al.*, astro-ph/0109302.
8. A. M. Cherepashchuk, Space Sci. Rev. **93**, 473 (2000).
9. J. E. McClintock, M. R. Garcia, N. Caldwell, *et al.*, Astrophys. J. **551**, L147 (2001).
10. A. G. Masevich and A. V. Tutukov, *Stellar Evolution: Theory and Observations* [in Russian] (Nauka, Moscow, 1988).
11. C. L. Fryer and V. Kalogera, Astrophys. J. **554**, 548 (2001).
12. M. J. Barlow, *Wolf-Rayet Stars: Observations, Physics, Evolution,* Ed. by C. W. H. de Loore (Cambridge Univ. Press, Cambridge, 1982), p. 149.
13. I. Iben and A. V. Tutukov, Astrophys. J. **284**, 719 (1984).
14. E. L. Martín, M. R. Zapatero-Osorio, and R. Rebolo, Astron. Soc. Pac. Conf. Ser. **109**, 615 (1996).
15. E. L. Martín and M. R. Zapatero-Osorio, Mon. Not. R. Astron. Soc. **286**, L17 (1997).
16. L. D. Landau and E. M. Lifshitz, *The Classical Theory of Fields* (Fizmatgiz, Moscow, 1962; Pergamon, Oxford, 1975).

17. A. Skumanich, Astrophys. J. **171**, 565 (1972).
18. I. Iben and A. V. Tutukov, Astrophys. J., Suppl. Ser. **58**, 661 (1985).
19. I. Iben and A. V. Tutukov, Astrophys. J. **313**, 727 (1987).
20. I. Iben and A. V. Tutukov, Astrophys. J. **342**, 430 (1989).
21. W. A. Rucinski, Astron. J. **103**, 960 (1992).
22. E. Ergma and A. Fedorova, Astron. Astrophys. **338**, 69 (1998).
23. E. Ergma and M. J. Sarna, astro-ph/0107041.
24. M. Ruderman, J. Shaham, M. Tavani, and D. Eihler, Astrophys. J. **343**, 292 (1989).
25. E. P. J. van den Heuvel and J. van Paradijs, Nature **334**, 227 (1988).
26. F. Camilo, D. R. Lorimer, P. Frejre, *et al.*, Astrophys. J. **535**, 975 (2000).
27. M. Tavani and R. London, Astrophys. J. **410**, 281 (1993).
28. I. Iben, Jr., A. V. Tutukov, and L. R. Yungelson, Astrophys. J., Suppl. Ser. **100**, 233 (1995).
29. V. V. Muzylev and A. V. Tutukov, Nauchn. Inf. Astrosoveta Akad. Nauk SSSR **26**, 3 (1973).
30. Ph. Podsiadlowski, Nature **350**, 136 (1995).
31. A. V. Fedorova and A. V. Tutukov, Astron. Zh. **71**, 431 (1994) [Astron. Rep. **38**, 377 (1994)].
32. U. Kolb and H. Ritter, Astron. Astrophys. **236**, 385 (1990).
33. G. Fontaine, H. C. Graboske, and H. M. van Horn, Astrophys. J., Suppl. Ser. **35**, 293 (1977).
34. D. Saumon, G. Chabrier, and H. M. Van Horn, Astrophys. J., Suppl. Ser. **99**, 713 (1995).
35. C. A. Iglesias and F. J. Rogers, Astrophys. J. **464**, 943 (1996).
36. D. R. Alexander and J. W. Ferguson, Astrophys. J. **437**, 879 (1994).
37. M. J. Harris, W. A. Fowler, G. R. Caughlan, and B. A. Zimmerman, Ann. Rev. Astron. Astrophys. **21**, 165 (1983).
38. G. R. Caughlan, W. A. Fowler, M. J. Harris, and B. A. Zimmerman, At. Data Nucl. Data Tables **32**, 197 (1985).
39. G. Beaudet, V. Petrosian, and E. E. Salpeter, Astrophys. J. **150**, 979 (1967).
40. A. M. Cherepashchuk, Astron. Zh. **78**, 145 (2001) [Astron. Rep. **45**, 120 (2001)].
41. P. Charles, in *Black Holes in Binaries and Galactic Nuclei,* Ed. by L. Kaper, E. P. J. van den Heuvel, and P. A. Woudt (Springer, 2001), p. 27.
42. R. M. Wagner, C. B. Foltz, T. Shahbaz, *et al.*, Astrophys. J. **556**, 42 (2001).

Translated by D. Gabuzda